

CHARACTERIZATION OF INDIVIDUAL STRAIGHT AND KINKED BORON  
CARBIDE NANOWIRES

by

Zhiguang Cui

A dissertation submitted to the faculty of  
The University of North Carolina at Charlotte  
in partial fulfillment of the requirements  
for the degree of Doctor of Philosophy in  
Nanoscale Science

Charlotte

2016

Approved by:

---

Dr. Terry Xu

---

Dr. Qiuming Wei

---

Dr. Thomas Schmedake

---

Dr. Haitao Zhang

---

Dr. Wesley Williams

©2016  
Zhiguang Cui  
ALL RIGHTS RESERVED

## ABSTRACT

ZHIGUANG CUI. Characterization of individual straight and kinked boron carbide nanowires. (Under the direction of DR. TERRY XU)

Boron carbides represent a class of ceramic materials with p-type semiconductor natures, complex structures and a wide homogeneous range of carbon compositions. Bulk boron carbides have long been projected as promising high temperature thermoelectric materials, but with limited performance. Bringing the bulk boron carbides to low dimensions (*e.g.*, nanowires) is believed to be an option to enhance their thermoelectric performance because of the quantum size effects. However, the fundamental studies on the microstructure-thermal property relation of boron carbide nanowires are elusive. In this dissertation work, systematic structural characterization and thermal conductivity measurement of individual straight and kinked boron carbide nanowires were carried out to establish the true structure-thermal transport relation. In addition, a preliminary Raman spectroscopy study on identifying the defects in individual boron carbide nanowires was conducted.

After the synthesis of single crystalline boron carbide nanowires, straight nanowires accompanied by the kinked ones were observed. Detailed structures of straight boron carbide nanowires have been reported, but not the kinked ones. After carefully examining tens of kinked nanowires utilizing Transmission Electron Microscopy (TEM), it was found that they could be categorized into five cases depending on the stacking faults orientations in the two arms of the kink: TF-TF, AF-TF, AF-AF, TF-IF and AF-IF kinks, in which TF, AF and IF denotes transverse faults

(preferred growth direction perpendicular to the stacking fault planes), axial faults (preferred growth direction in parallel with the stacking fault planes) and inclined faults (preferred growth direction neither perpendicular to nor in parallel with the stacking fault planes). Simple structure models describing the characteristics of TF-TF, AF-TF, AF-AF kinked nanowires are constructed in SolidWorks, which help to differentiate the kinked nanowires viewed from the zone axes where stacking faults are invisible.

In collaboration with the experts in the field of thermal property characterization of one dimensional nanostructures, thermal conductivities of over 60 nanowires including both straight and kinked ones have been measured in the temperature range of 20 – 420 K and the parameters (*i.e.*, carbon contents, diameters, stacking faults densities/orientations and kinks) affecting the phonon transport were explored. The results disclose strong carbon content and diameter dependence of thermal conductivities of boron carbide nanowires, which decreases as lowering the carbon content and diameter. Stacking fault orientations do modulate the phonon transport ( $\kappa_{TF} < \kappa_{AF}$ ), while stacking fault densities seems to only have obvious effects on phonon transport when meeting certain threshold (~39%). The most interesting discovery is significant reduction of thermal conductivity (15% – 40%) in kinked boron carbide nanowires due to phonon mode conversions and scattering at the kink site.

Last but not least, micro-Raman spectroscopy study on individual boron carbide nanowires has been performed for the first time, to the best of our knowledge. Based on the preliminary data, it is found that the stacking fault orientations have no apparent effect on the Raman scattering, but the stacking fault densities do. In addition, up as the

size going down to nanoscale, some Raman modes are inactive while some new ones show up, which is largely ascribed to the quantum confinement effects. One more important finding is that the carbon content also plays important role in the Raman scattering of boron carbide nanowires in the low frequency region ( $< 600 \text{ cm}^{-1}$ ), which mainly comes from the 3-atom chains (C-B-C or C-B-B).

## ACKNOWLEDGEMENTS

Firstly, I would like to gratefully and sincerely thank my advisor, Dr. Terry Xu, for her persistent help, guidance, support and encouragement on my research and study during the last four years. She sets excellent example to her students on conducting research with her diligent attitude and experiences. The good habits on time management, data summarization and documentation and academic integrity that I have learned from her will definitely benefit my future life and career.

In addition, special thanks go to Dr. Qiuming Wei, Dr. Thomas Schmedake, Dr. Haitao Zhang and Dr. Wesley Williams for serving in my doctoral committee and for their many valuable suggestions on how to present my research and write dissertation more concisely and clearly.

I am also very thankful to my groupmates Dr. Baobao Cao, Dr. Zhe Guan, Dr. Youfei Jiang and SiangYee Chang. The former two had taught me how to use the most important tool in my dissertation research, Transmission Electron Microscopy (TEM) and shared with me their experiences and useful tips accumulated in years without any reservation. The latter two had prepared all samples for me. Without their support and efficient cooperation, most of the works cannot be conducted smoothly. Additionally, I am grateful to be able to collaborate with Dr. Deyu Li's group at Vanderbilt University, working on the thermal property characterization of individual nanowires. I also would like to thank Dr. Yong Zhang and his student, Jason Marmon, at UNC Charlotte for sharing the micro-Raman system and their expertise with me and for insightful

discussions. In addition, I appreciate the enjoyable time spent with friends here at UNC Charlotte.

Finally and most importantly, I would express my deepest gratitude to my parents, Fengqi Cui and Suzhen Zhang and my two brothers, Zhiyong Cui and Zhihao Cui, who truly care about, trust, support and encourage me throughout my life.

## TABLE OF CONTENTS

CHAPTER 1: INTRODUCTION	1
1.1 Thermoelectric Effects	2
1.2 Boron Rich Materials	5
1.3 Bulk Boron Carbides	7
1.4 Why Going to Nanoscale	11
1.5 Boron-rich (Boron Carbide ) Nanostructures	17
1.6 Kinked Nanowires	21
1.7 Raman Spectroscopy on Individual Nanowires	23
1.8 Objectives	26
CHAPTER 2: EXPERIMENTS AND METHODS	29
2.1 Chemical Vapor Deposition (CVD)	29
2.2 Scanning Electron Microscope (SEM)	33
2.3 Transmission Electron Microscope (TEM)	37
2.4 Energy Dispersive X-ray Spectroscopy (EDX/EDS)	39
2.5 Electron Energy Loss Spectroscopy (EELS)	41
2.6 Micro-Raman ( $\mu$ -Raman) Spectroscopy	44
2.7 Micro-device for Thermal Conductivity Measurement of Individual Nanostructures	47
CHAPTER 3: STRUCTURAL INVESTIGATION OF BORON CARBIDE NANOWIRES	50
3.1 Structural Aspects on Establishing True Structural and Properties Relations of Boron Carbide Nanowires	50

3.2 Kinking in Boron Carbide Nanowires	56
CHAPTER 4: THERMAL TRANSPORT AND REPRESENTATIVE ZT OF STRAIGHT AND KINKED NANOWIRES	85
4.1 Background	85
4.2 Experiments	86
4.3 Results and Discussions	88
4.4 Conclusions	100
CHAPTER 5: RAMAN SPECTROSCOPY ON INDIVIDUAL BORON CARBIDE NANOWIRES	102
5.1 Background	102
5.2 Experimental	103
5.3 Results and Discussions	105
5.4 Conclusions	118
CHAPTER 6: CONCLUSIONS AND FUTURE WORKS	120
6.1 Conclusions	120
6.2 Future Works	121
REFERENCES	123
APPENDIX A: COMPARISON BETWEEN EELS AND EDX	148

## CHAPTER 1: INTRODUCTION

As the global climate change becomes severe, United States has initiated the clean power plan to reduce the carbon dioxide (CO<sub>2</sub>) emission according to the newest Annual Energy Outlook 2016 from Department of Energy.<sup>1</sup> In one aspect, current environmental problem requires alternative and renewable energy urgently, such as hydroelectric power, solar and wind. And more and more researches have been performed on developing materials with the abilities to enhance the efficiency of new energy's production. In another aspect, energy recycling shows equal significance in solving current energy problems since more than 60% of all primary energy consumed is wasted worldwide according to statistical results, most in the form of waste heat.<sup>2</sup> It would be great if the waste heat could be collected and converted to electrical energy. Thermoelectric (TE) materials might make this happen since they are capable to convert heat to electricity directly, and vice versa.<sup>3-6</sup> The radioisotope thermoelectric generators (RTGs) used as power source in satellites and spaces probes have long been developed.<sup>7-9</sup> However, the low conversion efficiency of current TE materials limits their wider application. Therefore, it is necessary to find and explore high performance TE materials operated in low temperature (<500 K), moderate temperature (500 K-1000 K) and high temperature (>1000K). Lots of works have been done on low temperature and moderate temperature TE materials, such as PbTe,<sup>10-12</sup> Bi<sub>2</sub>Te<sub>3</sub><sup>13-17</sup> and PbSe,<sup>18,19</sup> but

only a few on high temperature TE materials. Our research focus is the high temperature TE materials based on boron rich compounds, especially boron carbides. In this chapter, the following topics, including (1) the general principle of thermoelectric effects, (2) why are we interested in boron-rich materials, especially boron carbides, (3) why do we want to bring the bulk boron carbides to nanoscale, (4) the current research progress in boron carbide nanostructures' synthesis and characterization, kinked nanowires and Raman spectroscopy on identifying defects in individual nanowires, and (5) the objectives of this dissertation work, will be discussed.

### 1.1 Thermoelectric Effects

The first demonstration of thermoelectric effects was done by German scientist T.J. Seebeck in 1821,<sup>20</sup> in which an electromotive force could be produced by applying a temperature gradient at the joint between two different metals. This phenomenon is known as Seebeck effect, which is the basic principle for thermoelectric power generations. Thirteen years later, in 1834 a French physicist J.C.A. Peltier discovered a small heating or cooling effect at the junction depending on the direction of an electric current passing through a thermocouple,<sup>21</sup> which is just opposite to the Seebeck effect and named as Peltier effect. Peltier effect is more often used in the field of thermoelectric refrigeration or cooling. The demonstration of Seebeck effect and Peltier effect using simple thermocouple was schematically shown in Figure 1.1 (a) and (b) respectively. In case of Seebeck effect, a light bulb connected with the cold sides of the thermocouple made of p-type and n-type materials will be lightened up in the circuit when temperature difference ( $\Delta T$ ) applied between hot side and cold side, which drives

the charge carriers (electrons and holes) flow. The resulting current or thermoelectric voltage is proportional to the temperature difference. Another important parameter to be mentioned is the figure of merit ( $ZT$ ), which directly describes the performance of TE materials or devices and is defined in equation (1.1):

$$ZT = \left( \frac{S^2 \sigma}{\kappa} \right) T \quad (1.1)$$

where  $S$  is Seebeck coefficient,  $\sigma$  is electrical conductivity,  $\kappa$  is thermal conductivity, and  $T$  is absolute temperature. For a material with temperature-independent properties, the ideal TE conversion efficiency  $\eta$ , as a function of  $T_H$  (hot side temperature),  $T_C$  (cold side temperature),  $\Delta T$  and  $ZT$ , could be defined as<sup>22</sup>

$$\eta = \frac{\Delta T}{T_H} \frac{\sqrt{1 + ZT} - 1}{\sqrt{1 + ZT} + \frac{T_C}{T_H}} \quad (1.2)$$

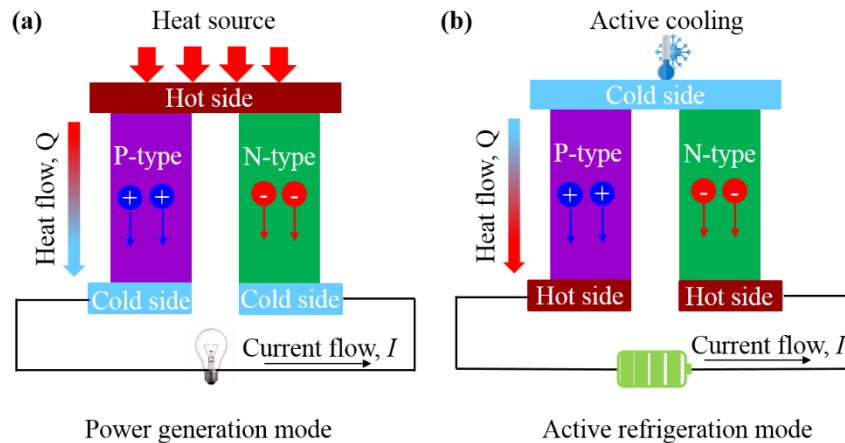


Figure 1.1: Schematic illustrations of a simple TE couple composed of a p-type leg and n-type leg for demonstrating (a) Seebeck effect (power generation) and (b) Peltier effect (active refrigeration). (a) The temperature gradient causes charge carriers (electrons or holes) to diffuse from hot side to cold side, which results in current flowing through the circuit. (b) Heat at the upper junction evolves to the lower junction when a current passes through the circuit.

Figure 1.2 presents the power generation efficiency of ideal TE generator (devices) at different  $ZT$  values as a function of hot side temperature calculated by M. Zdbarjadi *et al.*<sup>23</sup> The cold side temperature is assumed to be room temperature. Current best TE materials have  $ZT$  value in the range of 1-2, which leads to a power generation efficiency of 10%-20%. It is obvious with this low efficiency, TE generators could not compete against prime power converters with Carnot efficiency, such as internal combustion engines. However, TE generators' conversion efficiencies are comparable to the existing most renewable and clean energy sources, such as photovoltaics, geothermal, biomass and wave energy. In general, TE materials with higher  $ZT$  value are favored in order to achieve high conversion efficiency. A  $ZT$  value  $>3$  is preferred.

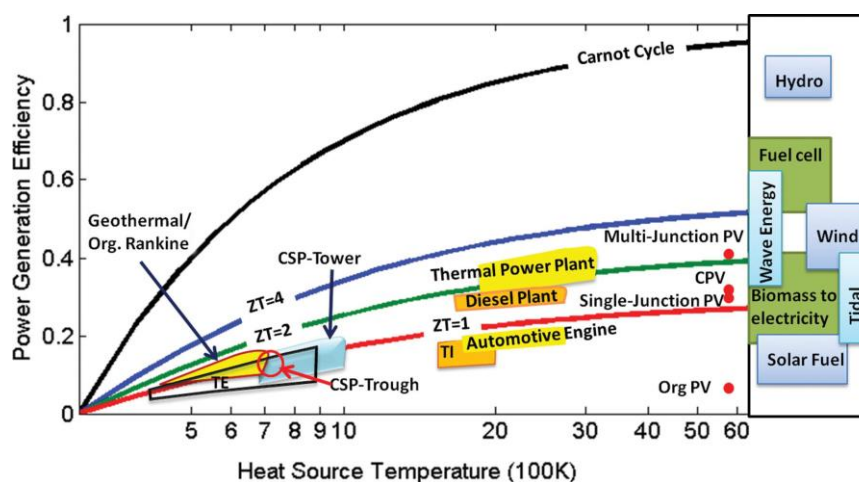


Figure 1.2: Plots of ideal TE generator's power generation efficiency versus temperature of the hot side (cold side assumed to be room temperature) aiming at competing with other different energy conversion technologies. The conversion efficiency range of other renewable energy is marked on the right side. The abbreviation of PV, CSP, Org, TE and TI stands for photovoltaic, concentrated solar power, organic devices, thermoelectric devices, and thermionic devices respectively.<sup>23</sup>

As for the demonstration of Peltier effect, the light bulb was replaced by a direct current source (battery) and a small thermometer was positioned on the junction of a thermocouple. As the current flows through the circuit from n-type leg to p-type leg, a slight active cooling at the junction happens and is measured by the thermometer since the heat carried by electrons is absorbed at the top junction and released at the lower junction. If reversing the current flow direction, the heat transport direction would be reversed as well and the upper junction will become hot. The TE cooling efficiency is also highly dependable on the figure of merit  $ZT$ . Therefore, it is of significance to explore TE materials with high  $ZT$  no matter for TE power generation or for TE cooling.

Peltier effect actually interrelates with Seebeck effect according to thermal dynamics, which was first discovered by W. Thomson in 1851.<sup>24</sup> The relationship between Seebeck coefficient and Peltier coefficient was established, which proves Peltier coefficient simply equals to the product of Seebeck coefficient and absolute temperature. Based on W. Thomson's theory, he predicted a third TE effect existing in a homogeneous conductor, now known as Thomson effect, in which, there is a reversible heating or cooling when a flow of electric current passes in the conductor with a temperature gradient applied as well. Here, heat transport is proportional to both current and temperature gradients. The proportionality constant is Thomson coefficient, which is thermal dynamically related with Seebeck coefficient. However, Thomson effect has little technical application and attracts less attention than the other two types of TE effects.

## 1.2 Boron Rich Materials

Bulk boron-rich materials describe a wide range of highly refractory and super hard boron compounds, which are also referred as the main derivatives of elemental boron and borides. Pure elemental boron tends to have four main polymorphs,  $\alpha$ -rhombohedral boron,  $\beta$ -rhombohedral boron,  $\alpha$ -tetragonal boron and  $\beta$ -tetragonal boron.<sup>25</sup> One common and unique building unit of the above mentioned pure elemental boron polymorphs is the  $B_{12}$  icosahedron, in which boron atoms stay at the twelve vertices and is bonded to five nearest boron atoms.<sup>26</sup> Because of the electron deficient nature of boron, the internal bonding of the icosahedron is an unusual three center bonding. If a crystalline element boron's building unit is  $B_{12}$  icosahedron, there will be more than one  $B_{12}$  icosahedron in the unit cell. For examples, eight  $B_{12}$  icosahedra locate at the vertices of rhombohedral unit in  $\alpha$ -rhombohedral boron.<sup>27</sup> The bonds between icosahedra are extremely strong, which make the crystalline elemental boron having high melting point and stability. Therefore, the pure elemental boron has low reactivity at room temperature, but high reactivity at high temperature, where it reacts with metals, carbons, silicon and oxygen to form various icosahedral boron-rich compounds, such as, boron pnictides ( $B_{12}As_2$ ,  $B_{12}P_{12}$ ), boron carbides ( $B_4C$ ), silicon boride ( $SiB_6$ ) and boron suboxides ( $B_6O$ ).<sup>25</sup> Those boron-rich compounds adopt the similar crystal structure and bonding characteristics of icosahedral elemental boron with additional two atoms (P-P, As-As, O-O) or three atoms (C-B-C, C-B-B, B-B-B) inter-icosahedra chains.<sup>28</sup> Regarding to the unique crystal structures of these icosahedral boron-rich materials, many exceptional electronic, thermal and mechanical properties could be expected. For instance, icosahedral boron-rich materials have

potential application in high-temperature TE applications due to their high temperature stability, low intrinsic thermal conductivity, moderately high electrical conductivity and large Seebeck coefficients.

### 1.3 Bulk Boron Carbides

Out of the aforementioned icosahedral boron-rich compounds, boron carbides are one of the most extensively investigated ones. Boron carbides is a compositionally disordered material whose homogeneity range extends from  $B_4C$  at carbon-rich phase (~20 at% C) to  $B_{11}C$  at boron-rich phase (~8 at% C).<sup>29-31</sup> At this homogeneity range, all boron carbides exist as rhombohedral phase, which is similar to  $\alpha$ -rhombohedral boron. Therefore, the stoichiometric boron-to-carbon ratio varies in different boron carbide phases, but  $B_4C$  ( $B_{12}C_3$ ) is commonly used to simply represent boron carbides. The crystal structure of boron carbide is  $\alpha$ -rhombohedral of trigonal symmetry ( $R\bar{3}m$  space group) with lattice parameters ( $a = 5.16 \text{ \AA}$  and  $\alpha = 65.7^\circ$ ).<sup>28,32</sup> As illustrated in Figure 1.3 (a), the primary structural units of boron carbides, 12-atom icosahedra and 3-atom linear chain, locate at the eight vertices and the longest diagonal ( $[111]$  axis) of a rhombohedral unit respectively. It is well known that the rhombohedral structure can be transformed and described as a hexagonal structure, in which the  $[0001]_h$  axis corresponds to the  $[111]_r$  rhombohedral axis. In this dissertation, all crystallographic indices are in rhombohedral notation.

Lots of works have been done to investigate the occupancy of carbon atoms in the boron carbide rhombohedral unit cell, especially in the 3-atom chain.<sup>33-37</sup> There are two types of chemically distinct sites in each icosahedral cluster: six equatorial sites

connecting to the chain and six polar sites connecting directly to another icosahedron, as visualized in the  $B_{12}$  icosahedra shown in Figure 1.3 (b), in which the bright atoms represent polar sites while the dark atoms represent equatorial sites.<sup>32</sup> The possible combination of structural elements for boron carbide which has been proposed are  $B_{12}$  and  $B_{11}C$  icosahedra and C-C-C, C-B-C (Figure 1.3 (d)), C-B-B (Figure 1.3 (e)), B-B-B, B-vacancy-B (Figure 1.3 (f)) chains. But there is still debate on the exact carbon occupancy in boron carbide even with same stoichiometric boron-to-carbon ratio. For example, the structural representation of  $B_4C$  or  $B_{12}C_3$  could be  $(B_{11}C)CBC$  or  $(B_{12})CCC$ . If taking the equatorial sites and polar sites into account,  $(B_{11}C)CBC$  could be further categorized into two cases,  $(B_{11}C_p)CBC$  and  $(B_{11}C_e)CBC$ , in which  $C_p$  means carbon atom occupying polar site and  $C_e$  represents carbon atom occupying equatorial site.<sup>38</sup> Figure 1.3 (c) shows one polar boron site is randomly substituted by a carbon atom (black sphere).

It is worth noting that in practice the as-synthesized boron carbides, mostly being polycrystalline, are more disorder than the ideal model, which means the carbon atoms could substitute any boron atoms in the icosahedra and diagonal chain. However, just because of the complicated structure, boron carbide as a p-type semiconductor exhibits unusual chemical and physical properties, such as super hardness (only lower than diamond and cubic boron nitride), low density ( $\sim 2.52 \text{ g/cm}^3$ ), light weight, high melting point ( $\sim 2540 \text{ }^\circ\text{C}$ ), high corrosion resistance, wide bandgap, high cross-section for absorption of neutrons and excellent high temperature TE performance.

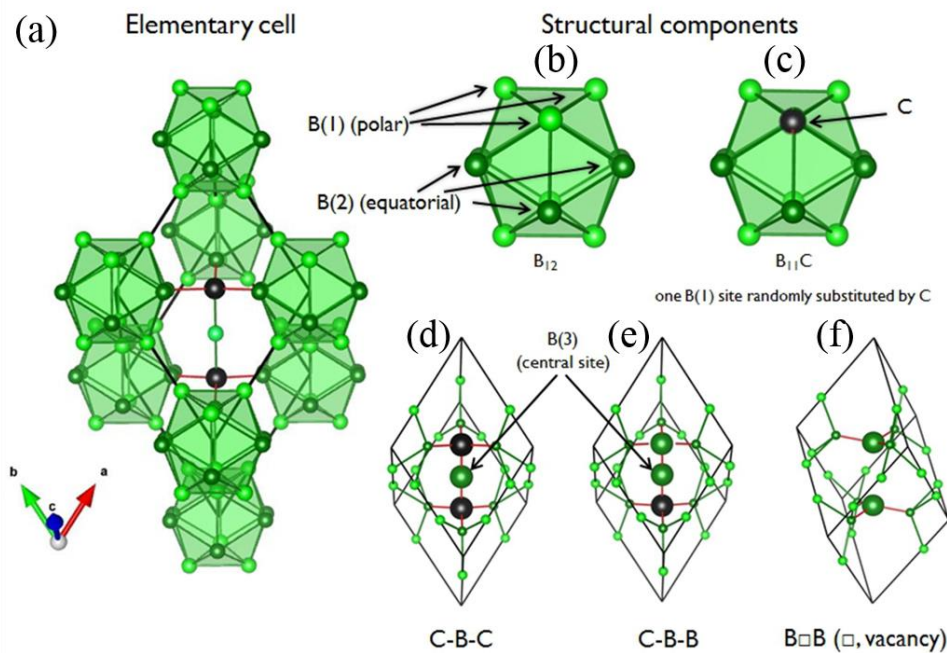


Figure 1.3: Element rhombohedral unit cell and structural components of boron carbide. (a) the general locations of B<sub>12</sub> icosahedra and 3-atom linear chain (C-B-C) in a elementary cell; (b) one B<sub>12</sub> icosahedron with polar sites and equatorial sites highlighted; (c) One B<sub>12</sub> icosahedron with a B polar site randomly substituted by C atom; (d)-(f) three types of diagonal chain are illustrated C-B-C, C-B-B, B-vacancy-B.<sup>32</sup>

In early 1984, boron carbide was proposed by Charles Wood *et al.*<sup>39</sup> to be potentially used for high temperature TE converter because of the high temperature stability and exceptional electronic transport properties. The figure of merit ( $ZT$ ) of hot pressing bulk boron carbide were reported by M. Bouchacourt *et al.*<sup>40</sup> as early as in 1985 and the largest value of  $ZT$  was 1.06 at 1250 K for boron carbide with 13.3 at% carbon, which further confirm the good TE performance of boron carbide. After that, the thermoelectric properties of boron carbide and silicon or aluminum doped boron carbide synthesized via hot pressing, arc melting, spark plasma sintering are widely studied with only a few  $ZT$  (less than 1) reported in 1990s.<sup>34,41-48</sup> It was found the

Seebeck coefficient of boron carbide is large ( 200-320  $\mu\text{V/K}$ ) at high temperatures and continuously increases up to 2000 K;<sup>48,49</sup> its electrical conductivity also increases when temperature elevates; while its thermal conductivity is very low (5-30 W/mK) in the whole homogeneity range and remains low (5-12 W/mK) at high temperatures.<sup>49</sup> Based on equation (1.1), all these properties make boron carbide a very promising TE material with potential high figure of merit  $ZT$ , especially in high temperature range. Most of the boron carbide materials being studied is polycrystalline. In order to better study the thermoelectric properties of boron carbide, I. Gunjishima *et al.*<sup>50</sup> synthesized single crystalline boron carbides using a floating zone method. The Seebeck coefficient of single crystalline boron carbides is 240-260  $\mu\text{V/K}$ , which is comparable to the polycrystalline, but their thermal conductivity is higher than that of polycrystalline ones. Entering 2000s, M. Takeda *et al.* proposed to fabricate boron carbides thin film using pulsed laser deposition and intense pulsed ion beam evaporation.<sup>51,52</sup> Moreover, a thin film based thermoelectric device was demonstrated.  $\text{B}_{13}\text{C}_2$  film and  $\text{SrB}_6$  film was used as p-type and n-type parts respectively to form the p-n thermoelectric device,<sup>53</sup> as shown in Figure 1.4 (a). Figure 1.4 (b) presents the open circuit voltage (maximum 3.93 mV at  $\Delta T = 53$  K) measured with applying the temperature difference to the device, but the hot side temperature was not specified. After inserting a load into the circuit, the output voltage and output electrical power were also evaluated and a maximum 9.15 pW was obtained when load resistance equals to internal device resistance, which is quite small as compared to the maximum output (several Watts at similar conditions) of other available thermoelectric modules (i.e. Bismuth Telluride) composed of tens of

thermocouples. Obviously, there is an urgency to improve the figure of merit ( $ZT$ ) of the boron carbides.

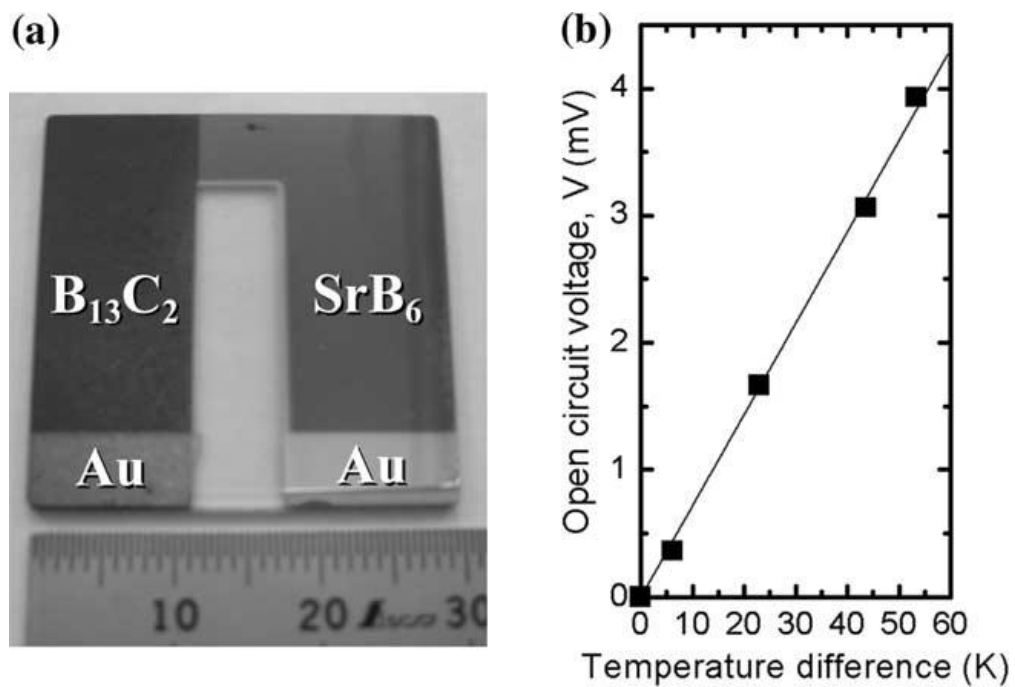


Figure 1.4: (a) A photograph of the  $p$ - $n$  thermoelectric device; (b) open circuit voltage generated from the device with the temperature difference being applied to the device.<sup>53</sup>

#### 1.4 Why Going to Nanoscale

From equation (1.1), it is apparent that a higher figure of merit  $ZT$  would be obtained by increasing the Seebeck coefficient  $S$  and electrical conductivity  $\sigma$ , while decreasing the thermal conductivity  $\kappa = \kappa_e + \kappa_{lat}$ , where  $\kappa_e$  and  $\kappa_{lat}$  represent the thermal conductivity contributed by electrons and lattice vibrations respectively. For bulk TE materials of metals and highly doped semiconductors, in which charge carriers (i.e. electrons) dominate both the electron and phonon transport, those three parameters are

inter-correlated.<sup>54</sup> Increasing  $S$  would generally result in decreasing  $\sigma$  at the same time because of the less number of charge carriers and increasing  $\sigma$  implies an increase in  $\kappa$  since the electrons contributed thermal conductivity is governed by Wiedemann-Franz law, which states that the ratio of the electrical conductivity and thermal conductivity contributed by charge carriers is fixed at specific temperature:<sup>55</sup>

$$\frac{\sigma}{\kappa_e} = L \quad (1.3)$$

where  $L$  is a constant Lorenz number,  $2.4 \times 10^{-8} \text{ J}^2\text{K}^{-2}\text{C}^{-2}$ , and  $T$  is the temperature. Therefore, it is really difficult to increase  $ZT$  in those bulk TE materials because of such adverse effect. However, heat transport in semiconductors is dominated by lattice vibration or phonons,<sup>56</sup> which suggests that interfering with the phonon dynamics could effectively suppress the thermal conductivity while having the Seebeck coefficient and electrical conductivity almost unchanged.

It is known that the lattice thermal conductivity can be reduced by phonon scattering from various types of defects, including point defects, boundaries and stacking faults of finite semiconductor crystals.<sup>57-61</sup> Point defects or atomic disorders could be introduced through the synthesis of isostructural solid solution alloys and consequently leads to significant reduction of thermal conductivity. The representative examples are  $\text{Bi}_{2-x}\text{Sb}_x\text{Te}_3$  and  $\text{Bi}_2\text{Te}_{3-x}\text{Se}_x$  solid solutions, whose TE performance are superior to the parent compound  $\text{Bi}_2\text{Te}_3$ 's.<sup>62,63</sup> The other idea “phonon glass electron crystal” was proposed by Slack in 1995 to achieve low lattice thermal conductivity without deteriorating electronic performance.<sup>64</sup> The “rattling” motion of loosely bonded atoms in skutterudites and clathrates, greatly enhances the phonon scattering,

while has no effects on electron transport.<sup>65-68</sup> Though the aforementioned two approaches have led to marked increase in  $ZT$ , the best  $ZT$  of most bulk TE materials without nanoscale engineering is around 1, which is still far away from the desired  $ZT$  ( $>3$ ) for practical applications.<sup>69</sup>

Nanophase inclusions in the order of 3-20 nm were frequently discovered in bulk  $\text{AgPb}_x\text{SbTe}_{2+x}$  system,<sup>70-73</sup>  $\text{AgPb}_x\text{Sn}_y\text{SbTe}_{2+x+y}$  system,<sup>74</sup>  $\text{NaPb}_x\text{SbTe}_{2+x}$  system<sup>75,76</sup> and  $\text{KPb}_x\text{SbTe}_{2+x}$  system<sup>77</sup>, which reduce the lattice thermal conductivity effectively to as low as 0.5 W/mK because of the strong boundary scattering of phonon. The maximum  $ZT$  of these bulk nanostructured TE materials reaches  $\sim 1.7$  for cubic  $\text{AgPb}_x\text{SbTe}_{2+x}$ .<sup>72</sup> Figure 1.5 shows the figure of merit ( $ZT$ ) values of more high performance TE materials developed with the idea of nanostructuring.<sup>78</sup> The operating temperature of these TE materials covers a wide range from 200K to 1300K. The initial works on low dimensional TE materials including superlattices, quantum dots and nanowires were pioneered by Dresselhaus *et al.* who suggested that quantum confinements could enhance the power factor ( $S^2\sigma$ ). A high  $ZT$  value of up to 2.4 and 3.0 was found in  $\text{Bi}_2\text{Te}_3/\text{Sb}_2\text{Te}_3$ <sup>79</sup> and  $\text{PbTe}/\text{PbTeSe}$ <sup>18</sup> superlattices respectively.

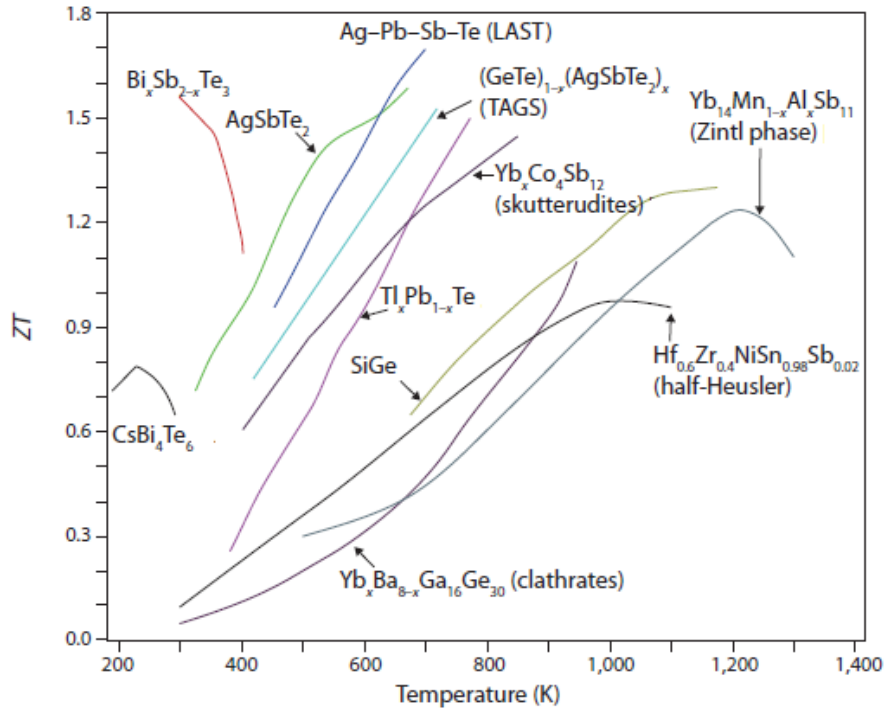


Figure 1.5: Figure of merit ( $ZT$ ) of some high performance bulk TE materials as a function of temperature. Most of these TE materials are subjected to nanostructure engineering.<sup>78</sup>

In addition, in gas-kinetic theory, the heat transport in an elastic medium, which is a random process, could be described in the following equation:<sup>80</sup>

$$\kappa = \frac{1}{3} C v \ell \quad (1.4)$$

where  $C$  is the heat capacity per unit volume,  $v$  is the velocity of sound,  $\ell$  is the mean free path of phonon between collisions. In addition, the length scale of mean free path for phonons is usually much larger than that for charge carriers. Such large difference raises a strategy of nanostructuring to reduce thermal conductivity without affecting the electron transport properties.<sup>81</sup> For this strategy to be successful, the nanostructures should be smaller than phonon mean free path but larger than electron mean free path

in at least one dimension. For single crystalline silicon, its phonon mean free path is  $\sim 300$  nm, while the electron mean free path is only  $\sim 1-2$  nm.<sup>82</sup> A first principle study on n-type silicon with charge carrier concentration between  $10^{16}$  and  $10^{19}$  cm<sup>-3</sup> shows the nanostructures with size of 20 nm could exhibit five times higher  $ZT$  than bulk counterparts in the temperature range of 100 to 400 K.<sup>83</sup> Much stronger TE enhancement was observed in individual Si nanowires experimentally, whose thermal conductivity (2 W/mK) was much smaller than bulk Si's 150 W/mK.<sup>84</sup> The resulting  $ZT$  values are very promising, 0.6 for rough Si nanowires at room temperature<sup>85</sup> and  $\sim 1$  for normal Si nanowire at 200K,<sup>86</sup> which are tens of fold enhancements comparing to the bulk ( $ZT = 0.01$ ). Other than Si nanowires, GaN,<sup>87</sup> Bi<sub>2</sub>Te<sub>3</sub>,<sup>88</sup> InSb,<sup>89,90</sup> InAs<sup>91,92</sup> and Bi nanowires<sup>93</sup> also exhibit significant reduction in thermal conductivity due to phonon-boundary scattering.

Besides the size reduction induced high performance TE materials, it has been proposed that the geometry of the low dimensional nanostructures, especially kinks in nanowires, could also play an important role in reducing thermal conductivity while enhancing Seebeck coefficient and electrical conductivity. For instance, molecular dynamics (MD) simulations performed by Jinwu Jiang and coworkers<sup>94</sup> on the investigation of kinked Si nanowires' thermal conductivity indicates that the kinks are helpful to reduce the thermal conductivity. Comparing to the straight nanowires, the reduction percentage of kinked Si nanowires' thermal conductivity can be as high as 70% at 300K when there are 10 segments of kinks. Biao Wan *et al.*<sup>95</sup> theoretically investigated the TE transport properties of bent nanowires, kinked nanowires, stubbed

nanowires and segmented like superlattices nanowires using GaAs nanowires as an example. For kinked nanowires with single kink, the maximum power factor ( $S^2\sigma$ ), which is a function of Seebeck coefficient and electrical conductivity, is  $1 k_B^2/h$  when kink angle is  $30^\circ$  at  $\mu$  (chemical potential) = 0.11 eV. While for kinked nanowire with fixed kink angle ( $45^\circ$ ) and different number of kinks (1, 2, 3), more kinks could enhance the Seebeck coefficient as well as power factor. Therefore, kinks in nanowires will not only reduce thermal conductivity but also improve the power factor, which offers the opportunity to further improve the figure of merit  $ZT$  in nanowires.

Inspired by the theoretical prediction and experimental validation of increasing the figure of merit  $ZT$  by reducing dimensionality to 2-dimensional (2D) quantum wells<sup>96-98</sup> and superlattices and 1-dimensional (1D) nanowires<sup>99-101</sup>, some works have been done on exploring low dimensional boron-rich nanostructures for TE in recent years.<sup>102,103</sup> In the case of boron nanobelts with  $\alpha$ -tetragonal crystal structure, the power factor was found to be the highest among crystalline boron and amorphous boron.<sup>102</sup> Another boron-rich nanostructure being investigated for TE application is boron carbide nanowires, which do have lower thermal conductivity (7 W/mk) than bulk (35 W/mK) at room temperature.<sup>103</sup> However, to date, no direct  $ZT$  value has been measured and reported for boron-rich nanostructures.

Moreover, another driven force for bringing bulk boron-rich materials to nanoscale is their potential applications in serving as building blocks in microelectromechanical systems (MEMS) and nanoelectromechanical systems (NMES) because of their p-type or n-type semiconductor nature and excellent mechanical

properties.<sup>104-106</sup> Recently, more efforts have been emphasized on synthesizing and studying boron-rich including boron carbide nanostructures, which will be reviewed in detail in the next section.

### 1.5 Boron-rich (Boron Carbide ) Nanostructures

Lots of works have been done on making boron-rich thin films, which could be considered as a type of 2D nanostructures, but most of the recent research focus on synthesizing and characterizing 1D boron-rich nanostructures. For examples, boron nanowires,<sup>107</sup> boron nanobelts,<sup>108</sup> boron nanoribbons,<sup>109</sup> alkaline-earth hexaboride ( $\text{CaB}_6$ ,  $\text{SrB}_6$ ,  $\text{BaB}_6$ )<sup>110,111</sup>, rare earth hexaboride ( $\text{REB}_6$ ,  $\text{RE} = \text{Y, La, Ce, Pr, Nd, Sm, Gd, Tb, Dy, Ho}$ ),<sup>112</sup> boron arsenide ( $\text{B}_{12}\text{As}_2$ ) nanowires,<sup>113</sup> boron carbide ( $\text{B}_4\text{C}$ ) nanowires<sup>103,114-117</sup> and nanorods<sup>118</sup> and boron suboxide ( $\text{B}_6\text{O}$ ) fibers and nanowires<sup>119</sup> have been synthesized by magnetron sputtering, laser ablation, catalyst-assisted chemical vapor deposition and solid state reaction. The structure,<sup>103,114,115</sup> field emission,<sup>117</sup> thermal transport<sup>120</sup> and electrical transport<sup>117</sup> properties of the above boron-rich 1D nanostructures have been investigated and reported, out of which, boron nanoribbon<sup>120</sup> shows enhanced thermal conductivity when bundled together while the thermal conductivity of boron carbide nanowires is significantly lower than that of bulk boron carbide. It should be noted that some 2D boron-rich nanostructures, such as boron and boron carbide nanosheets,<sup>121-124</sup> are also able to be fabricated currently, but with little information about their thermal and electrical properties.

Boron carbide nanostructures, including 0D (nanoparticles), 1D (nanowires, nanorods and nanobelts) and 2D (nanosheets and nanoflakes) have attracted increasing

attentions in recent years due to promising applications in reinforcing nanocomposites and TE conversion. The boron carbide nanoparticles synthesized by solid state reaction or solid vapor reaction tend to have nanometer size (less than 100 nm) and submicron size (around 300 nm), and it was expected that the small grain size could significantly enhance the mechanical properties of B<sub>4</sub>C nanoparticle reinforced nanocomposites.<sup>125-</sup>

<sup>127</sup> Most reported boron carbide 1D nanostructures, especially nanowires, were synthesized via carbothermal reaction and catalyst-assisted chemical vapor deposition with solid or gas source of B and C. Even though the as-synthesized boron carbide 1D nanostructures are usually single crystalline,<sup>103,114</sup> oxygen rich amorphous layer and planar defects are often observed.<sup>103</sup> For example, Figure 1.6 (b) and (c) shows a boron carbide nanowire with stacking faults orientation perpendicular to the projected preferred growth direction of the nanowire (transverse faults, TF) and Figure 1.6 (d) and (e) shows a boron carbide nanowire with stacking faults orientation parallel to the projected preferred growth direction of the nanowire (axial faults, AF). The planar defects are induced by disorder stacking during the growth, as shown in Figure 1.6 (a). In addition, a thin amorphous layer was seen on both type of nanowires. Out of question, those amorphous layer and planar defects might affect the various properties of boron carbide 1D nanostructures, such as thermal conductivity and mechanical properties. But due to the complicated rhombohedral structure of boron carbide, there is lack of detailed structural characterization on the formation of planar defects, which challenges the establishment of true structure and property relationship of boron carbide nanowires.

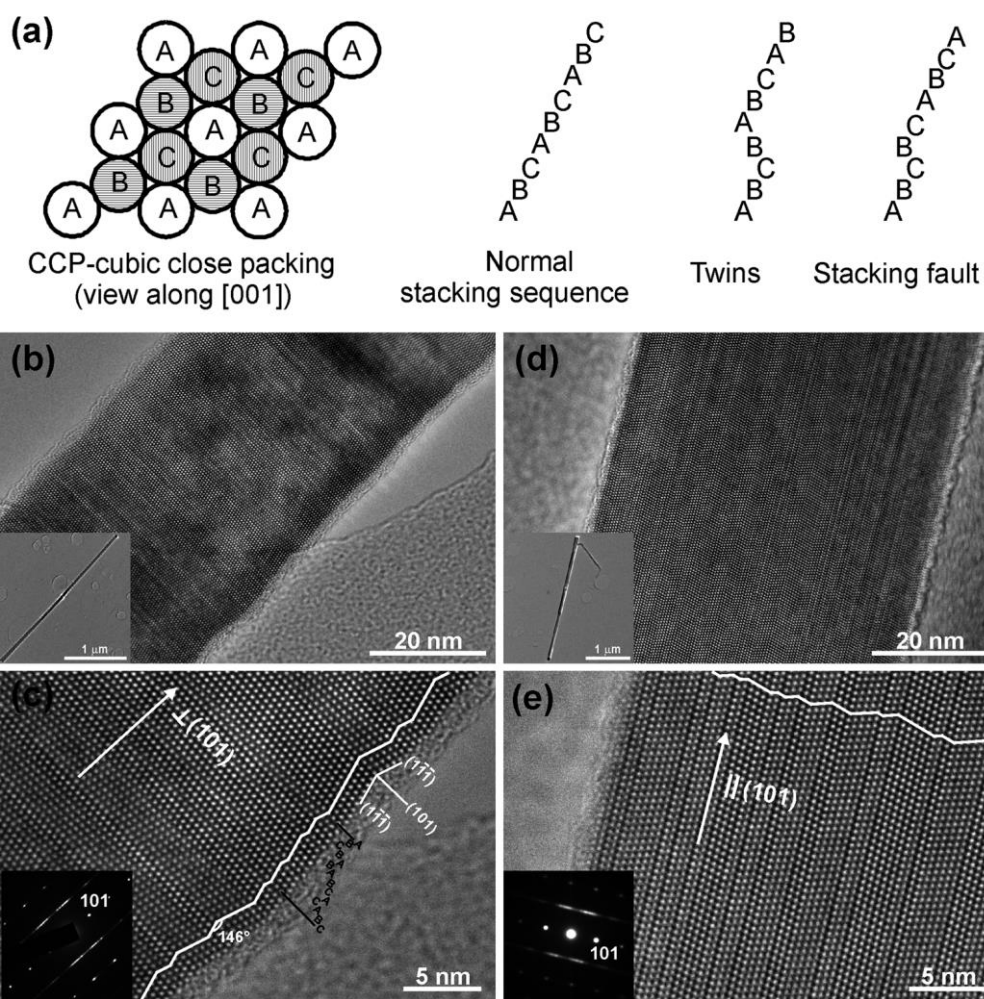


Figure 1.6: (a) Schematic drawing of CCP arrangement for a rhombohedral boron carbide with normal stacking sequence, twins and stacking faults; Transmission electron microscope (TEM) results of as-synthesized nanowire with transverse planar faults (b and c) and axial planar faults (d and e).<sup>103</sup>

Another issue worth noting is that the determination of planar defects is mostly based on the modulated contrast of high resolution TEM images and streaks appearing in diffraction patterns (DPs), which requires extensive and tedious TEM works. The model proposed by Zhe Guan *et al.*<sup>128</sup> on correlating the DPs and projected preferred growth direction of a nanowire helps to facilitate the process of identifying the types of planar defects that exist in the nanowires. In that model, the (001) planes were defined

as defect planes and three in-zone axes  $[100]$ ,  $[010]$  and  $[1\bar{1}0]$  (orange line in Figure 1.7), from which the defect planes  $(001)$  could be seen and three off-zone axes  $[001]$ ,  $[10\bar{1}]$  and  $[01\bar{1}]$  (blue line in Figure 1.7), from which the defect plane could not be seen. Based on the simulation results and experimental verification, two TF cases and three AF cases were obtained to help identify the stacking fault orientation of as-synthesized boron carbide nanowires when only off-zone data could be collected. Table 1.1 shows the five cases and the corresponding identification criteria. However, one question could be asked here is whether one can find an alternative and even quicker way to determine the planar defects of 1D nanostructures? The answer is conditionally yes and this will be discussed in detail in section 1.7.

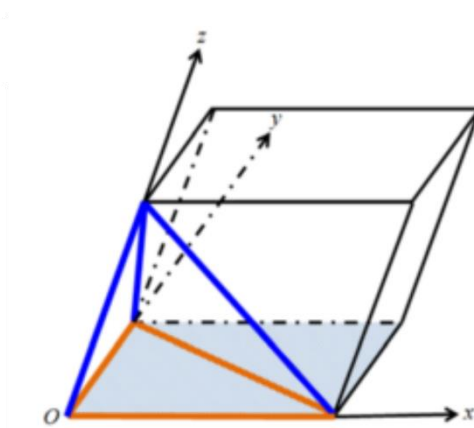


Figure 1.7: A schematic drawing of the rhombohedral unit cell with defined defect plane  $(001)$  being shaded, three in-zone axes  $[100]$ ,  $[010]$  and  $[1\bar{1}0]$  within the defect plane (orange lines) and three off-zone axes  $[001]$ ,  $[10\bar{1}]$  and  $[01\bar{1}]$  out of the defect plane (blue lines).<sup>128</sup>

Table 1.1: Five cases of determination of fault orientation within a nanowire when only off-zone TEM data are available<sup>128</sup>

Case No.	Zone Axis	Alignment of the projected preferred growth direction in the diffraction pattern
TF case 1	[001]	Through $\bar{1}\bar{1}0$ and 110 spots
TF case 2	[10 $\bar{1}$ ] [01 $\bar{1}$ ]	Through $\bar{1}0\bar{1}$ and 110 spots Through $0\bar{1}\bar{1}$ and 011 spots
AF case 1	[001]	Perpendicular to the tie line between $0\bar{1}0$ and 010 spots
AF case 2	[10 $\bar{1}$ ]	Perpendicular to the tie line between $0\bar{1}0$ and 010 spots
AF case 3	[01 $\bar{1}$ ]	Perpendicular to the tie line between $0\bar{1}\bar{1}$ and 011 spots

## 1.6 Kinked Nanowires

Since we have already understood the structural evolution in straight boron carbide nanowires, our focus in this dissertation is the kinked boron carbide nanowires. In this section, a brief overview of the research progress of the kinked semiconductor nanowires is presented.

The common “bottom up” synthesis methods developed to synthesize group IV, III-V semiconductor nanowires and metal oxide nanowires, including molecular beam epitaxy (MBE), chemical vapor deposition (CVD), chemical beam epitaxy (CBE) laser ablation, and thermal evaporation mainly apply one principle growth mechanism, i.e., vapor liquid solid (VLS) growth, which was first mentioned by Wagner and Ellis on investigating Au-catalyzed Si whisker growth.<sup>129,130</sup> In VLS growth, there are three main steps: (1) the metal catalysts (Au, Cu, Ti, Fe or In)<sup>131</sup> are prone to form liquid-alloy droplet as the precursor gas is being injected; (2) the liquid-alloy droplet will eventually become saturated when excess precursor gas decomposes and adsorbs on or into the droplet; (3) the whiskers or nanowires will then precipitate layer by layer

beneath the liquid-alloy droplet with continuous precursor gas supply. The best advantage of VLS is the guided growth, which is important for controlling the morphology of nanowires in order to fabricate functional devices.<sup>132</sup> Efforts were initially made to synthesize straight nanowires for axial nanowire based device.<sup>133,134</sup> However, by varying the reaction conditions (temperature, pressure and source gas), kinked nanowires were often accompanied by the growth of straight nanowires. As early as in 1960s, kinked or branched silicon (Si) micro-whiskers were observed.<sup>135</sup> Later in 1990s, kinked and curved Si nanowires were reported by J. Westwater and his coworkers.<sup>136</sup> After that, more and more kinked nanowires from other materials system have been synthesized and reported, for example germanium (Ge) nanowires,<sup>137-139</sup> III/V group nanowires (GaP,<sup>140</sup> InP,<sup>141-143</sup> InAs,<sup>144</sup> GaAs,<sup>145-147</sup> Zn<sub>3</sub>P<sub>2</sub><sup>148</sup>), oxide nanowires (SnO<sub>2</sub>,<sup>149,150</sup> In<sub>2</sub>O<sub>3</sub>,<sup>151-153</sup> Zn<sub>2</sub>GeO<sub>4</sub><sup>154</sup>) and some heterostructure nanowires<sup>155-157</sup>(Si/Ge, Si/GaP, GaAs/InAs, GaP/InP). In 2009, Charles Liber's group at Harvard reported a single crystalline kinked Si nanowires superstructure with controllable number of kinks and crystallographic direction by using proper growth parameters, as shown in Figure 1.8 (a) and (b). The growth direction of the synthesized nanowires switches from  $\langle 112 \rangle$  to  $\langle \bar{1}\bar{1}2 \rangle$  at each kink site to keep a fixed 120° angle joint. And based on those kinked nanowires, some novel nanodevices were designed and demonstrated, such as bioprobe FETs<sup>158-160</sup> and p-n diodes,<sup>161</sup> which raised the importance of kinked nanowires. Figure 1.8 (c) and (d) illustrates the general overview of the design and application of bioprobes made of kinked Si nanowires with the ability of deep penetrating and intracellular and extracellular recording. Besides controllable

synthesis, the underlying growth mechanisms of kinked nanowires are also of significant importance. Kinking of nanowires means the growth direction or orientation changes and is often caused by changing the reaction conditions (temperature and pressure). It was proposed that the instability at liquid-solid surface or surface migration of catalyst or liquid-solid droplet maybe responsible for kinks' formation in nanowires.<sup>162</sup> However, it still requires more works to better understand the kinked nanowires' crystal structures, growth mechanisms and properties in terms of both experimental and theoretical results.

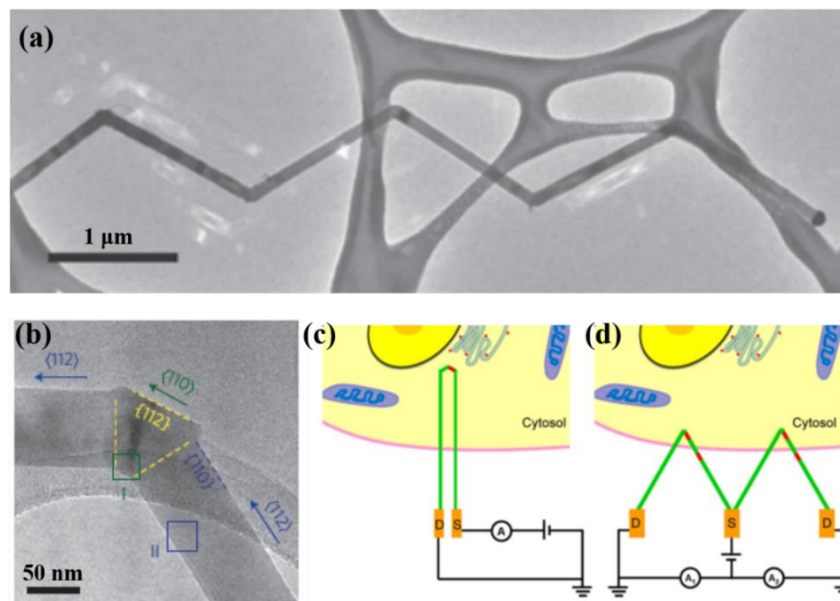


Figure 1.8: (a) Low magnification transmission electron microscope (TEM) image of a kinked Si nanowire with multiple number of kinks (b) Zoom in TEM image of the kink area showing the growth directions of two arms and transition part;<sup>161</sup> U-shaped bioprobe with integrated nanoFET (red) for intracellular recording (c) and W-shaped with multiple nanoFETs (red) bioprobe for simultaneous intracellular/extracellular recording based on kinked Si nanowires.<sup>159</sup>

### 1.7 Raman Spectroscopy on Individual Nanowires

In section 1.5, a question was raised on whether there is an alternative technique other than TEM to determine the planar defects of boron carbide nanowires effectively and quickly. Quick identification of boron carbide nanowires' defects and fault types will facilitate the mechanical and thermal test, which is important for establishing structure-property relationships. It was found that Raman spectroscopy might be an option. Due to its non-destructive and micro-spatial resolution, Raman spectroscopy is a powerful tool for rapid structural, compositional and properties characterization of individual nanowires.

A great number of Raman spectroscopy characterization works on individual nanowires have been reported in the last decade. Out of all, polarized Raman spectroscopy was most widely used to determine the growth direction of single GaN<sup>163</sup>, RuO<sub>2</sub><sup>164</sup>,  $\alpha$ - and  $\beta$ -Bi<sub>2</sub>O<sub>3</sub><sup>165</sup> and CdS<sup>166</sup> nanowires, to study the strain effect of single InAs<sup>167</sup>, Si<sup>168</sup> and GaN/AlN nanowires<sup>169</sup>, and to study the diameter dependent Raman scattering of single Si and AlN nanowires. In addition, the composition of single wurtzite and zinc-blend GaAs<sup>170</sup> and Al<sub>x</sub>Ga<sub>1-x</sub>As/GaAs<sup>171</sup> was analyzed by combining the compositional dependence of the Raman peaks with the existence of photonic modes in the nanowires. Moreover, both ordered stacking faults (polytypes, 2H and 9R) and disordered stacking faults in single Si nanowire identified by Raman spectroscopy with sensitivity to a few fault planes were reported by Lauhon's group.<sup>172,173</sup> One interesting finding of their studies is for kinked Si nanowires, the defects could evolve during growth, which could be characterized by Raman spectroscopy, as shown in Figure 1.9. Low magnification TEM image with inset DPs in Figure 1.9 (a) shows the

growth direction of the Si nanowire switched from  $\langle 111 \rangle$  to  $\langle 112 \rangle$  from left to right. By taking Raman spectra at the regions (green circle in Figure 1.9 (c) and (d)) with different growth directions, it was found that an extra Raman peak at  $\sim 495 \text{ cm}^{-1}$  showing up in the  $\langle 112 \rangle$  region. This finding was further confirmed by doing the Raman mapping of the nanowire via monitoring  $\sim 519 \text{ cm}^{-1}$  and  $\sim 495 \text{ cm}^{-1}$  bands. More recently, the polytypes formed by periodical twinning in individual Ge nanowire<sup>138,174</sup> was also confirmed using Raman spectroscopy.

Inspired by the success of identification of planar defects in individual Si and Ge nanowires by means of Raman spectroscopy, in this dissertation we have performed Raman spectroscopy studies on individual boron carbide nanowires to determine if there is any relationship between the stacking faults orientations/densities and Raman scattering.

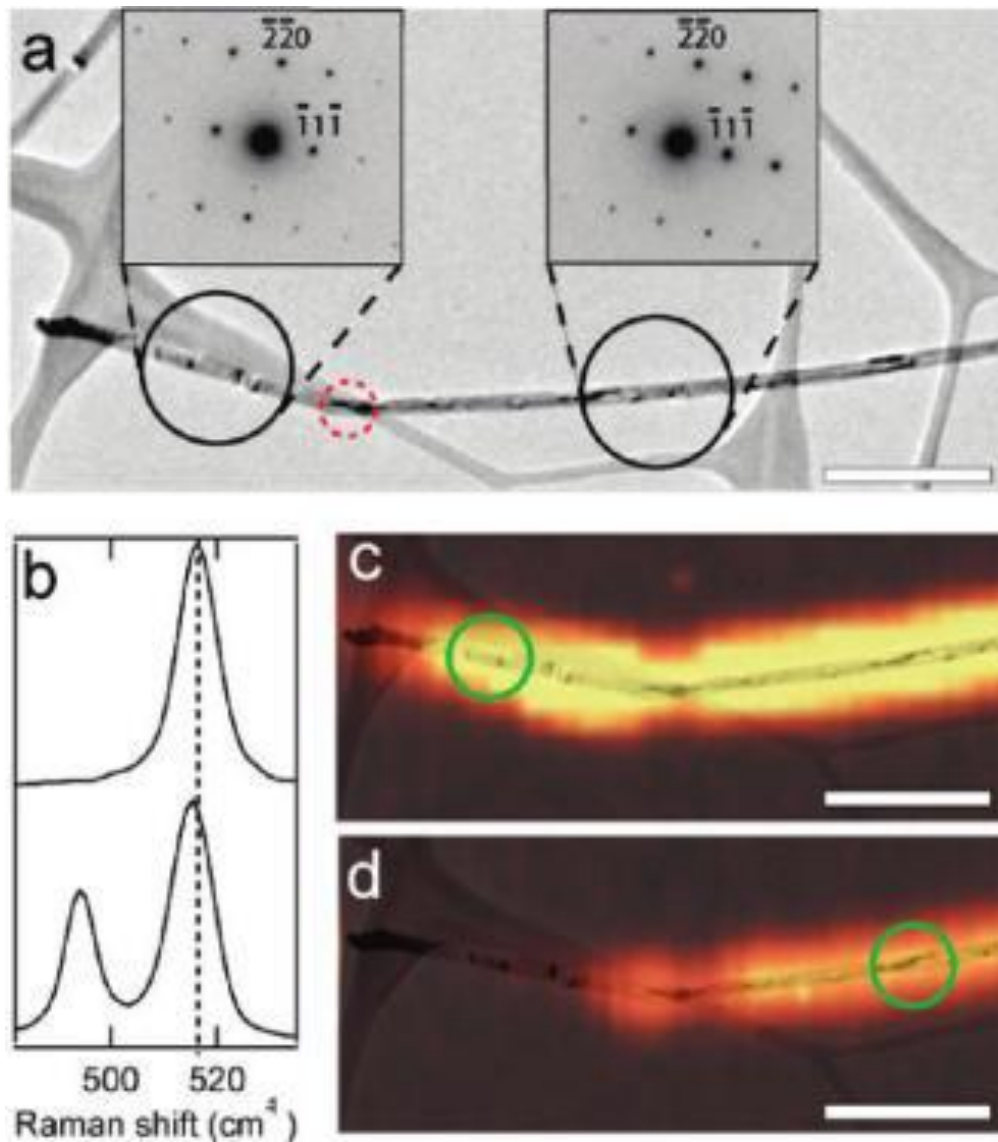


Figure 1.9: (a) Low magnification TEM image with inset diffraction patterns (DPs) from  $[112]$  zone axis showing the growth direction of the nanowire changed from  $\langle 111 \rangle$  to  $\langle 112 \rangle$  (left to right) at a kink (red circle). (b) Raman spectra taken from regions indicated by green circles in (c) and (d) (top and bottom, respectively). Raman intensity mapping of (c)  $\sim 519 \text{ cm}^{-1}$  and (d)  $\sim 495 \text{ cm}^{-1}$  bands. Scale bars are  $1 \mu\text{m}^{172}$

## 1.8 Objectives

As reviewed above, boron carbide nanowires have already been synthesized via carbothermal reduction method or CVD method and their crystal structure and thermal properties have been characterized by means of TEM examination and microthermal

measurement. However, no detailed microstructure-thermal property relation of boron carbide nanowire has been established so far. Particularly, there is no experimental study on the structural and thermal characterization of kinked boron carbide nanowires. Therefore, the general objective of this dissertation project is to explore a high temperature TE material—boron carbide nanowires (straight or kinked) and to understand their growth mechanisms, structure and thermal transport property relations. The approach is to integrate rational materials synthesis, transport property measurement on single nanowire, thorough structural characterization of samples before and after measurement, and theoretical analysis to understand structure-phonon transport property relation.

In Chapter 2, the details of the experiments and methods are described as well as the working principle of the instrument being used. In Chapter 3, the structural investigation of boron carbide nanowires, including the structural evolution of straight boron carbide nanowire before and after mechanical test and thermal test, and the detailed kinking behavior study in as-synthesized kinked boron carbide nanowires are presented. In Chapter 4, a thorough study of the thermal transport in individual boron carbide nanowires is presented. This part of work is done in collaboration with Dr. Deyu Li's group at Vanderbilt University. The thermal transport measurement was done by Li's group. The content discussed in the dissertation is extracted from a manuscript jointly prepared by the two groups. (Both myself and Mr. Qian Zhang from Vanderbilt University are first authors of the manuscript.). In this collaborative work, the effect of diameter, carbon concentration, stacking fault orientation, fault density and kink

morphology on the final thermal conductivity are explored. It is worth noting that, to the best of our knowledge, the reduction of thermal conductivity because of the presence of kink is verified experimentally for the first of time. In addition, Seebeck coefficient and electrical conductivity were measured as well as the  $ZT$  value of boron carbide nanowires was estimated. In Chapter 5, micro-Raman study on individual boron carbide nanowires was performed and presented. The experimental parameters were optimized to extract decent Raman signal due to the small Raman scattering cross section of boron carbide nanowires. The relationship between the stacking faults and Raman scattering was evaluated preliminarily. Chapter 6 presents the conclusions and future works.

## CHAPTER 2: EXPERIMENTS AND METHODS

In this chapter, the main focus is the discussion of the synthesis methods and characterization tools used for this dissertation work, including but not limited to the general working principles, components of the tools, and the operation parameters.

### 2.1 Chemical Vapor Deposition (CVD)

Chemical vapor deposition (CVD) is one of the few deposition processes for producing high quality coating and thin film initially and now is widely used in the field of low dimensional nanostructures' synthesis, such as 2D graphene, 1D carbon nanotube, and various nanowires.<sup>175-177</sup> A typical CVD process involves a series of gas-phase and surface chemical reactions close to or on a substrate while introducing source gas precursors into the reactor chamber, in which the decomposition of the precursors and subsequent reactions are usually activated or initiated by heating, high frequency radiation or plasma. Depending on the pressure inside the reaction chamber, the CVD can be further divided to three groups: atmospheric pressure CVD (APCVD), low pressure CVD (LPCVD) and ultrahigh vacuum CVD (UHVCVD), whose CVD processes are at atmospheric pressure (760 torr), sub-atmospheric pressures ( $\sim 10^{-3}$  torr) and very low pressure (typically below  $\sim 10^{-8}$  torr) respectively.<sup>178</sup>

In the case of synthesis of our boron carbide nanowires via co-pyrolysis of dibo-

thane ( $B_2H_6$ ) and methane ( $CH_4$ ), a home-built LPCVD system was developed and unitized. Here based on the schematic drawing of our LPCVD system shown in Figure 2.1, the general components of a CVD setup are briefly illustrated.<sup>179</sup> Gas delivery system, which supplies the precursors and carrier gas to the reactor chamber, is presented in the right dashed square, in which 1-3 denotes the gas cylinder for  $B_2H_6$ ,  $CH_4$  and Ar respectively, whose flow rates are regulated by each gas flow controller (4-6). The blue dashed square highlights another important component, furnace and reactor chamber. The reactor chamber usually is a quartz or alumina tube, and the heating is provided by the electrical furnace with a thermocouple (indicated by the red line) inserted at the center with sensor placed between the heater and tube. The target heating temperature can be set in the temperature controller, which is a proportional-integral-derivative controller (PID controller) controlling the power switch and solid state relay. The thermocouple measures the instant temperature of the heating zone during the heating process and sends the information to the temperature controller, which maintains a stable power supply to the furnace when the target temperature is reached. The third part of the LPCVD system is the vacuum system, which includes a pressure gauge placed downstream measuring the pressure of the chamber (tube), a vacuum trap close to the outlet of the chamber condensing additional vapors inside the system to enhance the vacuum level, a mechanical pump providing vacuum for the whole system, and a bubbler used for releasing pressure when venting the chamber.

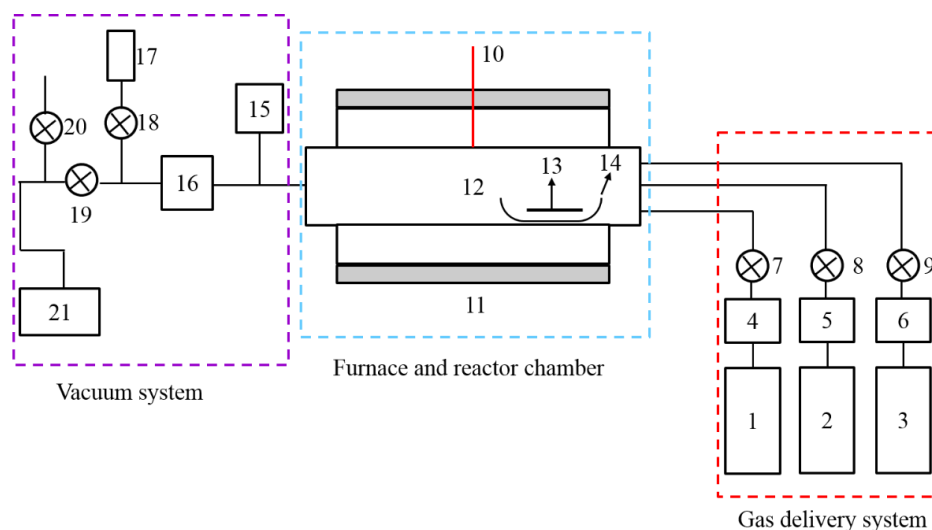


Figure 2.1: Schematic drawing of the LPCVD system. Gas delivery system: 1-3 denotes gas cylinder for  $B_2H_6$  (precursor gas),  $CH_4$  (precursor gas), Ar (carrier gas) respectively; 4-6 are gas flow controllers; 7-9 are valves. Furnace and reactor chamber: 10 denotes thermocouple; 11 is the furnace; 12 is a quartz or alumina tube; 13 is the substrate; 14 is a quartz or alumina boat. Vacuum system: 15 denotes pressure gauge; 16 is a vacuum trap; 17 is bubbler; 18-20 are valves; 21 is the vacuum pump.<sup>179</sup>

In our LPCVD system, the highest temperature locates at the center of the furnace. The measured heating temperature goes down gradually as the thermocouple moves away from the center and drops to the lowest at the two ends of the tube.<sup>179</sup> The position dependent morphology and crystal structures of boron nanostructures synthesized by this method were carefully investigated by my former groupmate, Zhe Guan.<sup>179</sup> Three substrates coated with nickel (Ni) were placed close to the tube's right inlet where precursor gases ( $B_2H_6$  and  $CH_4$ ) were injected through, as shown in Figure 2.2 (a). The temperature distribution trend is  $T_3 > T_2 > T_1$ . In addition, the decomposition rates of  $B_2H_6$  and  $CH_4$  are different. The  $B_2H_6$  decomposed quickly and completely once entering the tube while  $CH_4$  needs more time and higher temperature

to be fully decomposed. Therefore, the boron content is higher at the inlet while carbon content is higher a little away from the inlet (substrate #3 position), as indicated by the dotted and dashed curve in Figure 2.2 (a). The CVD process is extremely sensitive to the temperature and the content of source precursors and so are the morphology and crystal structures of final products. Three different types of crystalline boron nanostructures were found on the above three substrates: substrate #1,  $\alpha$ -tetragonal boron nanoribbons and nanoplatelets; substrate #2, tapered and short boron carbide nanostructures; substrate #3, boron carbide nanowires with high aspect ratio.

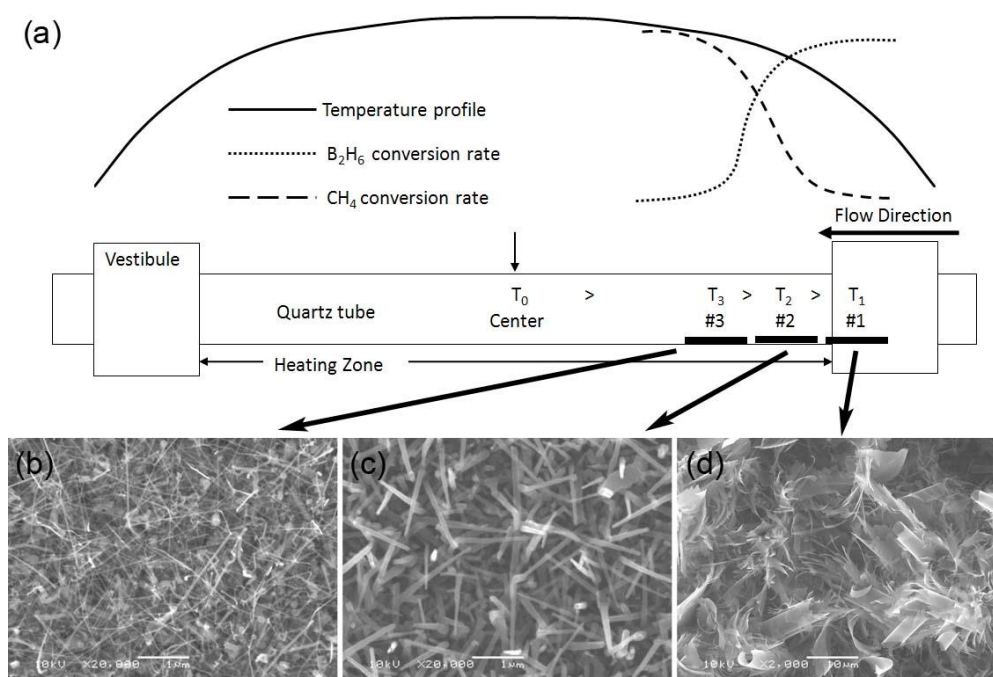


Figure 2.2 (a) schematic drawing of the arrangement of the three substrates, temperature profile and concentration profiles within the tube; the SEM images of the products at position #3 (b), #2 (c), and #1 (d) respectively.<sup>103</sup>

In this work, our focus is the straight and kinked boron carbide nanowires synthesized at position #3. The heating temperature is between 950 and 1050 °C and Nickel (Ni) was used as catalyst material and coated onto Si/SiO<sub>2</sub> or sapphire substrates via sputter coating. The detailed synthesis procedures and parameters could be found elsewhere.<sup>103,179</sup>

## 2.2 Scanning Electron Microscope (SEM)

The resolution of light microscope is determined by the formula of Ernst Abbe:<sup>180</sup>

$$\text{resolving power} = \frac{0.61\lambda}{N.A.} \quad (2.1)$$

where  $\lambda$  is the wavelength of light and  $N.A.$  is numerical aperture of the lens. A useful rule of thumb for light microscope is that theoretical maximum resolution is  $\lambda/2$ . Therefore, as the wavelength of the light gets smaller, the resolving power becomes better. The visible light ranges from 400 nm to 700 nm. Current most modern light microscope enables the eye to resolve objects separated by as small as 100 nm via using shorter light with a shorter wavelength and reducing the numerical aperture together.

However, with a great demand of seeing features less than 100 nm or even smaller as the rapid development of nanomaterials, alternative microscopy tools are in need. It is well known that the wavelength of electrons depends on the accelerating voltage, for example, it is 0.009 nm when the accelerating voltage is 20 KV if ignoring relativistic effects from the following equation:

$$\lambda = \frac{1.22}{\sqrt{E}} \quad (2.2)$$

Obviously, the electron microscope would have higher resolution than the light microscope in terms of much shorter wavelength according to equation (2.1). Moreover, it is discovered the accelerated electrons behave much like light in vacuum and electric and magnetic fields could be used to shape and focus the electron beam path. SEM uses high-energy electrons instead of light for imaging via raster scanning the surface of the specimens, which is an advanced tool for high-resolution imaging of specimens in small scale. Comparing with traditional light microscope, the additional advantages of SEM include much higher magnification and larger depth of field, which are able to produce images representing 3D structure of the sample.

A typical SEM consists of electron gun, alignment coil, vacuum column, condenser lenses, objective lens, scan coil, objective lens aperture, specimen chamber and secondary electrons detector, which are all shown in Figure 2.3. Electron gun, on top of the column, is used to generate a beam of incident electrons with energy ranging from 0.1 to 30 KeV. Two types of electron guns are generally used, thermionic gun (hairpin tungsten and LaB<sub>6</sub>) and field emission gun (FEG). The characteristic properties and performance of four typical electron guns are summarized in Table 2.1. The source size of FEG is much smaller than that of thermionic guns, which enables a better resolution in SEM with FEG. As mentioned earlier, accelerated electrons only behave like light in vacuum, which requires the column and specimen chamber in a good vacuum level with the help of diffusion pump in order to focus electrons emitted from the gun onto the surface of the specimen with an even small probe size (0.4-5 nm)

through a series of electromagnetic lenses (two condenser lenses and one objective lens) and a set of scanning coils near the end of the column.

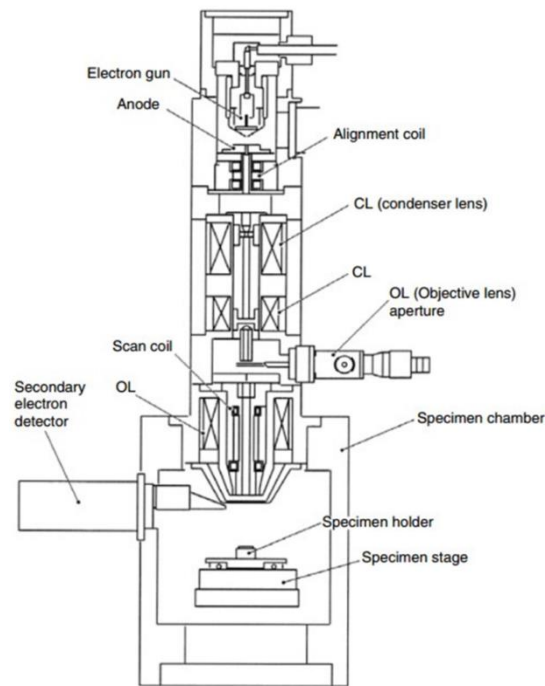


Figure 2.3: Schematic diagram of a SEM showing its key components<sup>181</sup>

Table 2.1: The characteristic properties of four typical guns: Tungsten, LaB<sub>6</sub>, Schottky FEG and Schottky FEG<sup>180</sup>

	Tungsten	LaB <sub>6</sub>	Schottky FEG	cold FEG
Brightness (A/cm <sup>2</sup> sr)	10 <sup>6</sup>	10 <sup>7</sup>	5*10 <sup>8</sup>	10 <sup>9</sup>
Operating temperature (K)	2700	1700	1700	300
Crossover Size (nm)	10 <sup>5</sup>	10 <sup>4</sup>	15	3
Energy spread (eV)	3	1.5	0.7	0.3
Current stability (%/hr)	<1	<1	<1	5
Vacuum (Torr)	10 <sup>-5</sup>	10 <sup>-7</sup>	10 <sup>-8</sup>	10 <sup>-11</sup>
Lifetime	100	1000	>5000	>5000

When the electrons beam reaches onto the surface of the sample, the electrons-matter interaction (elastic and inelastic scattering) happens, which results in different types of signal from different volumes of interaction. The size of the interaction volume extending from 100 nm to 5  $\mu\text{m}$  depends on many factors, including electron energy, atomic number and density of the specimen. As shown in Figure 2.4, Auger electrons (AE), secondary electrons (SE), backscattered electrons (BSE) and characteristic X-rays are the typical signals collected by specific detectors for topography and composition analysis. In most cases, SE is collected for imaging the true surface structure of a specimen due to its relative small escape depth ( $\sim 50$  nm).

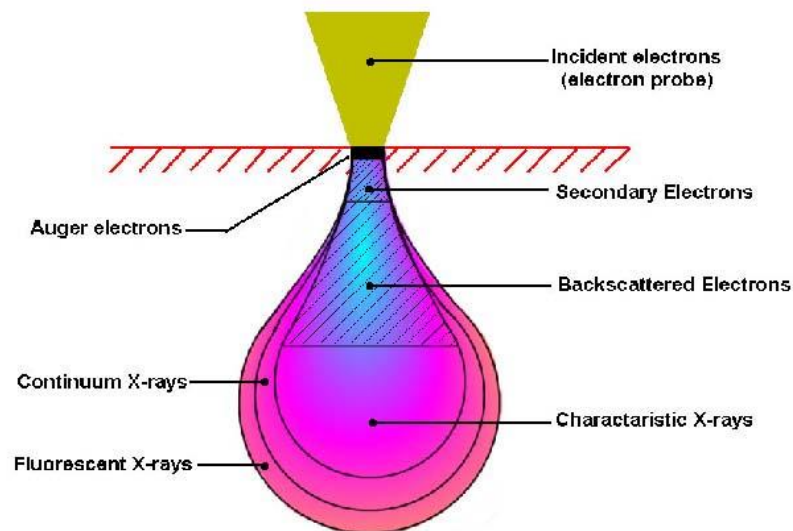


Fig. 2.4 Electron beam interaction diagram showing different types of electrons and X-rays ejected from the surface of the specimen<sup>182</sup>

In the real practice operation of SEM, acceleration voltage, working distance, and spot sizes are three important parameters affecting get high resolution and high quality SEM images if the alignment is good. In our work, a JSM-6480 SEM from JEOL with has a thermionic hairpin tungsten gun, a spatial resolution at 30 kV of 3 nm for SE imaging, and 4 nm for BSE imaging, was used to characterize the morphology of boron carbide nanowires. The acceleration voltage, working distance and spot size was chosen as 10 KV, 10, and 30 nm respectively.

### 2.3 Transmission Electron Microscope (TEM)

TEM is another type of electron microscopes being used in examining nanostructures and is extensively used in this work. The accelerating voltage in TEM is quite high, usually 80-300 KV, which brings electrons beam with high energy and extremely short wavelength. If recalling Equation (2.1), it would be easily to conclude the resolution of TEM will be even better than SEM's and it is true in reality. Different from raster scan of a fine electron beam probe in SEM, the parallel electron beam is transmitted through the ultra-thin specimen (less than 500 nm) and then the transmitted electrons are collected and focused for imaging in TEM. For high resolution TEM (HRTEM) imaging, the specimens' thickness should be less than 100 nm. Therefore, the general purpose of TEM sample preparation is to make the sample as thin as possible, which are difficult. Several methods have been developed on TEM sample preparation, for example precision ion polishing (PIP), focused ion beam (FIB) thinning, and ultramicrotome cutting.<sup>180</sup> In the case of our boron carbide nanowires, whose diameters are usually less than 100 nm, the thickness is not an issue. Individual

nanowires are transferred onto the TEM grid. Our approach is to transfer a bunch of boron carbide nanowires from the donor substrate onto a PDMS receiver substrate via dry contact printing method. The individual nanowires are later picked up with a micromanipulator and then moved onto the mesh slot of the TEM grid.

There are two basic operation modes of the TEM imaging system, as shown in Figure 2.5. One is diffraction mode, in which the electron diffraction pattern (EDP) forming at the back focal plane (BFP) is projected onto the viewing screen or CCD camera. The other is image mode, in which the image of the object forming at the imaging plane is projected. In combination of EDP and TEM image, the structural and morphological information of the examined samples could be obtained. By inserting a selective area aperture (SA) at the image plane of the objective lens, the EDP from a specific area of the sample could be recorded, which is called SAEDP. Most of the EDPs shown in this dissertation are SAEDPs. In addition, with the help of objective aperture locating at the BFP, bright field (BF) and dark field (DF) TEM images are produced by selecting the direct-beam electrons and scattered electrons respectively.

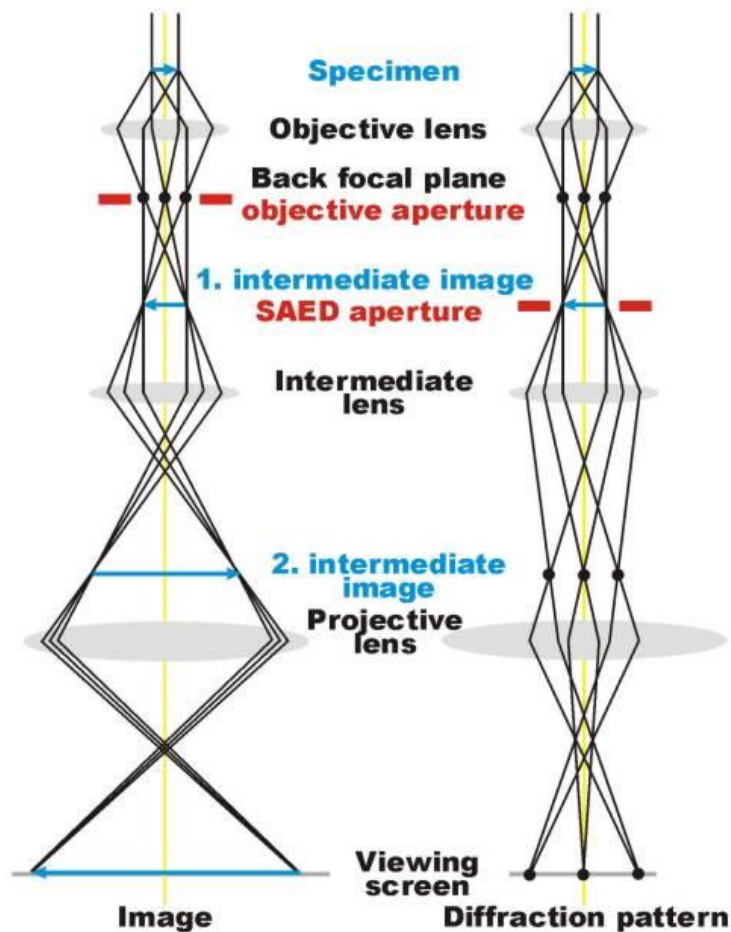


Figure 2.5: Schematic and simplified ray diagram of two basic operation modes in TEM: image mode (left) and diffraction pattern mode (right)<sup>183</sup>

A JEOL JEM-2100 LaB<sub>6</sub> TEM operating at 200 kV acceleration voltage was used to record BF TEM images, DF TEM images, HRTEM images and SAEDPs of boron carbide nanowires. A JEOL double-tilt holder and a Gatan double-tilt holder were used for large angle tilting ( $\pm 30^\circ$  in both X and Y directions).

#### 2.4 Energy Dispersive X-ray Spectroscopy (EDX/EDS)

As shown in Figure 2.4, X-rays including characteristic X-rays, continuum X-rays (Bremsstrahlung), Fluorescent X-rays (cathodoluminescence) could be produced

as a result of the electron-matter interaction. Out of them, characteristic X-rays carry energy directly related with the atoms' orbital electrons transitions between inner shells. Figure 2.6 (a) presents the schematic drawing of the production of characteristic X-rays, in which, three steps are involved: first, an electron in an inner shell is knocked out by the incident high energy electron beam; second, a hole is generated in that shell; then an electron from the one of the outer shells transition to the hole in the inner shell with excess energy being emitted as a characteristic X-ray. The characteristic X-rays are named depending on the shell in which hole is generated and the shell from which an electron fills the hole, For example, the transition from the electrons in L, M and N shell to the vacancy in K shell emits K lines, including  $K_{\alpha}$ ,  $K_{\beta}$  and  $K_{\gamma}$ . Figure 2.6 (b) also presents the other possible characteristic X-rays, such as  $L_{\alpha}$ ,  $L_{\beta}$  and  $M_{\alpha}$ . Moreover, it taking the energy degeneration at each shell into consideration, the case shown in Figure 2.6 (a) emits  $K_{\alpha 3}$  X-ray.

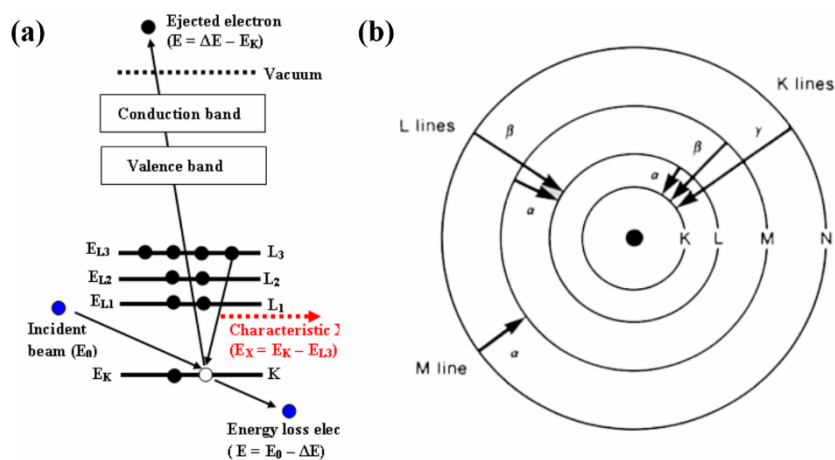


Figure 2.6: (a) Schematic drawing of a characteristic X-ray generation process; (b) Different characteristic X-rays between inner and outer shell.<sup>184</sup>

EDX/EDS usually combined with SEM/TEM collects those characteristic X-rays signals with the help of a semiconductor based detector consisting of a collimator, an electron trap, a window, a semiconductor crystal and the electronic components, which allows one to identify the composition elements with atomic numbers from 4 to 92 and their atomic percentage within the specimen.<sup>185</sup> In our work, boron with atomic number 5 and carbon with atomic number 6 are able to be detected by an INCA energy dispersive X-ray spectroscopy (EDS/EDX) system from Oxford Instruments, which has a Si(Li) detector cooled down to liquid nitrogen temperature to reduce electronic noise. With integration to the TEM, we are able to identify the local composition along the individual nanowires by focusing the electron beam with a diameter smaller than the boron carbide nanowires' diameters. One more thing need to mention is current most advanced EDX system (i.e. FEI super X) coupled with aberration corrected STEM could produce element mapping of nanostructures with atomic spatial resolution.

### 2.5 Electron Energy Loss Spectroscopy (EELS)

EELS, which collects and analyzes the inelastic scattering electrons transmitted through the ultrathin specimens, is a strong complementary technique to EDX/EDS for identifying elements (especially light elements) quantitatively and qualitatively. The energy resolution of EELS ( $<1$  eV) is much better than that of EDX/EDS ( $>100$  eV), which results in a more accurate analysis of the composition elements and atomic percentage. Besides elemental identification, EELS provides an additional tremendous amount of information on specimen atoms' fine chemistry and electronic structures,

including but not limit to, bonding/valence state, the nearest-neighbor atomic structure, the free electron density and the specimen thickness.<sup>180</sup>

A magnetic prism spectrometer mounted below the viewing screen is indispensable in order to collect the electron energy loss spectrum, as shown in Figure 2.7 (a). The magnetic prism actually has an electrically isolated drift tube, in which electrons beam is directed by the magnetic field. And the electron beam could be selected by an entrance aperture with variable size mounted above the entrance of the magnetic prism. A schematic ray path of electrons passing through a magnetic prism is shown in Figure 2.7 (b), in which the electron beam was deflected by a  $90^\circ$  angle. The dispersing and focusing of zero loss and energy loss electrons in the image plane are different. Electrons that have lost energy travelling with a smaller speed and deflected further (dashed line in Figure 2.7 (b)).<sup>186</sup> But the on-axis and off-axis electron beams suffering same energy loss could be brought back to a focus in the image plane, where the detector locates to obtain the final EELS spectrum.

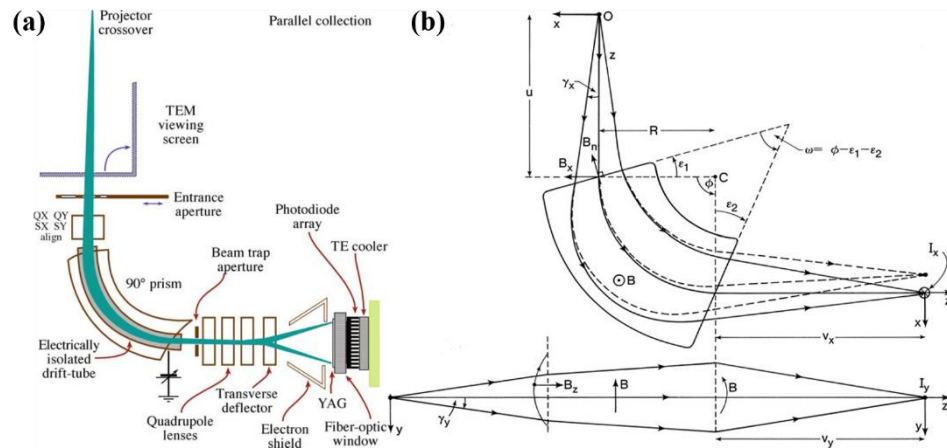


Figure 2.7: (a) Schematic drawing of the configuration TEM-EELS and the collection of energy loss spectrum by a YAG based detector;<sup>180</sup> (b) Ray paths of electrons travelling through a magnetic prism.<sup>186</sup>

Figure 2.8 presents a typical EELS spectrum, which is separated into two parts: one low loss region ( $<50$  eV) and one core (high) loss region ( $>50$  eV). In the low loss region, the intense zero-loss peak mainly comes from the electrons going through an elastic scattering process or even without interacting with the specimen, while the plasmon peak actually results by a longitudinal wavelike oscillation from weakly bound conduction and valence-band electrons.<sup>180</sup> As moving to the core (high) loss region, primary elemental information related to tight bounding electrons, core-shell electrons and distribution could be extracted from the spectrum. In order to ionize an atom, a critical energy needs to be transferred from the incident electron beam to the electron being kicked out, which is shown as the ionization energy edge of specific atom. For example, N-K edge, Ti-L<sub>1,2,3</sub> edge and O-K edge are identified the EELS spectrum in Figure 2.8.

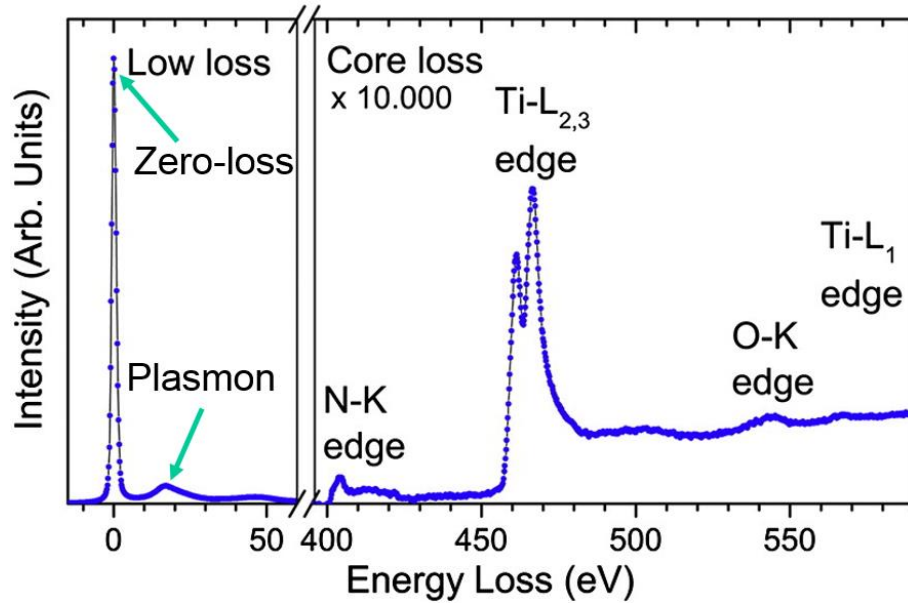


Figure 2.8: A typical EELS spectrum including both low loss and core loss regions from a  $\text{Ti}_2\text{Al}(\text{O},\text{N})$  phase layer.<sup>187</sup>

## 2.6 Micro-Raman ( $\mu$ -Raman) Spectroscopy

From the theory, the lattice vibration in crystals or molecular vibration in chemicals with a vibrational frequency  $\omega_j$  will mediate with the electric moment  $P = \epsilon_0 \chi_0 E_0$  resulted by the electric field  $E = E_0 \exp[i(k_i \cdot r - \omega_i)]$  when the interaction between light and crystal happens at position  $r$ . The induced electric moment after interaction could be described by the following equation:<sup>188</sup>

$$P = \epsilon_0 \chi_0 \cdot E_0 \exp[i(k_i \cdot r - \omega_i)] + \epsilon_0 E_0 \left( \frac{\partial \chi}{\partial Q_j} \right)_0 A_j \times \exp[-i(\omega_i \pm \omega_j)t] \exp[i(k_i \cdot r \pm q_i) \cdot r] \quad (2.3)$$

It is the electrical susceptibility  $\chi$  that is actually changed by lattice vibrations characterized by a normal coordinate  $Q_j = A_j \exp[i(q_j \cdot r - \omega_j t)]$ . To be more straightforward, moment shown in Equation (2.3) could be simplified as:<sup>189</sup>

$$P = P(\omega_i) + P(\omega_i + \omega_j) + P(\omega_i - \omega_j) \quad (2.4)$$

in which the first term denotes the elastic scattering of the light (Rayleigh scattering), which shares the same frequency as the incident light; the second and third term correspond to the inelastic scattering of light, whose frequency is either larger (anti-Stokes Raman scattering) or smaller (Stokes Raman scattering) than that of incident light. Figure 2.9 schematically shows the three types of scattering using an energy-level diagram.

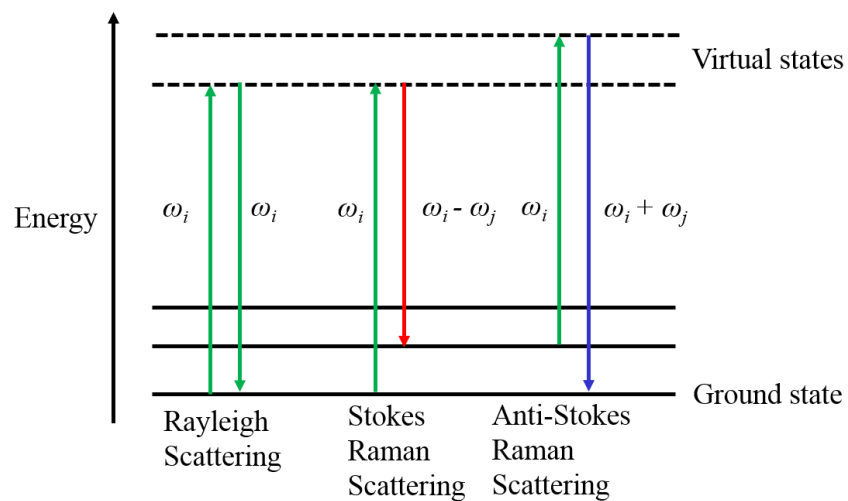


Figure 2.9: Schematic energy-level diagram showing the process of Rayleigh scattering and Stokes and anti-Stokes Raman scattering.

Raman spectroscopy, which measures the inelastic scattering of light, has been successfully used in- and ex-situ studies of materials in different states (solid, liquid and gas). For solid state crystalline materials, their mechanical stress, crystallographic orientation, doping and even composition could be evaluated non-destructively and

efficiently by Raman spectroscopy, since lattice vibrations or phonons are sensitive to those internal and external perturbations.<sup>188</sup> However, not every lattice vibration in the crystal can be probed via Raman spectroscopy because of the selection rule  $\left(\frac{\partial\chi}{\partial Q_j}\right)_0 \neq 0$ , which depends on crystal symmetry. Moreover, with integration of advanced microscope objective lens to focus the incident laser, the final laser spot shining on samples could be as small as  $\sim 750$  nm (for 100x objective lens), which raises the development of micro-Raman spectroscopy for the analysis of a small sample area or volume (even in nanoscale). The general setup of a micro-Raman spectrometer in a backscatter configuration is shown in Figure 2.10. The incident laser light could be ultraviolet (335 nm), blue (441 nm), green (532 nm) or red (633 nm). By choosing appropriate notch filters, the cut off Stokes edge could be tuned. The confocal hole here is used to enhance the spatial resolution with scarifying part of the signal. In this work, a LabRAM HR800 micro-Raman spectrometer from Horiba with a green laser (532 nm) excitation source was used to characterize individual boron carbide nanowires. The details will be discussed in Chapter 5.

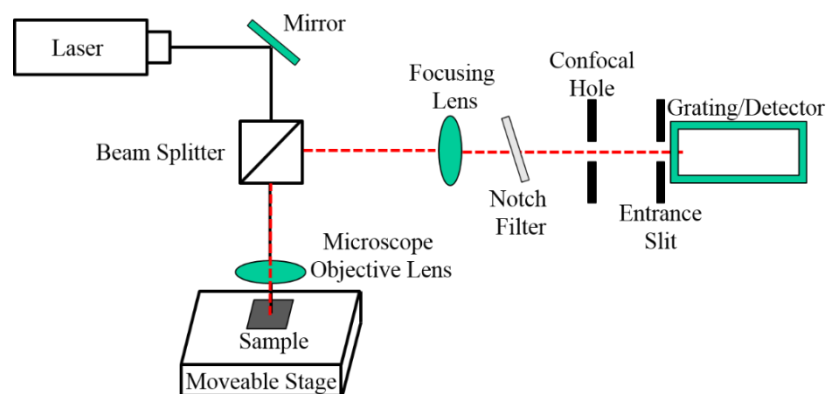


Figure 2.10: Schematic drawing of a micro-Raman spectrometer.

## 2.7 Micro-device for Thermal Conductivity Measurement of Individual Nanostructures

The traditional thermal conductivity measurement methods and devices are not able to deal with samples in nanoscale length, for example 1D nanotubes, nanowires, and nanoribbons, which all have unique thermophysical properties deserving well investigations. To address this issue, several novel methods including suspended micro-devices,<sup>84,190</sup> joule heating<sup>191</sup> and micro-Raman spectroscopy,<sup>192</sup> have been developed to measure the thermal properties of individual 1D nanostructures. Out of them, the suspended micro-devices are more popular and widely used. Here the components and working principles of the suspended micro-devices is briefly discussed.

As shown in Figure 2.11 (a), the micro-device consists of a resistive platinum heater ( $R_h$ ) and a resistive platinum thermometer ( $R_s$ ) patterned on two suspended silicon nitride ( $\text{SiN}_x$ ) membranes separated with a 2~6  $\mu\text{m}$  space. Six long (420  $\mu\text{m}$ ) and narrow (3  $\mu\text{m}$ ) beams are used to support each membrane and to ensure minimal heat loss from the sample to the ambient environment. Furthermore, a thin  $\text{SiO}_2$  layer could be patterned covering the Pt resistor only, which serves to avoid the nanowire contacting the Pt resistor electrically. By flowing a direct current  $I_{dc}$  through two beams to the Pt heater, the thermal conductance  $G_s$  of 1D nanostructures (nanowires, nanotubes) bridging the gap is measured. The resistances of heating and sensing membrane are both measured by 4-point I-V method, which is enabled by connecting the resistor to four contact pads through metal lines lying on the suspended beams. A smaller AC current ( $i_{AC} < 0.5 \mu\text{A}$ ) passes through the other two beams and a lock-in amplifier measures voltage drop across the platinum coil. In this way, the measurement

sensitivity is  $\sim 1$  nW/K.<sup>193</sup> With knowing the thermal conductance, the thermal conductivity could be calculated based on the following equation:

$$\kappa_s = \frac{G_s L}{A} \quad (2.5)$$

where  $A$  is the area of the sample's cross section and  $L$  is the suspend length between the membrane. Moreover, the Seebeck coefficient and electrical conductivity could also be measured using this micro-device, which in turn leads to the calculation of figure of merit ( $ZT$ ).<sup>193</sup>

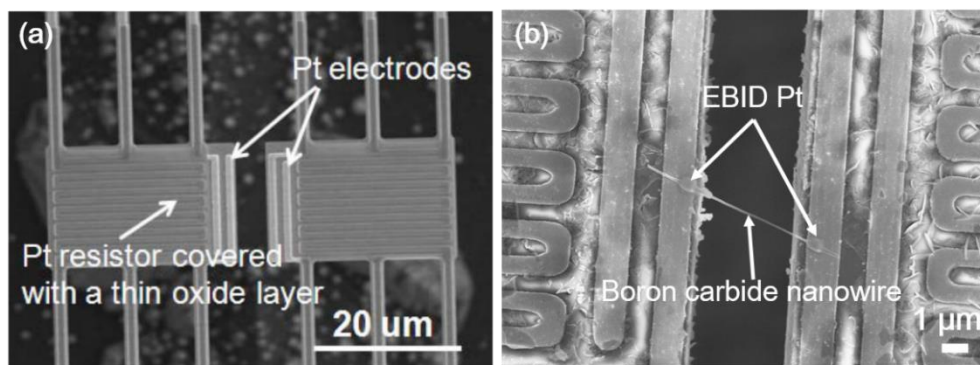


Figure 2.11: SEM photographs of (a) a microdevice and (b) a microdevice with a boron carbide nanowire on it. (Courtesy of Li's group )

Using a micro-manipulator, an individual boron carbide nanowire could be placed to bridge the two separated membranes. In order to enhance the thermal contact between the boron carbide nanowire and suspended device, platinum (Pt) contact pads were locally deposited at the nanowire-Pt electrodes junctions via electron beam induced deposition (EBID) performed in the SEM, as shown in Figure 2.11 (b). Currently, the micro-device being used is etched through to facilitate the TEM

examinations after thermal conductivity measurement. In addition, an extra radiation shield is directly mounted on the sample holder inside the cryostat in our setup, which could further reduce the heat loss to the surrounding environment.

## CHAPTER 3: STRUCTURAL INVESTIGATION OF BORON CARBIDE NANOWIRES

### 3.1 Structural Aspects on Establishing True Structural and Properties Relations of Boron Carbide Nanowires

Individual nanowires subjected to mechanical properties and thermal properties test need to be clamped firmly or be in good contact with the micro-device. The current widely used approach is to deposit carbon or platinum by means of EBID in the SEM.<sup>194-197</sup> The diameter information is mostly obtained from the recorded SEM images directly without any pre- or post-test TEM examination. However, due to the low resolution of SEM, the dimensional data measured from the SEM images would bring large errors in the calculation of the final Young's modulus and thermal conductivity. In addition, amorphous layer and additional contaminants might build up along the nanowire during the EBID process as well. However, the SEM is not able to distinguish such tiny structural change, which will also greatly impact on the data analysis. Moreover, most of the calculations assume the cross section of the nanowires is in a circular shape since it is really difficult to evaluate the cross section of nanowires experimentally. But in actual case, the nanowires' cross section varies, such as rectangular, hexagonal, octagonal and even irregular polygons. Here we address those issues by examining the boron carbide nanowires using the TEM before and after test and by looking into the cross section using both SEM and TEM.

### 3.1.1 The Effect of EBID

As introduced in section 2.7, a specific micro-device was utilized for testing the thermal properties of individual boron carbide nanowires. A single nanowire is firstly placed on the micro-device with two ends touching the two membranes respectively via a micromanipulator under optical microscope, and then the whole piece will be transferred to the SEM chamber for subsequent EBID of platinum to enhance the contact between the nanowire and platinum pad. Figure 3.1 (a) shows the SEM image of the micro-device with suspended nanowire right after EBID. Two square shape platinum contacts could be seen on the membranes and the magnified SEM image of one contact is shown in Figure 3.1 (b). The nanowire looks uniform and smooth and its diameter is measured as 85 nm from this SEM image. After thermal test, the micro-device could be examined by TEM since the bottom is etched through. Figure 3.1 (c) shows the low magnification TEM image of whole length of the nanowire bridging across the two membranes on the micro-device. Here phase contrast and thickness contrast are clearly seen. In addition, by magnifying the nanowire, the amorphous layer and platinum nanoparticles are observed, as shown in Figure 3.1 (d). It is evident that the diameter measured from SEM image including the thickness of the amorphous layer is larger than the actual diameter. In addition, due to low resolution of SEM and relative small size of boron carbide nanowire, it is believed that TEM will give more reliable measurement of the wire diameter. From Figure 3.1 (d), the diameter including amorphous layer is 68 nm and the core diameter excluding amorphous layer is 59 nm. Both are smaller than that obtained from SEM. Referring to the Equation (2.6), the

thermal conductivity is inversely proportional to the area ( $A$ ) of the cross section, which directly depends on the diameter of the nanowire. In this case, the thermal conductivity could have been overestimated around 36% or 52% if we only performed SEM examination. Therefore, it is of significance to examine every nanowire subjected to the subsequent properties test. Figure 3.1 (e) and (f) display another nanowire's structural change before and after EBID under TEM. By aligning the two images, the much thicker amorphous layer and platinum nanoparticles are more clearly visualized. Since the platinum nanoparticles are only physically adsorbed on the surface, they will not influence the phonon transport in the nanowire. And the dimensional information of all our thermal tested boron carbide nanowires are taken from TEM images, which ensure our thermal conductivity data are computed with minimal errors.

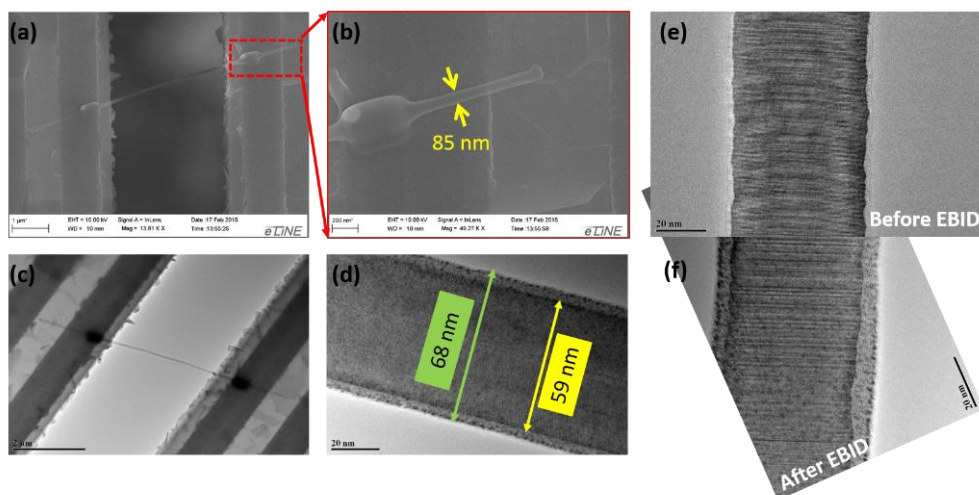


Figure 3.1: SEM images ((a) and (b), courtesy of Mr. Qian Zhang) and TEM images ((c) and (d)) of a same nanowire on a micro-device after EBID, (e) and (f) comparison between another nanowire's amorphous layer before and after EBID.

Besides individual nanowires' thermal conductivity measurement, its mechanical properties are also investigated in our group. An example of measure single nanowire's Young's modulus via vibration test is shown in Figure 3.2 (a). The test is done with help of a home-built nano-manipulator under SEM, which is also capable to perform tensile, compression and buckling test. No matter what kind of tests, the nanowire should be firmly bonded with the tungsten tip. Figure 3.2 (b) shows the EBID area, where carbon was deposited to secure the nanowire with the tip. By identifying the resonant frequency ( $f$ ) of the vibration, the Young's modulus could be calculated based on the following equation:<sup>198</sup>

$$E = \frac{4\pi^2}{\beta_0^4} \rho \frac{L^4 A}{I} f^2 \quad (3.1)$$

where  $\rho$  is the density,  $L$  is the effective length,  $A$  is the area of the cross section,  $I$  is the area moment of inertia, and  $\beta_0$  is the eigenvalues obtained from the following equation:

$$\cos \beta_0 \cosh \beta_0 - 1 = 0 \quad (3.2)$$

Before the vibration test, the nanowire was examined by TEM to identify the fault type, fault density, diameter and length, similar as what we have done for the nanowires for thermal test. After the test, the nanowire will be cut at the line indicated by the yellow arrow (Figure 3.2 (b)) and collected for later TEM examinations to see if there is any structural change. As can be seen in Figure 3.2 (c) and (d), before EBID the amorphous layer is very thin (1-2 nm), while it becomes much thicker (~10 nm) after EBID. Since we have already used TEM images to extract dimensional

information, the diameter uncertainty is not an issue. The main problem here is the additional mass the thick amorphous layer bringing to the nanowire, which will make the measurement of resonance frequency smaller, which in turn will result in the calculated Young's modulus smaller than the actual one.

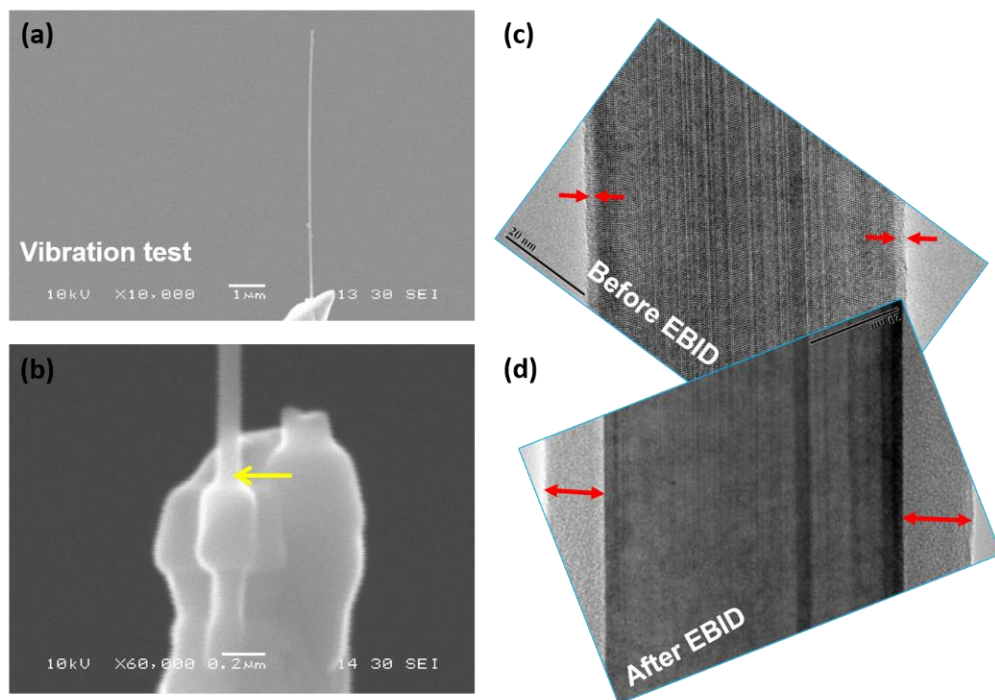


Figure 3.2: (a) and (b) EBID clamping of a nanowire on a tungsten tip for vibration test, (courtesy of Dr. Youfei Jiang) (c) and (d) TEM images of the same nanowire before and after EBID.

### 3.1.2 The Effect of Cross Section Shape

As can be seen in both Equation (2.6) and (3.1), cross sectional area is a key parameter to calculate the thermal conductivity and Young's modulus. In order to get valid data, the cross section of each nanowire needs to be characterized. However,

because of the difficulty to do that, most people tend to assume the cross section is in a circular shape and use the following equation to calculate the area:

$$A = \pi D^2 / 4 \quad (3.3)$$

In the case of boron carbide nanowires, it is found that their cross section is actually not circular. As evidenced in Figure 3.3 (a) and (b), in which the diameters from two zone axes are different. Otherwise, one would expect an equal diameter at different viewing zone axis. Moreover, it is lucky enough to view some cross sections of short branched nanowires under TEM. One example is shown in Figure 3.3 (d), which has an irregular polygon shapes with approximate eight sides (red lines) and is darker due to the strong thickness contrast. The corresponding short branch or segment is viewed by tilting the nanowire in around  $60^\circ$ . As shown in Figure 3.3 (c), an AF characteristic feature is seen and the diameter indicated by the blue line is 90 nm, which resulting in a cross sectional area of  $6358 \text{ nm}^2$  based on Equation (3.3). While the area directly measured from the polygon highlighted Figure 3.3 (d) using Image J is about  $6719 \text{ nm}^2$ , which is only slightly larger (5%) than that of the circular one. Therefore, the thermal conductivity and Young's modulus calculation based on the assumption of a circular cross section is within acceptable error range for our boron carbide nanowires. Figure 3.3 (c) and (d) present two more examples of the boron carbide nanowires' cross sections viewed under SEM, which exhibit similar irregular polygon shape as observed in TEM.

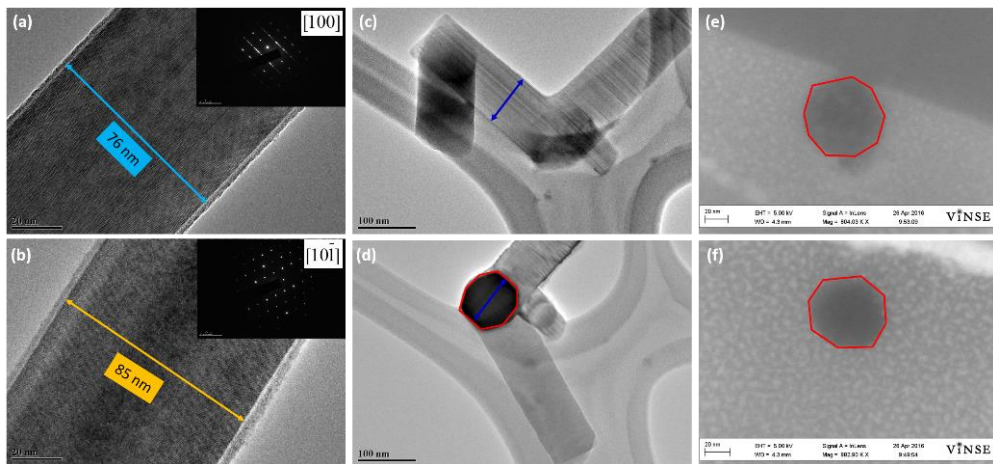


Figure 3.3: Cross section analysis of boron carbide nanowires: (a) and (b) an AF nanowire viewed from two different zone axis, (c) and (d) a short segment before and after tilting, (e) and (f) SEM images of two nanowires' cross sections cut by FIB. ((e) and (f) are courtesy of Mr. Qian Zhang).

### 3.1.3 Conclusions

In conclusion, a thorough TEM examination of each nanowire before and after thermal and mechanical properties test is necessary to establish the true structure-properties relations for individual nanowires since EBID often result in a thick amorphous layer built-up. The cross section of boron carbide nanowire is in an irregular polygon rather than a round shape with minor difference in area measurement. Therefore, our thermal conductivity and Young's modulus calculation based on a circular cross section assumption is still valid.

## 3.2 Kinking in Boron Carbide Nanowires

### 3.2.1 Introduction

Semiconductor nanowires (NWs), including group IV, group III-V ones, metal oxides ones and heterostructure ones, have attracted enormous attentions in the last two

decades due to their outstanding electrical, optical, mechanical and thermal properties comparing to their bulk counterparts.<sup>84,199-202</sup> In regards of the future nanoscale electronic device applications, straight NWs are more preferred in many aspects because of good alignment ability and well-investigated properties, also straight NWs based field emission transistors (FETs),<sup>203</sup> lasers,<sup>204</sup> photo detectors,<sup>205</sup> sensors<sup>206</sup> and solar cells<sup>207</sup> have already been demonstrated in many groups. Therefore, one aim of the controllable synthesis of semiconductor NWs via vapor liquid solid (VLS) is to avoid undesirable kink structures.<sup>208,209</sup>

However, recent reports have shown these traditionally unfavorable kinked NWs tend to exhibit similar electrical properties as compared to the straight ones,<sup>210</sup> reduced thermal conductivity<sup>94,95</sup> and nanospring mechanical behaviors<sup>211</sup>. It is believed that the kink imposes favorable effect on the transport and mechanical properties. It is proposed that kinked NWs could also be the building blocks for next generation nanoelectronic devices with improved performance.<sup>158,212,213</sup> For example, owing to their special geometry, kinked Si nanowires based bioprobes are capable of monitoring inter- and intracellular processes with enhanced penetration depth and spatial resolution.<sup>159</sup> Clearly, it is of significant importance to understand how and why kinking occurs during the NWs growth (*e.g.* the change of growth orientation and evolution of microstructures) so as to be able to control the growth of kinked NWs for future devices with unique capabilities.

The  $\langle 111 \rangle$  to  $\langle 111 \rangle$ ,  $\langle 111 \rangle$  to  $\langle 112 \rangle$  and  $\langle 112 \rangle$  to  $\langle 112 \rangle$  growth orientation transitions are commonly observed in kinked Si NWs.<sup>136,161,214</sup> In addition, a very recent

publication reported a kinked Si NW with rare  $\langle 111 \rangle$  to  $\langle 311 \rangle$  transition.<sup>215</sup> Even though Ge shares the same diamond cubic structure as Si, kinked Ge NWs grown via VLS frequently exhibit  $\langle 111 \rangle$  to  $\langle 110 \rangle$  kinks without any defects.<sup>139</sup> Group III-V NWs (GaAs, InAs, InP, etc.) usually have a cubic zinc-blend (ZB) or hexagonal wurtzite (WZ) crystal structure and tend to have high density of planar defects on the (111) planes with a  $\langle 111 \rangle$  growth orientation.<sup>216</sup> With the possibility of growing along  $\langle 100 \rangle$  and  $\langle 110 \rangle$  direction,  $\langle 111 \rangle$  to  $\langle 111 \rangle$ ,  $\langle 111 \rangle$  to  $\langle 110 \rangle$  and  $\langle 111 \rangle$  to  $\langle 100 \rangle$  kinks usually exist in kinked group III-V NWs.<sup>141,217</sup> For instance, both  $\langle 111 \rangle$  to  $\langle 110 \rangle$  and  $\langle 111 \rangle$  to  $\langle 100 \rangle$  kinks have been demonstrated for InP NWs.<sup>141</sup> Experimentally observed kinking in VLS grown semiconductor NWs often occurs when temperature or pressure changes in the reaction chamber.<sup>135,218</sup> In addition, the surface chemistry (hydrogen bond) is also reported to be able to control the kink structure's formation.<sup>139,219</sup> By modulating the parameters such as temperature and pressure or surface chemistry, the number of the kinks and even the growth orientation could be controlled. It is believed that the liquid droplet's dynamic motions (pinning and unpinning), shape and geometry evolution caused by liquid-solid interface's instability may lead the formation of kinks in VLS grown nanowires.<sup>220</sup> However, planar defects, such as twin boundaries (TBs) and stacking faults (SFs), may also influence the change in original growth orientation, though not all kinked NWs have such defects.<sup>137</sup>

So far, most of the VLS grown kinked semiconductor NWs being studied, as mentioned above but not limited to, exhibit simple cubic, diamond cubic, cubic ZB or hexagonal WZ crystal structures. It would be beneficial if the similar structural and

growth studies could be extended to some NWs with more complicated crystal structures. Boron carbide (B<sub>4</sub>C) nanowires, which has a rhombohedral crystal structure ( $R\bar{3}m$ , No. 166) with eight B<sub>12</sub> icosahedron and a C-B-C chain located at the vertex and longest diagonal respectively,<sup>28</sup> offer such an opportunity. Straight B<sub>4</sub>C nanowires have been synthesized and characterized by several groups including our group.<sup>103,114,115,122</sup> However, to the best of our knowledges, research on the detailed microstructures of kinked B<sub>4</sub>C nanowires, which are keys to establish true structure-properties relationship, are extremely rare.

In this chapter, a thorough discussion on investigating the structures and growth mechanisms of kinked B<sub>4</sub>C NWs using SEM and TEM is presented. In our previous studies,<sup>103</sup> two types of planar defects, transverse stacking faults (TF) in which growth direction is perpendicular to the defect planes and axial stacking faults (AF) in which growth direction is parallel with the defect planes, exist in our as synthesized B<sub>4</sub>C NWs. In current study, a third type of planar defects, inclined stacking faults (IF) in which growth direction is neither perpendicular to nor parallel with the defect planes, was identified. Based on the planar defects on two arms of the kink, the observed kinked B<sub>4</sub>C NWs could be categorized into five cases: TF-TF (case 1), AF-TF (case 2), AF-AF (case 3), TF-IF (case 4), AF-IF (case 5) kinked NWs. The characteristic kink angle of each case was determined by calculating the inter-growth direction angle. Besides, kinked B<sub>4</sub>C NWs with multiple kinks were also found, but it could be broken down to the above mentioned five cases. Furthermore, by looking into the catalyst's movement,

position, shape and interface, the possible growth mechanisms were proposed to explain the formation of kinked B<sub>4</sub>C NWs.

### 3.2.2 Experiments

The kinked B<sub>4</sub>C NWs investigated in this work were grown by co-pyrolysis of diborane and methane in a home-built low-pressure chemical vapor deposition system following the VLS mechanism at temperature between 950 and 1050 °C. Nickel (Ni) was used as catalyst material and coated onto Si/SiO<sub>2</sub> or sapphire substrates. Detailed synthesis procedure was described elsewhere.<sup>103</sup> The general morphologies of as-synthesized B<sub>4</sub>C NWs were first examined by JEOL JSM-6480 SEM. Individual kinked B<sub>4</sub>C NW was transferred to each labeled mesh of a TEM grid with lacey carbon supporting film using a micromanipulator under the optical microscope for TEM characterization. Each NW was tilted in a full range during TEM investigation, which is limited by the configuration of the microscope and holder. Some NWs were re-examined to observe the planar defects by re-orientating and repositioning individual NWs onto another region of lacey carbon film.

A JEOL JEM-2100 LaB<sub>6</sub> TEM operated at 200 kV acceleration voltage was used to record bright-field (BF) images, dark field (DF) images, high resolution TEM (HRTEM) images and selected-area diffraction patterns (SADPs) of kinked B<sub>4</sub>C NWs. A JEOL double-tilt holder was used for large angle tilting ( $\pm 30^\circ$  in both X and Y directions). The maximum tilting angle is  $60^\circ$ . Software packages such as SolidWorks and CrystalMaker were used to construct the kinked B<sub>4</sub>C nanowires models and planar defects.

### 3.2.3 General Morphology

Figure 3.4 (a) presents the top view SEM image of the as-synthesized B<sub>4</sub>C NWs on a substrate. Both straight and kinked B<sub>4</sub>C NWs were observed while kinked ones are minorities, as marked by the yellow arrows. The side view SEM image of the substrate (Figure 3.4 (b)) has clearly shown the existence of kinked B<sub>4</sub>C NWs with single kink or multiple kinks. Figure 3.4 (c) shows one example of kinked B<sub>4</sub>C NWs viewed under TEM. From this low magnification TEM image, the kink angle could be determined as 90°. Figure 3.4 (d) – (f) presents the represent HRTEM images viewed along the [010] zone axis of above mentioned three types of planar defects (SFs and TBs): TF (d), AF (e) and IF (f). The white arrow indicates the growth direction ( $[\overline{0.292} \overline{0.292} 1]$ , [100] and [110]) and the inset is the SADPs, which shows characteristic streaks features. The schematic illustration on the geometry relationship between the growth direction and defect planes or TBs is also shown in Figure 3.4 (g)-(i). It is worth noting that AF and TF B<sub>4</sub>C nanowires are more common than IF ones. Now if we zoom into the kink site shown in Figure 3.4 (c), what we see is actually a combination of AF segment and TF segment. Based on these three types of planar defects and their combinations, the kinked B<sub>4</sub>C NWs can be categorized into five cases: TF-TF, AF-TF, AF-AF, TF-IF, and AF-IF kinked NWs.

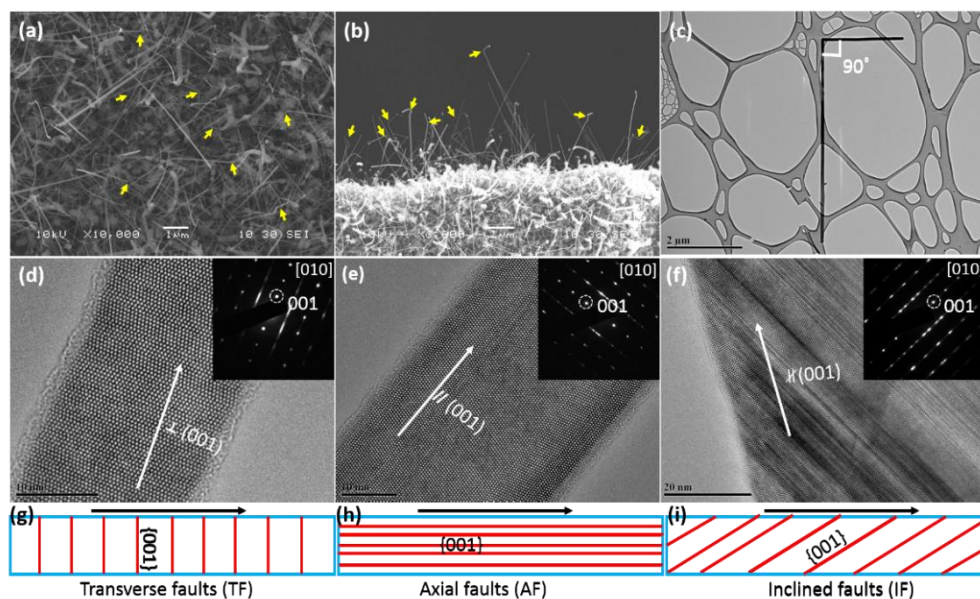


Figure 3.4: Top view (a) and side view (b) of as-synthesized B<sub>4</sub>C nanowires with yellow arrows indicating kinked ones; (courtesy of Dr. Zhe Guan) (c) Low magnification TEM image of a 90° kinked B<sub>4</sub>C nanowire; (d-f) three types of stacking faults observed in as-synthesized B<sub>4</sub>C nanowires with schematic illustration: transverse faults (TF), axial faults (AF), inclined faults (IF), (g-h) the schematic drawing of orientation of the planar defects.

### 3.2.4 Case 1: TF-TF Kinked NWs

Planar defects could be clearly seen in most TF-TF kinked NWs' two arms or segments during TEM examination when tilting the nanowire to certain zone axis, as shown in Figure 3.5 (a) and (c). It is clearly seen before and after the growth direction transition, both SFs and TBs keep perpendicular to the growth direction, which is exactly a TF type. The measured kink angles are 106° and 107° for the two examples respectively, which both match extremely well with the theoretical value of 106.9°. Figure 3.5 (b) and (d) are the zoom in HRTEM images of dashed line highlighted kink area in Figure 3.5 (a) and Figure 3.5 (c) respectively. The former one shows a defect-free transition area, while the latter one composed two SFs: SF1 and SF2 (indicated by

the red line) formed at the (100) and (001) planes respectively as well as some deformations within the transition area. This subtle structure difference may affect the final transport properties within the TF-TF kinked NWs. However, by simply looking at the low magnification TEM images shown in the left inset in Figure 3.5 (a) and (c), it is impossible to distinguish the structure difference between these two NWs, which in turn imposes difficulty to correlate the structure and transport properties. Besides  $106.9^\circ$  kink angle in TF-TF kinked NWs, its supplementary angle  $73.1^\circ$  should also be possible. Indeed, this is experimentally verified by observing several TF-TF kinked NWs with such an acute kink angle. One example was shown in Figure 3.5 (e), in which a  $73^\circ$  kink angle was determined according to the TEM image. The black spot is a catalyst nanoparticle attached onto the kinked NW. The transition area has a diamond shape and high density of SFs at one segment. Kinked  $B_4C$  NWs with acute angles are only observed in TF-TF kinked ones, which could be used as a reference to quickly identify the kinked  $B_4C$  NWs' cases. However, it should be noted that only very few (less than five) TF-TF kinked NWs have been observed so far.

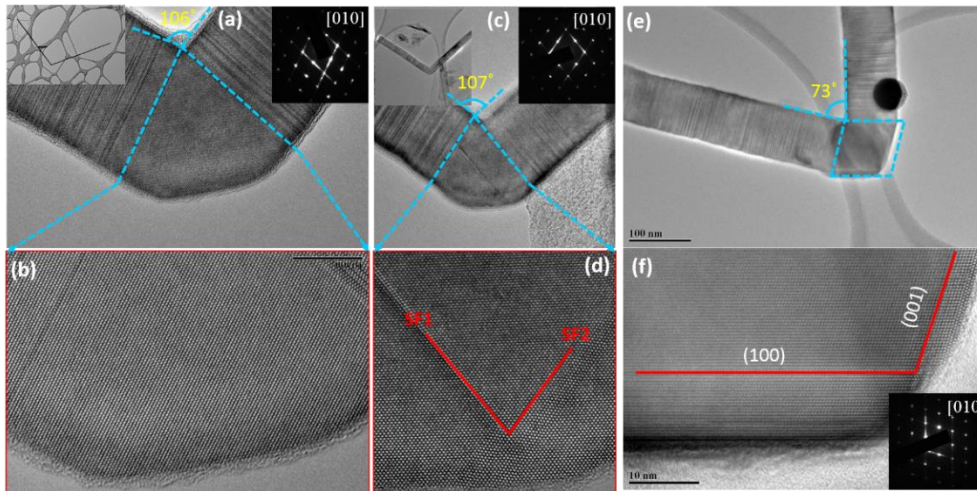


Figure 3.5: (a) and (b) TF-TF kinked NWs with obtuse  $106.9^\circ$  kink angle. The insets are low magnification TEM image showing whole NW and the corresponding SADPs. (c) and (d) are the zoom in HRTEM images of the kink area in (a) and (b). (e) TF-TF kinked NW with acute  $73^\circ$  kink angle and HRTEM image (f) of the kink area showing stacking faults formed on (100) and (001) plane.

If the above-mentioned  $106.9^\circ$  or  $73.1^\circ$  TF-TF kink could be repeated in one  $B_4C$  NW, a coherent crystallographic structure TF-TF kinked  $B_4C$  NW with multiple kinks would be produced. However, our kinked  $B_4C$  NWs with multiple kinks are not similar to those Si kinking superstructures having the same kink angle and crystallographic orientation.<sup>161,219</sup> Figure 3.6 presents a kinked  $B_4C$  NWs with two kinks. As seen in Figure 3.6 (b), kink 1 with  $105.8^\circ$  kink angle is identical to the common  $106.9^\circ$  TF-TF kink and the transition area at kink 1 exhibits two intersected SFs lines or planes. Small deformation occurs at the intersection point. However, kink 2 demonstrates different features as compared to kink 1. Firstly, the measured kink angle from the TEM image (Figure 3.6 (c)) is  $122^\circ$ . Secondly, planar defects were observed in one segment (above the kink) of the NW, while not in the other (below the kink). The viewing direction is [010], as determined from the inset SADPs. But based

on our experience, the observation of the “ring” features and the geometry relation between the growth direction and SADPs infers that the segment below the kink belongs to TF. Moreover, this NW was tilted around  $57^\circ$  to the other zone axis  $[\bar{1}10]$ . Figure 3.6 (d) and (e) present the TEM images of the entire NW and the kink site respectively. The planar defects were still not visible in the segment below the kink. It speculated that the two segments at kink 2 are not in the same plane, as shown in Figure 3.6 (f). The defect planes of kink 2 is more like to be (010) instead of (001). This observation also demonstrates the wide range of catalyst’s movement or migration.

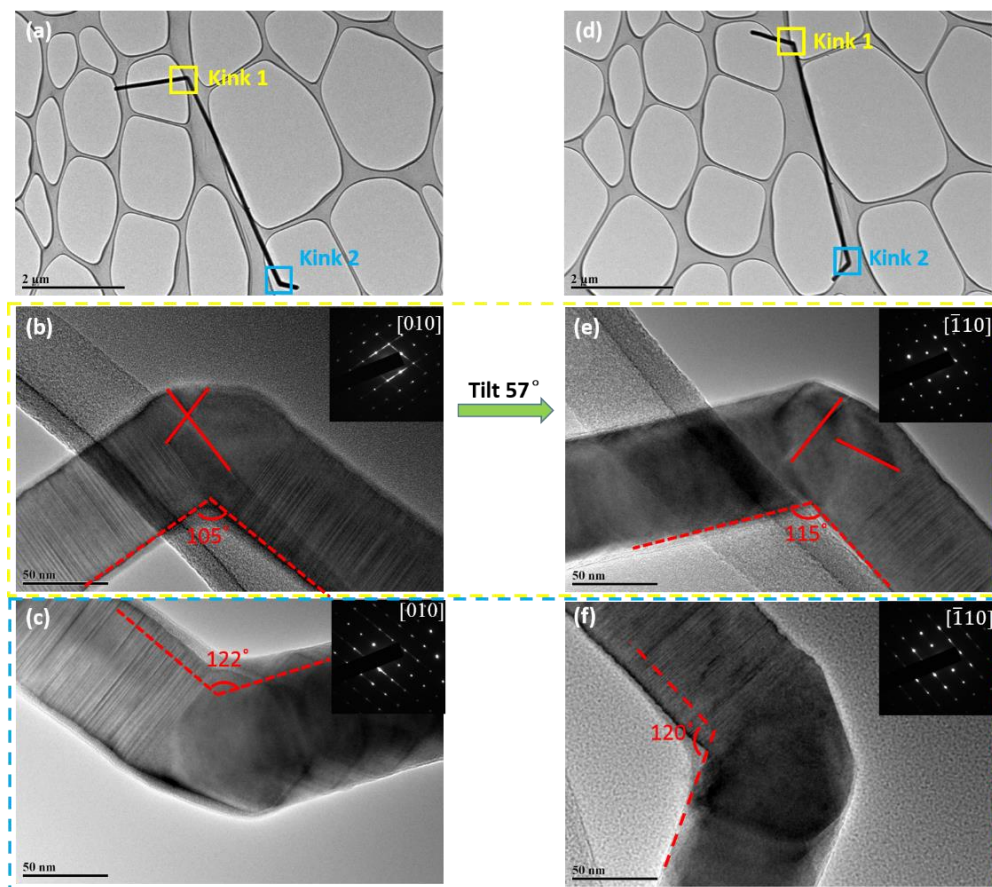


Figure 3.6: A TF-TF NW with two kinks viewed from tow direction:  $[010]$  and  $[\bar{1}10]$  whole NW (a,d), kink 1 (b,e) and kink 2 (c,f)

Even though kinks in TF-TF kinked NWs could exist in different planes, it was found that the basic nature (transition) of all types of kinks is identical under modeling. Because of the tilting limitation to (maximum  $60^\circ$ ), the kinks can not be viewed in every zone axis. It should be noted that the recorded TEM images are the projections of the samples being examined, which poses difficulty to model the kinked nanowires solely based on the data from one zone-axis. Here our basic model was built in the SolidWorks based upon the TEM images obtained from  $[010]$  zone axis, viewing from which both sides of the kink are in-zone and atomic arrangement or stacking is evident. Based on the crystallography structure of a rhombohedron, Figure 3.7 (a) shows a general view of the model with a “saw tooth” edge at the transition area, but it is physically imaged as a smooth edge surface due to limited resolution. This simple model could be rotated and viewed in any direction in order to compare with the experimental data. As shown in Figure 3.7 (b)-(e), the general morphology and kink angle match very well between the model and actual nanowire viewed from  $[1\bar{1}0]$ ,  $[100]$ ,  $[010]$ , and  $[\bar{1}10]$  zone axes, which further validates the accuracy of our model. Particularly, from Figure 3.7 (b) to Figure 3.7 (c), the nanowire needs to be tilted  $114.2^\circ$ , far beyond the limit of our TEM holder, which explains why a full set of data from one kink is rarely seen experimentally. This also emphasizes the advantages of building the models, which facilitate the identification kinked NWs’ types even from the images in off-zone axis.

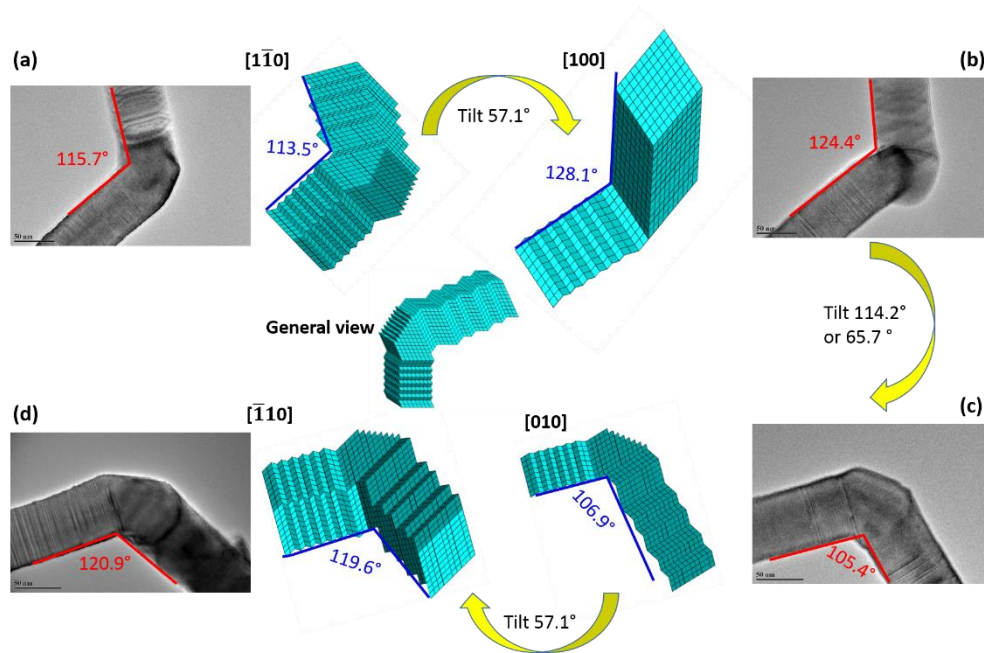


Figure 3.7: The comparison between the model and experimental kinked angles viewed from different zone axis: (a)  $[1\bar{1}0]$ , (b)  $[100]$ , (c)  $[010]$  and (d)  $[\bar{1}10]$ .

### 3.2.5 Case 2: AF-TF Kinked NWs

Another commonly observed kinked  $B_4C$  nanowires exhibit a combination of an AF segment and a TF segment, which usually results in a  $90^\circ$  turning angle, as shown in Figure 3.4. In this kind of kinked nanowires, the stacking faults plane in both AF and TF arms is the same (001). In addition, AF arm's growth direction  $[010]$  is parallel with (001) plane, while TF arm's one  $[\bar{0.292}\bar{0.292}1]$  is perpendicular to (001) plane. Therefore it is easy to derive the kink angle to be  $90^\circ$ . However, even the general kink angle is the same, the structural details varies a lot in between nanowires.

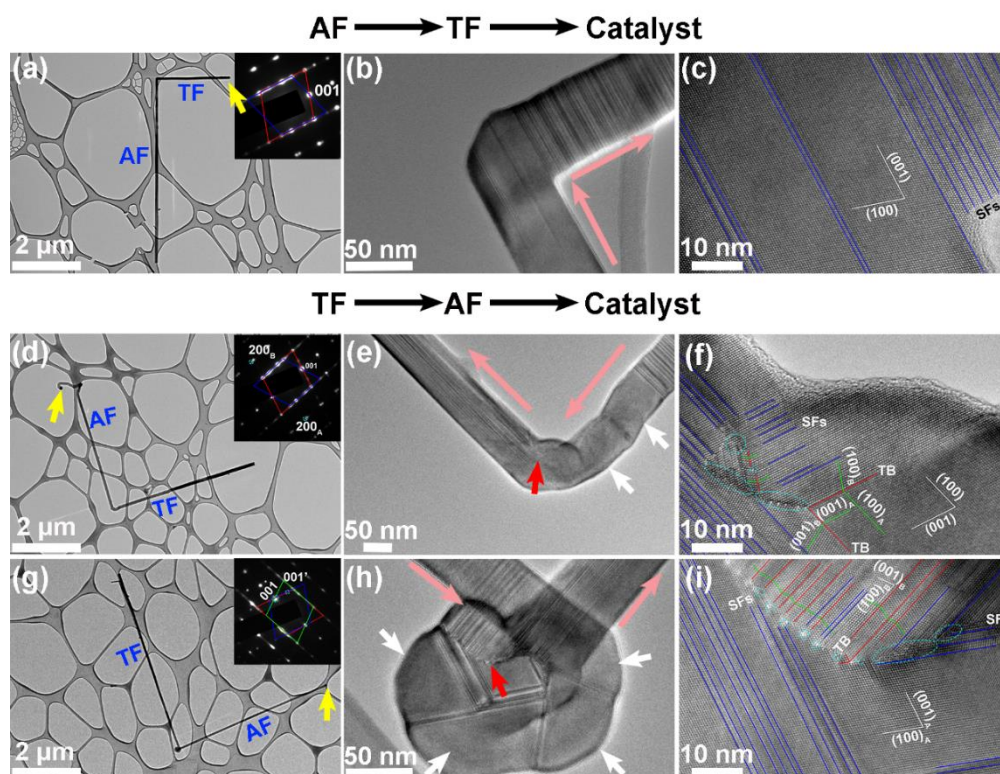


Figure 3.8: Low and high magnification TEM images of Two types of AF-TF kinked NWs based on the location of the catalyst: (a-c) AF-TF-catalyst, (d-i) TF-AF-catalyst.

Based on the location of the catalyst, AF-TF kinked could be further categorized to two groups, one, AF-TF-catalyst, in which AF arm usually grows first, then the TF arm continues and finally the catalyst sits on top of the TF arms, the other, TF-AF-catalyst, in which the growth sequence reverses. One representative example of AF-TF-catalyst kinked nanowires was shown in Figure 3.8 (a), in which the fault types of the two arms are labeled and the yellow arrow indicates the location of the catalyst. By zooming in to the kinked area, a smooth and direct transition from an AF segment to a TF segment was evidenced in Figure 3.8 (b) (the growth direction indicated by the peach arrows). One interesting finding is that the fault density of the AF arm is relatively low, in other words the number of stacking fault planes are small, as

confirmed from the DPs (inset in Figure 3.8 (a)) and HRTEM image (Figure 3.8 (c)) collected in the kinked area. In high fault density area, a streak is commonly seen in the DPs, while in low fault density area, instead of a streak, distinctive diffraction spots appear along the stacking faults' direction, which is the case in the inset in Figure 3.8 (a). Two sets of rhombus (red and blue) were resolved in the DPs, which indicate the existence of microtwins. In Figure 3.8 (c), the AF and TF planar defects are more clearly seen and are marked by blue lines. By looking more closely, the angle between the AF segment and the first few defect-free layers of TF segment is found to be  $107^\circ$ . If there are no defects forming after transition, one could expect a defect-free segment connecting to the AF segment with an angle either  $106.9^\circ$  or  $73.1^\circ$ . However, defect-free B<sub>4</sub>C NWs have not been found in our as-examined hundreds of NWs, which means that the AF-defect free kinks probably would not exist.

Figure 3.8 (d) and (g) shows two examples of TF-AF-catalyst kinked nanowires. As indicated by the yellow arrows, the catalysts locate on top of the AF ends in both. In addition, different from the AF-TF-catalyst ones, these two nanowires' AF arms have much higher fault density. Actually it is reasonable since TF arms usually have high fault density. And when the catalyst migrates to the TF arm's sidewall and leads the further growth layer by layer, the later arm tends to share the similar fault density as the TF seeds. However, the true mechanism governing this kind of catalyst's migration and subsequent growth is complicated. As seen in Figure 3.8 (e) and (h), a number of large twin blocks (marked by white arrows) formed before the growth of the AF arms. Moreover, in the kinked area, additional defects (new stacking faults, twins,

dislocations) pointed by red arrows were also observed. From the HRTEM image shown in Figure 3.8 (f) and (i), the stacking faults including in the original and new planes (blue lines), twin boundaries (green lines), dislocations (dashed circle) were carefully identified. At the boundary, where several SFs lines meet, the lattices deformation and mismatch are serious, which is believed to cause the dislocations. The corresponding DPs from the kinked area shown in Figure 3.8 (f) and (i) are inserted in Figure 3.8 (d) and (g) respectively. In the DPs shown in Figure 3.8 (d) inset, three rhombuses were highlighted. The red and blue are two mirrored ones, while the green one is induced by the new inclined stacking faults planes. The inter-plane angle between the original stacking faults plane (001) and inclined one (001') is  $163^\circ$ , which matches with the theoretical calculation. One more thing worth noting is that the kinked area in Figure 3.8 (g) nanowire is like a knot and the two arms are not in the same plane, which is confirmed by tilting the nanowire to another zone axis  $[\bar{1}10]$ . From the DPs collected at the knot (Figure 3.8 (g) inset), additional diffraction spots from different blocks showed up with some rotation compared to the original ones.

A simple model describing the common AF-TF kinked  $B_4C$  NWs' transition area was built using SolidWorks. The model was simplified to show only the stacking faults orientation change and  $90^\circ$  angle. Figure 3.9 shows an AF-TF kinked NW tilted to two different zone axes [010] and  $[\bar{1}10]$  under the TEM. Again, the experimental measured kink angles are in good agreement with the ones obtained from the model viewed from exactly the same zone axis in SolidWorks.

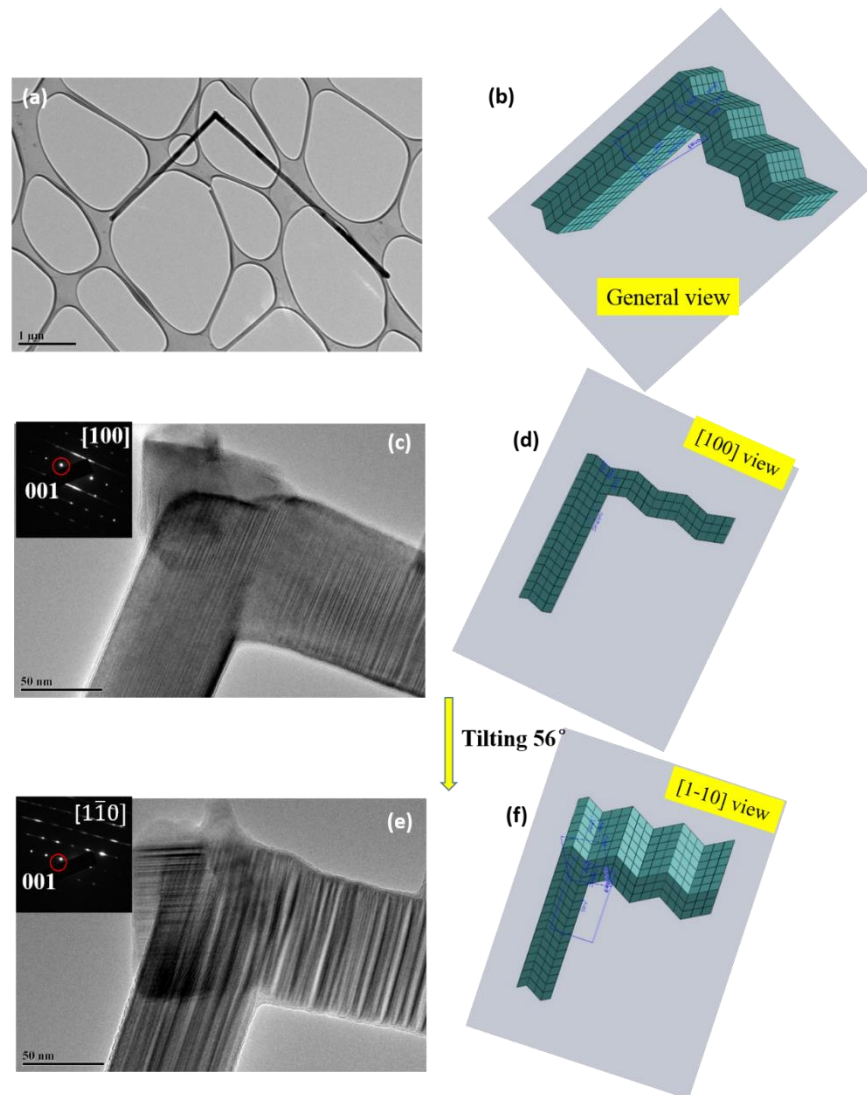


Figure 3.9: (a) Low magnification TEM image of an AF-TF NW (b) General view of AF-TF model built using SolidWorks (c) HRTEM image of AF-TF NW viewed from  $[100]$  zone axis and (d) the model viewed in the same zone axis in SolidWorks; (e) same NW tilted to  $[1\bar{1}0]$  zone axis and corresponding model in same zone axis (f).

### 3.2.6 Case 3: AF-AF Kinked NWs

Figure 3.10 (a) shows a  $B_4C$  NW, which looks almost straight without carefully examining the TEM image. By zooming in to the red square area marked in Figure 3.10 (a), a “step” shows up in the HRTEM images (Figure 3.10 (b)) though the overall growth direction stays unchanged. The kink angle was determined as  $180^\circ$ . However, it

is clear that before and after the “step” the NW shares the same AF planar defects with different stacking sequence or polymorphs. Another example of AF-AF kinked NWs is shown in Figure 3.10 (c). From the low magnification TEM image, two kinks actually could be observed. Here our focus is the top one since the bottom one is a common TF-TF kink. Figure 3.10 (d) is the zoom in TEM image of the top kink with a  $135.1^\circ$  angle, in which a short zigzag side is shown and planar defects are not seen above and below the kink area. From the inset SADPs, the zone axis was determined to be  $[01\bar{1}]$ . In order to better understand the structure of this special kink, the NW was tilted to the limitation of the microscope and holder. The TEM image with corresponding SADPs is presented in Figure 3.10 (e). The current zone axis is very close to  $[010]$ , viewing from which the planar defects could be seen below and above the kink. Though no HRTEM images, the SFs and TBs parallel to the growth direction indicate the two segments are of AF planar defects. In addition, one side’s zigzag features observed from the other zone axis were not seen. By closely examining at the transition from top to bottom at the kink, the above AF segment first gradually change the stacking fault density but retains the same growth direction. Then the transition from this point to the bottom AF segment manifests the development of several short defects free segments as evidenced from the dark band in Figure 3.10 (d). The kink angle viewing from this direction is  $145.6^\circ$ .

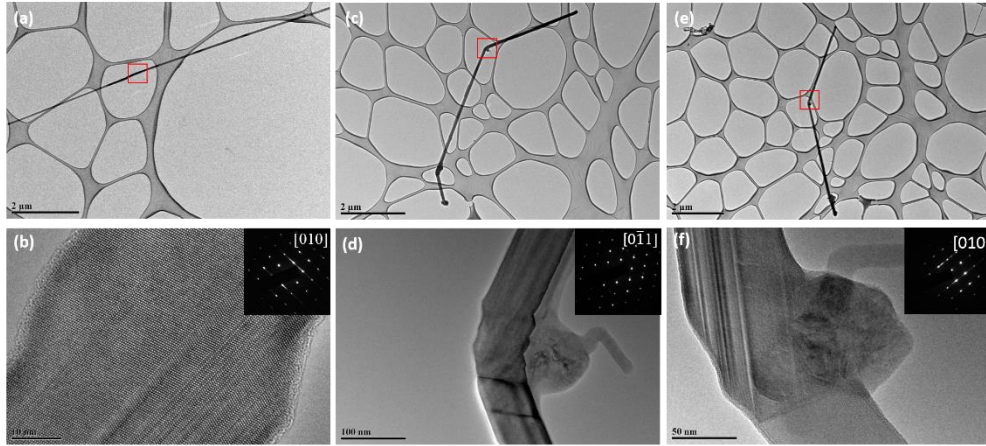


Figure 3.10: (a) and (b) AF-AF kinked NWs with a “step”; (c-f) an AF-AF NW viewed from two zone axes

Another interesting finding on the structural study of the AF-AF kinked  $B_4C$  NWs is for one type of kinked nanowires with large obtuse angle ( $166^\circ$  or  $158^\circ$ ), the kink could only be seen in off-zone conditions, where the planar defects could not be seen, while not in in-zone conditions, where the planar defects become visible, as shown in Figure 3.11. As introduced in section 1.6, the defect planes of our boron carbide nanowires are usually defined as (001) planes with the three off-zone conditions being  $[001]$ ,  $[10\bar{1}]$  and  $[01\bar{1}]$ , while three in-zone conditions are  $[100]$ ,  $[010]$  and  $[1\bar{1}0]$ . Figure 3.11 (a) and (c) represents the same nanowire viewed from zone axis  $[0\bar{1}1]$  (off-zone) and  $[0\bar{1}0]$  (in-zone) respectively. The insets in Figure 3.11 (a) and (c) are corresponding DPs and the one in Figure 3.11 (c) has streak features, which indicates defect planes were seen as well. By enlarging the kink area viewed from off-zone (Figure 3.11 (c)) and in-zone (Figure 3.11 (d)) axes, it can be clearly seen that the kink in off-zone disappeared when tilting the nanowire to in-zone. This kind of kink

is ascribed to extrinsic nature of B<sub>4</sub>C NWs, which is most likely due to external force induced curving or bending.

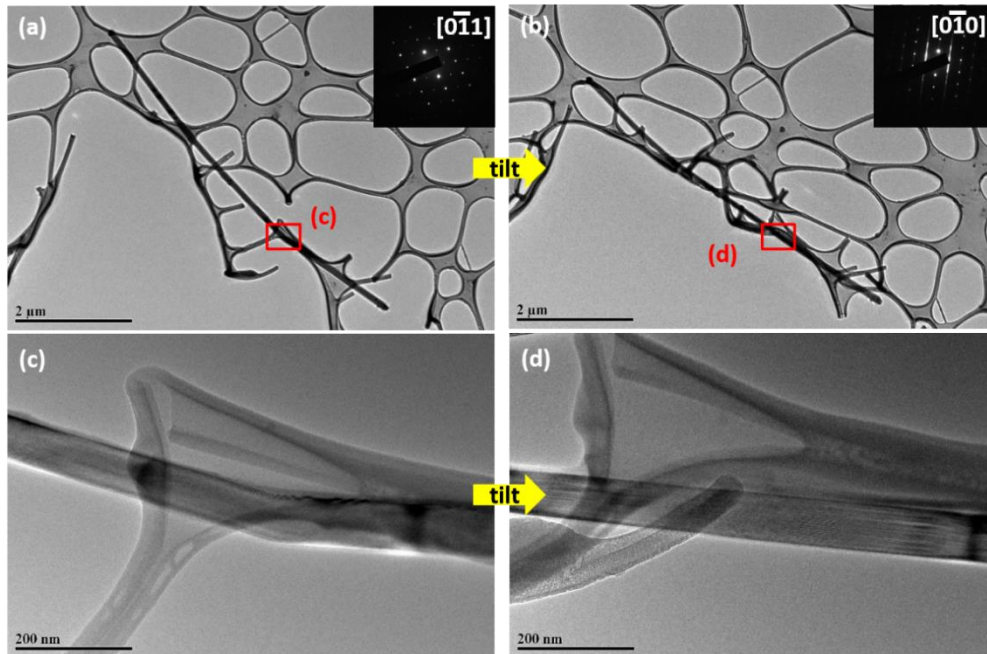


Figure 3.11: An AF nanowire viewed from two different zone axes: kink can be seen in  $[0\bar{1}1]$  zone axis (a) and (c) but not  $[0\bar{1}0]$  zone axis (b) and (d).

Moreover, Figure 3.12 shows another three examples of above-mentioned AF-AF kinked nanowires, which do not match our AF case model thoroughly along the nanowire. More specifically, the segment at one end of the kink successfully matches the model, while the segment at the other end does not. The AF case model is summarized in Table 1.1, which was proposed to determine the stacking fault orientation within a nanowire when the nanowire is in off-zone conditions. The first row of Figure 3.12 presents an AF nanowire viewed from  $[01\bar{1}]$  zone axis. From the low magnification image of the nanowire, Figure 3.12 (a), a clear kink was observed. The high magnification images and corresponding DPs were collected at both sides of

the kink and were shown in Figure 3.12 (b) (position 1) and (c) (position 2). From Figure 3.12 (b), an AF case 3 could be concluded according to the model, in which the projected preferred growth direction (red line extracted from the inset image) is perpendicular to the tie line between  $011$  and  $0\bar{1}\bar{1}$  spots (blue line). However, as shown in Figure 3.12 (c), the projected preferred growth direction (green line) is not perpendicular to the tie line between  $011$  and  $0\bar{1}\bar{1}$  spots (yellow line), which means it does not agree with our AF case model. More interestingly, by using the projected preferred growth direction at position 1 and the DPs taken at position 2, an AF case 3 could be obtained (the red line is perpendicular to the yellow line in Figure 3.12 (c)).

Figure 3.12 (d-j) shows two additional nanowires viewing from the other two off-zone axes  $[\bar{1}01]$  and  $[00\bar{1}]$  respectively with similar findings, namely one end of the kink matches our model (AF case 2 at  $[\bar{1}01]$  and AF case 1 at  $[00\bar{1}]$ ), but not for the other end. The reason is that the DPs taken at position 1 and 2 are identical, but the projected preferred growth directions vary. Therefore, if one position agrees with our model, the other part definitely will not. The question now is why there is no difference or little difference between the DPs taken at two different positions? Theoretically, the DPs taken at different ends of the kink should be different. Here the hypothesis is that curving and bending will not affect the periodic arrangement nature of the unit cells and one arm gives a false growth direction.

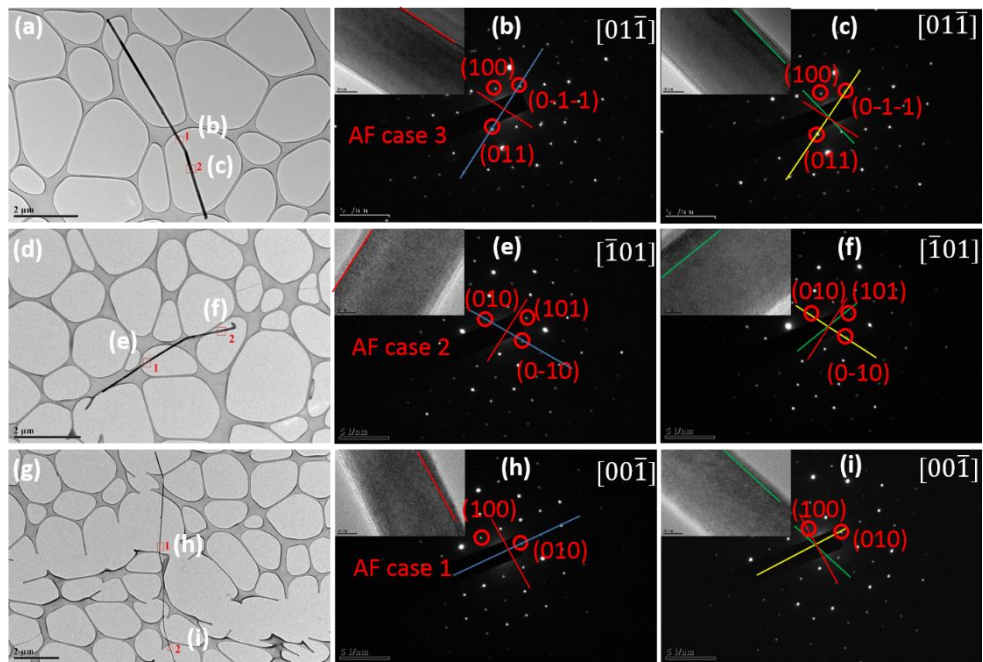


Figure 3.12: Three kinked AF nanowires viewed from  $[01\bar{1}]$  (a, b, c),  $[\bar{1}01]$  (d, e, f) and  $[00\bar{1}]$  (g, h, i) zone axis respectively with one end of the kink matches our AF case model but not the other end.

Recently, a third type of AF-AF kinked NWs was discovered. Similar to the one shown in Figure 3.11, kinks are only seen from off-zone axes while not from in-zone axes. The major difference is the kink angles. Current ones exhibit smaller kink angles:  $107^\circ$  for  $[001]$  and  $120^\circ$  for  $[0\bar{1}1]$ , as can be seen in Figure 3.13 (a) and (b) respectively. In addition, two kinks are often seen in one nanowire with a short segment in the middle connecting the other two long arms. By viewing from the in-zone axis  $[010]$ , only the segment's cross section other than the body could be seen, the dark part shown in Figure 3.13 (d). If looking more closely, when one long arm is in-focus, the other one is always not, which clearly indicates that the two arms are not in the same plane and are separated by a short segment.

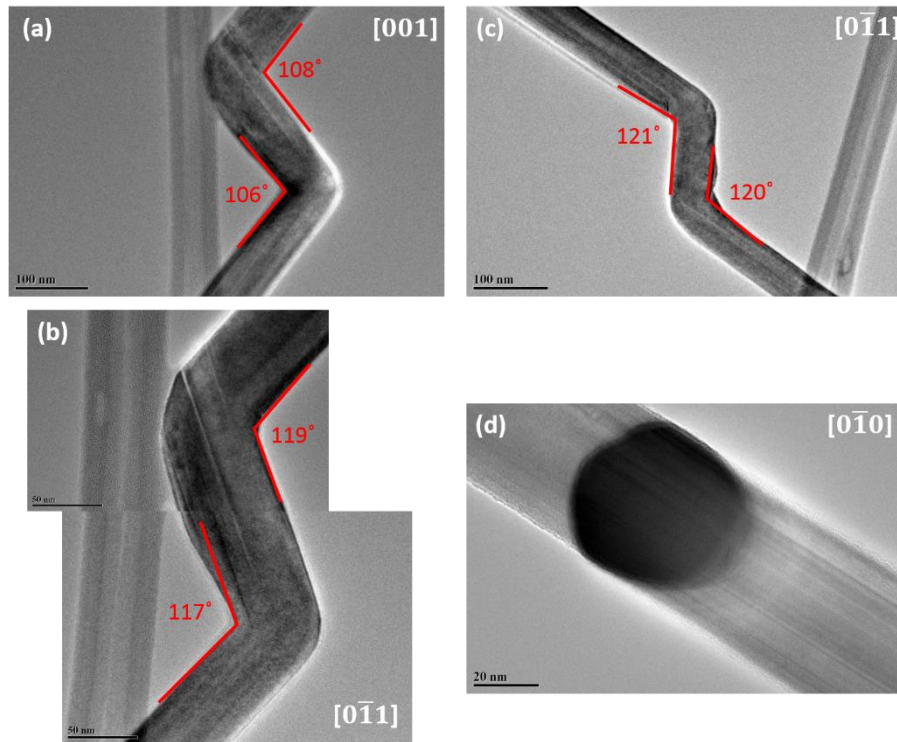


Figure 3.13: (a) and (b) A same kink viewed from  $[001]$  and  $[0\bar{1}1]$  zone axis respectively; (c) and (d) another kink viewed from  $[0\bar{1}1]$  and  $[0\bar{1}0]$  zone axis respectively.

Again a simple model corresponding to the abovementioned observation was built to describe the transition at the kink area. Figure 3.14 (a) shows the general view of this model, in which a short segment (“step”) is included in between two arms. Viewing from the in-zone axes,  $[100]$  (Figure 3.14 (b)) and  $[1\bar{1}0]$  (Figure 3.14 (c)), the model looks exactly straight, while kinks only appear in the off-zone conditions,  $[001]$  (Figure 3.14 (d)),  $[0\bar{1}1]$  (Figure 3.14 (e)) and  $[10\bar{1}]$  (Figure 3.14 (f)). Moreover, the shapes and the kink angles measured from the model are in good agreement with the experimental ones, which confirms the current model is relevant and useful to describe this kind of AF-AF kinked NWs with insightful structural information.

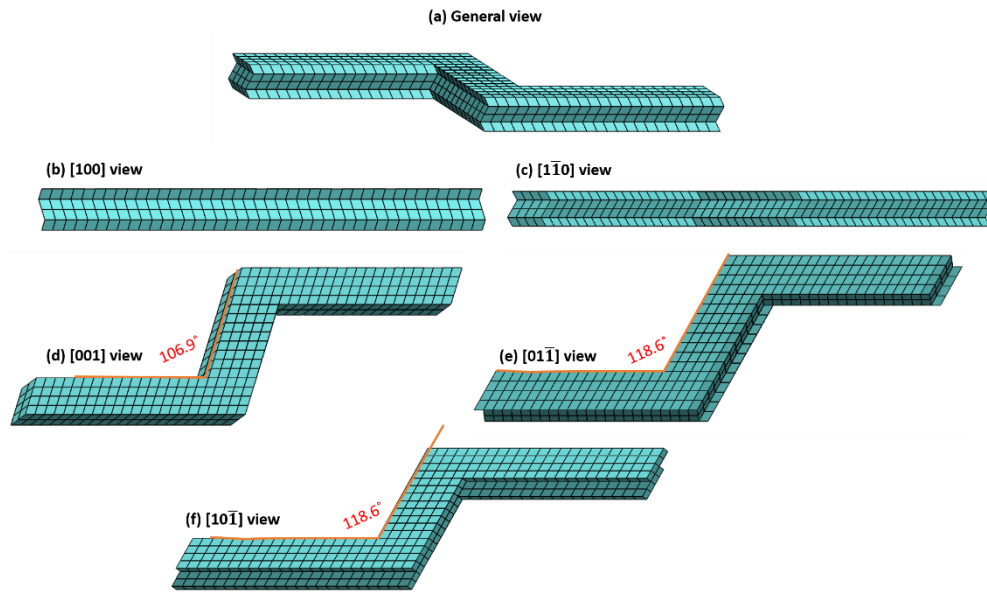


Figure 3.14: The AF-AF kinked NW model viewed from different zone axis in SolidWorks: (a) general view, (b)  $[100]$  view, (c)  $[1\bar{1}0]$  view, (d)  $[001]$  view, (e)  $[0\bar{1}1]$  view and (f)  $[10\bar{1}]$ .

### 3.2.7 Case 4: TF-IF Kinked NWs

Inset DF TEM image in Figure 3.15 (a) presents a TF-IF kinked  $B_4C$  NW. It is clearly seen that planar defects at the top segment belong to TF, while the bottom one belongs to IF. The IFs planes stacks in a direction which forms an angle of  $163^\circ$  with the TF planes. The measured kink angle is  $160.8^\circ$ , which is extremely close to the theoretical value of  $160.5^\circ$ . At the transition area from TF to IF (Figure 3.15 (a)), a clear TB at (001) plane was formed. A simple twin model of two  $B_4C$  unit cells was built and inserted for better illustration. The inset SADPs were taken from  $[010]$  zone axis at the respective positions marked with the white dashed square areas. It is worth noting that the inclined stacking faults were initiated at left corner of the TB, where this might be the liquid-solid-vapor triple phase line as the catalyst moves and wets the side

surfaces.<sup>221</sup> Ideally the kinking occurs when the catalyst completely wets the newly formed inclined facet. In our case, the growth direction is not perpendicular to the inclined facet, which means the catalyst might sit on the inclined facets of both sides and induce the current grown direction shown in Figure 3.15 (a).

### 3.2.8 Case 5: AF-IF Kinked NWs

Figure 3.15 (b) presents an example of AF-IF kinked B<sub>4</sub>C NWs. The inset DF TEM image clearly shows the IF part, where the IF planes stack in two directions marked by the red arrows. A simple model (bottom right inset) consisting of five B<sub>4</sub>C unit cells was built to explain the two stacking directions. While the AF part is evidenced by the two TBs marked. The transition area looks as if being twisted from AF segment into the IF segment. For this NW, it is difficult to tell where the inclined faults first initiated. The kink angle being measured is 108.0°, which matches well with theoretical one 110°.

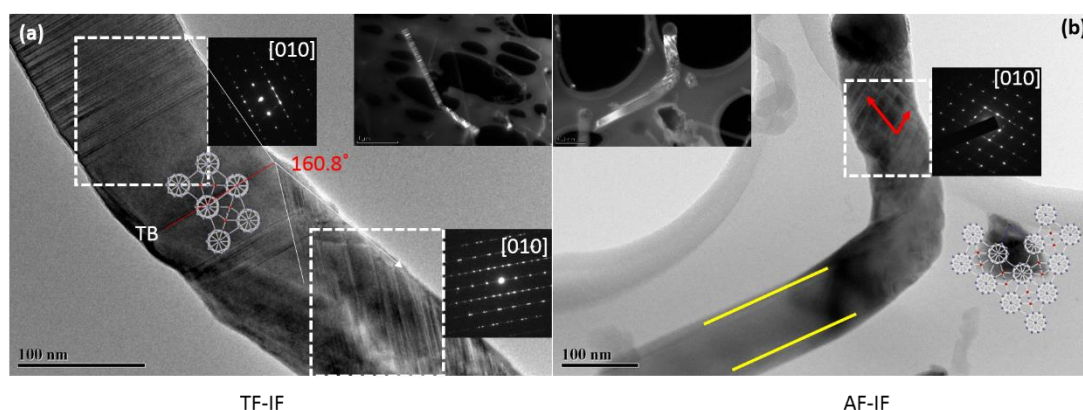


Figure 3.15: TEM images of (a) TF-IF and (b) AF-IF kinked NWs with inset DF TEM images showing the transition. (Courtesy of Dr. Baobao Cao)

### 3.2.9 Growth Mechanisms

The kinked B<sub>4</sub>C NWs discussed in this dissertation generally involve with planar defects (AF, TF, IF) formed at (100) planes, which is probably due to the relative low stacking fault energy (76 mJ/m<sup>2</sup>) of B<sub>4</sub>C.<sup>222</sup> Stacking faults or twins at (100) planes are also frequently being observed in bulk B<sub>4</sub>C samples.<sup>223-225</sup> Here our focus is to understand and discuss how those kinked B<sub>4</sub>C nanowires were grown. As mentioned in the experimental section, the as-synthesized NWs were grown following a VLS mechanism. In VLS grown NWs, catalyst is the key to control the diameter and morphology. It is believed that the liquid droplet (catalyst)'s dynamics caused by the instability at the solid-liquid interface are the driving force for kinking during the growth process.<sup>162,226,227</sup> Catalyst shape and configuration also play key roles on leading defects as well as kinks formation.<sup>228</sup> This is also adapted to rationalize the kinking in the kinked B<sub>4</sub>C NWs.

Figure 3.16 presents three representative TEM images of the catalysts found on kinked B<sub>4</sub>C NWs, which are in an irregular shape (broken ball, triangle and sharp tip) and do not cover the whole cross section of the nanowires compared to those hemisphere catalysts for straight B<sub>4</sub>C NWs. The catalysts shown in Figure 3.16 (a) and (b) decompose and diffuse to the side surface of the nanowires, and lead the growth of a TF-TF kinked NW and AF-TF kinked NW respectively. Moreover, the catalysts shrink slightly at the right corner of the interface between catalyst and nanowires and the diffusion occurs at the left side. Catalyst shown in Figure 3.16 (c) shrinks even more, but without diffusion. Meanwhile the one shown in Figure 3.16 (d) only contacts with

nanowire partially. The catalyst in Figure 3.16 (e) sits on top of an IF nanowire segment and leaves part of the facet exposed. Though it looks like the catalyst was partially removed, no diffusion was found along the nanowires, which also agree with our previous hypothesis: catalyst may be in a partially liquid status for AF nanowires. By zooming in to the interface, an identical “zig-zag” line was observed as in the AF nanowires. Figure 3.16 (f) shows a catalyst completely migrates to the side surface of an AF nanowire segment. These findings prove that the catalysts are extremely unstable during the kinked NWs’ growth and thus results in kinking.

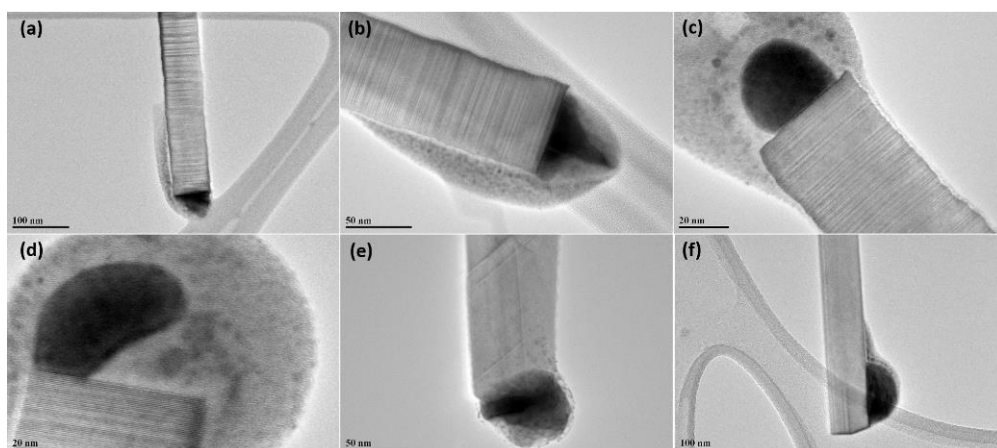


Figure 3.16: Catalysts with different shapes in kinked boron carbide nanowires.

The schematic diagram of the possible growth mechanisms for most cases is shown in Figure 3.17. The growth mechanism of AF-AF cases with kinks being visible in off-zone while not in in-zone condition is not quite well-understood and thus is not presented here. The first panel of Figure 3.17 shows the growth of TF-TF kinked NWs. First, straight TF NW was grown with liquid catalyst sitting on top of the flat surface,

as shown in Figure 3.17 (a). Then, with a small perturbation (unstable gas flow or temperature), the catalyst might slightly move away from the top surface (Figure 3.17 (b)). As the synthesis process continues, the arc shape transition area forms either with or without defects (Figure 3.17 (c)). Eventually, the catalyst completely wets the other same plane facet (100) of lowest surface energy and stable configuration, leading the NW to grow in the direction perpendicular to the new wetted facet (Figure 3.17 (d)). However, the catalyst may also wet another equivalent facet which is out-of-plane (010). This causes the subsequent segment to grow in an out-of-plane direction, as shown as dash line in Figure 3.17 (e) and (f). Figure 3.17 (g) and (h) shows the initiation of inclined faults at the liquid-solid-vapor triple phase corner and the subsequent IF segment was grown following the catalyst. The possibility of growing an AF segment after TF segment is very low, which probably due to the energy required to move the catalyst to the side surface is much higher than to the other facet. This is also confirmed by examining the catalyst final position on the nanowires, in which the catalyst was prone to sit at the end of TF segment in most of examined AF-TF NWs. Figure 3.17 (i) shows the initial stage of growing AF segment NW. As the catalyst may move away from the surface (Figure 3.17 (j)), the AF NW continues to grow at a small slope and subsequently, the final morphology of the NW will resemble the one a “step” shown in Figure 3.17 (k) while maintaining the growth direction. But, the catalyst may shift to the side surface and gradually pin off the top surface and completely wet the side surface, as shown in Figure 3.17 (l) and (m). After that, the catalyst will drive the NW to grow in the direction perpendicular to the defect plane, which results in AF-TF

kinked NW. For AF-IF NWs growth, the catalyst may stabilize right on top of two surfaces since the IFs stack in two directions and two inclined facets form.

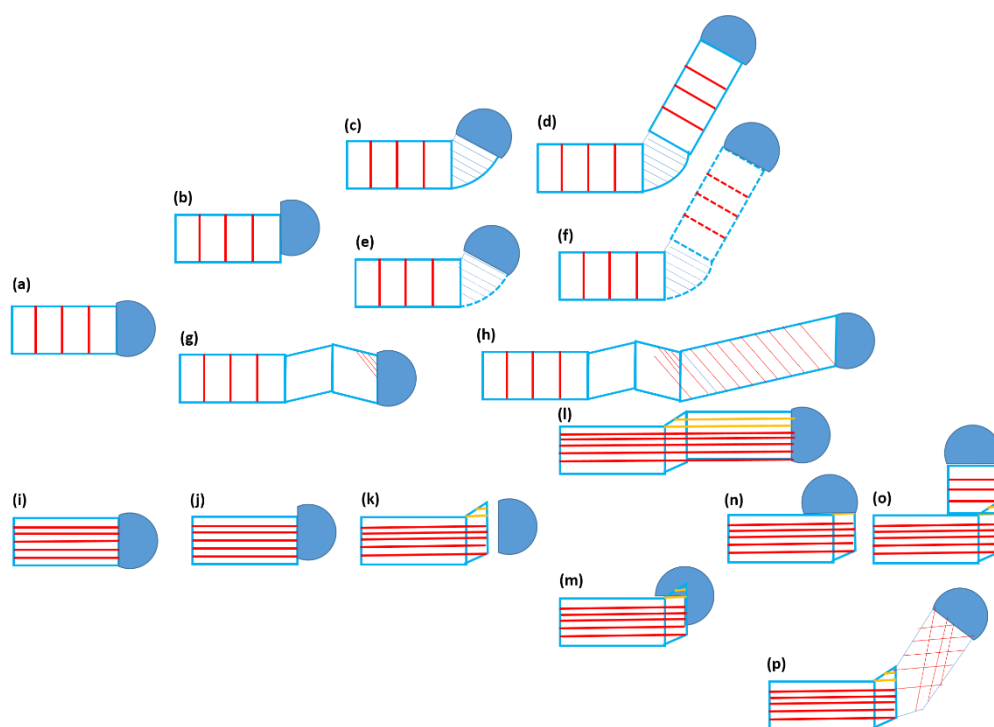


Figure 3.17: Schematic drawing of the growth mechanisms of TF-TF, TF-IF kinked nanowires (starting from (a)) and AF-AF, AF-IF kinked nanowires (starting from (i))

### 3.2.10 Conclusion

In conclusion, a detailed structural investigation of kinking in  $B_4C$  NWs was systematically performed via extensive TEM examination of tens of kinked  $B_4C$  NWs. The two segments of as-synthesized kinked  $B_4C$  NWs could be the combination of either any two of TF, AF and IF planar defects except the combination of two IF segments, which gives total 5 cases of kinked  $B_4C$  NWs, *i.e.*, TF-TF, AF-AF, AF-TF, TF-IF, AF-IF kinked NWs. The kinked  $B_4C$  NWs with multiple kinks also exist but

they are not structurally coherent because the kink angles and crystallographic orientation vary. Even within each of the five cases, the structure, particularly at the transition area, may be different.

It is necessary to perform TEM examination of the kinked NWs before studying their transport properties since the usual optical microscope and SEM examinations will not be able to distinguish subtle defects, whereby they may strongly affect the transport properties. Only by doing so, should researchers be able to establish the true structure-property relation. Additionally, the growth mechanism for each case of kinked B<sub>4</sub>C NW is proposed based on the dynamics of liquid droplet (catalyst), which divided the kinked NWs' growth into several steps. The current work extends the analysis of kinked NWs from simple crystal systems to complex ones.

## CHAPTER 4: THERMAL TRANSPORT AND REPRESENTATIVE $ZT$ OF STRAIGHT AND KINKED NANOWIRES

In this chapter, the transport properties, especially thermal transport properties of both straight and kinked boron carbide nanowire were thoroughly explored experimentally. This is a collaborative work with Dr. Deyu Li's group at Vanderbilt University. The thermal conductivity measurement and analysis are done by Dr. Li's group. Meanwhile, we are our responsible to conduct the structural characterization and analysis of the boron carbide nanowires. The correlation between structure and thermal conductivity is conducted by both groups.

### 4.1 Background

Owing to high temperature stability and decent figure of merit ( $ZT$ ), boron carbide has long been projected as a type of promising thermoelectric (TE) materials.<sup>39,229</sup> However, the measured thermal conductivity, electrical conductivity and Seebeck coefficient are often obtained from hot pressing polycrystalline bulk boron carbide samples with a wide range of grain sizes due to the extreme challenge of synthesizing high quality single crystalline samples.<sup>40,230-232</sup> As such, the measured properties include the contributions from the grain boundaries and suffer from the average effects. Boron carbide nanowires with highly crystalline nature offer an opportunity to eliminate abovementioned structure-properties uncertainty. In addition, it is believed that the low dimensional nanostructures would have superior TE properties compared

to their bulk counter parts.<sup>233,234</sup> However, transport properties, particularly thermal transport properties of boron carbide nanowires with stacking faults and kinks have not been well explored experimentally.

In this chapter, the experimental thermal conductivities of single crystalline boron carbide nanowires of different structures and compositions are reported. Different parameters, such as wire diameter, carbon concentration, stacking faults orientation and density, and especially kinks, which might affect the thermal transport of boron carbide nanowires, have been extensively explored. The results present a comprehensive picture of structure-thermal properties relation of boron carbide nanowires and provide important physical insights into tuning the thermal transport properties of the nanowires.

## 4.2 Experiments

Single crystalline boron carbide nanowires were synthesized in a LPCVD system as mentioned in the previous chapter. With the help of a home-built micromanipulator, individual boron carbide nanowires were then picked up and transferred to a copper grid with lacey carbon for structural investigation using TEM, which serves as a key process to identify appropriate nanowires for the subsequent thermal test. The TEM characterization reveals two dominant types of stacking faults orientation inside the boron carbide nanowires, *i.e.*, transverse faults (TF) and axial faults (AF).<sup>103</sup> The fault density of AF nanowires was also extracted from HRTEM image by dividing the number of total atomic planes and the number of stacking fault planes. In addition to straight boron carbide nanowires, kinked ones are also observed,

as described in detail in Chapter 3. The carbon concentration was measured by both EELS and EDS, which provide comparable results in majority nanowires (within 2%), as presented in Appendix A.

The characterized nanowires were then transferred to a specific suspended micro-device for subsequent thermal properties measurements from 20 to 420 K, which were conducted in a cryostat (Janis-CCS 450) under a high vacuum level ( $< 1 \times 10^{-6}$  mbar). In addition, dual radiation shields with an inner one mounted on the sample holder directly, were utilized to minimize the effects of radiation heat transfer. Figure 4.1 (a) presents the schematic drawing of this dual radiation shield setup, in which a micro-device with a nanowire bridging across the stage, as shown in Figure 4.1 (b). The background thermal conductance ( $G_{bg}$ ) between the two suspended membranes was measured separately and subtracted from measured thermal conductance of the nanowires. Moreover, in order to reduce contact thermal resistance, the contacts between the nanowire and the suspended membranes were enhanced with EBID of platinum (Pt). With this EBID treatment, the contact thermal resistance could be minimized to a negligible level, which is confirmed by measuring the Seebeck coefficient from different sets of electrodes following the approaches as demonstrated by Mavrokefalos *et al.*<sup>235</sup>. In Figure 4.1 (c), a long nanowire contacts with the suspended membranes at four points (electrodes) and the Seebeck coefficients from both outer two (1,4) and inner two electrodes (2,3) were measured simultaneously. The result shows that both measurements overlapped each other essentially (Figure 4.1 (d)).

This indicates negligible temperature difference between 1 and 2, 3 and 4, and the contact thermal resistance contributes merely to the total measured quantity.

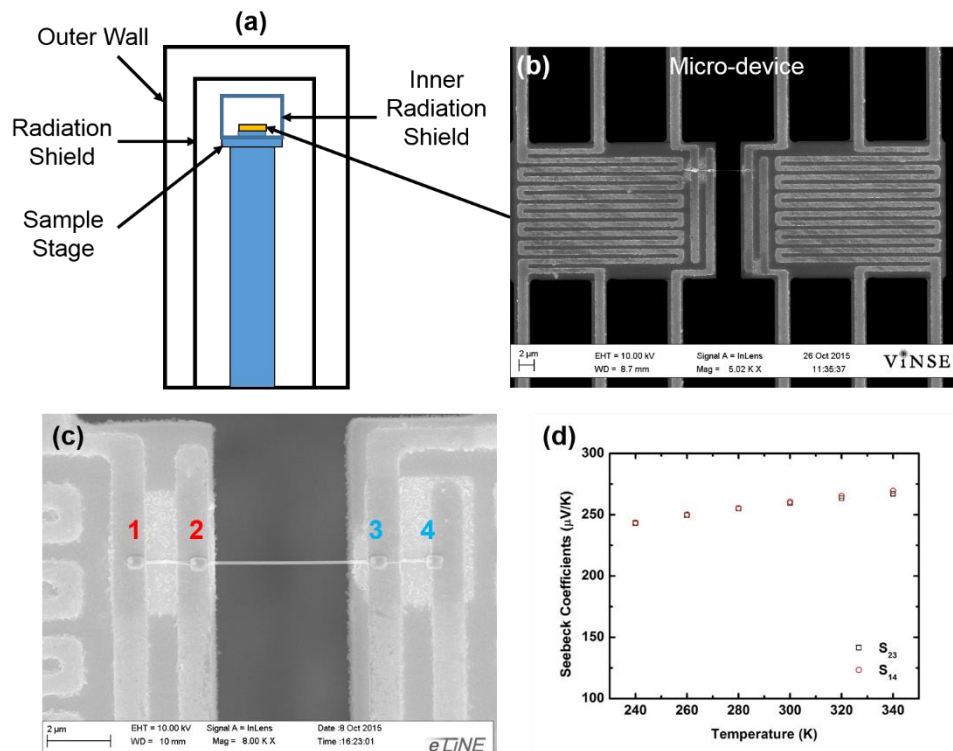


Figure 4.1: (a) Schematic drawing of the dual radiation shields setup; (b) an actual micro-device with a nanowire secured on it; (c) a long nanowire with 4-point contacts suspended on the micro-device; (d) Seebeck coefficients comparison between the electrodes positioned at 1,4 and 2,3.

### 4.3 Results and Discussions

A large number of boron carbide nanowires (> 50 nanowires) have been measured and subsets of samples with only one parameter different from each other are carefully selected to extract the true effects of each factor since our examined boron carbide nanowires are of different diameters, carbon concentrations, stacking faults

orientations/densities, and straight/kinked morphologies. However, it is crucial to confirm that measured thermal conductivities overlap with each other for such complex nanowires of similar structure, diameter and composition to make sure that the extracted trends are physically meaningful. Figure 4.2 plots the thermal conductivities of three TF nanowires with  $\sim 50$  nm diameter and  $\sim 14\%$  carbon concentration. It is obvious that the measurement results of these three nanowires almost overlapped, suggesting that it is still feasible to extract the effects of sole parameter through comparing data from samples with only one parameter as a variable.

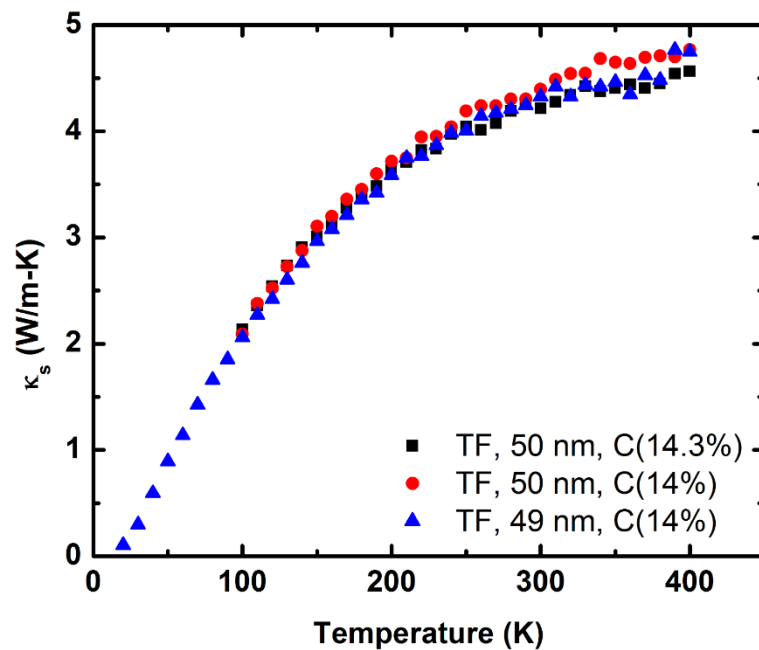


Figure 4.2: Plot of thermal conductivities from three TF nanowires with similar diameter and carbon concentrations.

#### 4.3.1 Carbon Concentration

It has been found that thermal conductivity of bulk polycrystalline boron carbides becomes larger as the carbon concentration increase even though the reported data are quite scattered.<sup>40,236,237</sup> This general trend is confirmed in both TF and AF boron carbide nanowires during our measurement. As mentioned earlier, boron carbide could have carbon concentration ranging from 8-20%. In our boron carbide nanowires, majority have a carbon concentration of 13~15% with only a small number of nanowires falling out of this range from the EDS/EELS measurement. Figure 4.3 (a) and (b) presents two sets of TF and AF nanowires' thermal conductivity plots at different carbon concentration. As shown clearly, the nanowires with lowest carbon concentration (9.3% or 9.5%) exhibit lowest thermal conductivity. Note that, the diameters of these nanowires are not same, but our strategy here is to select nanowires with higher carbon concentrations having diameter similar or smaller than those with lower carbon concentrations. In this way, any effects from phono-boundary scattering will counter the trend of the carbon concentration; therefore, the actual thermal conductivity increase with carbon concentration should only be more prominent. In addition, the fault density of the three AF nanowire shown in Figure 4.3 (b) is different as well, but the fault density found to have negligible effect on the thermal transport of boron carbide nanowires, which will be discussed later.

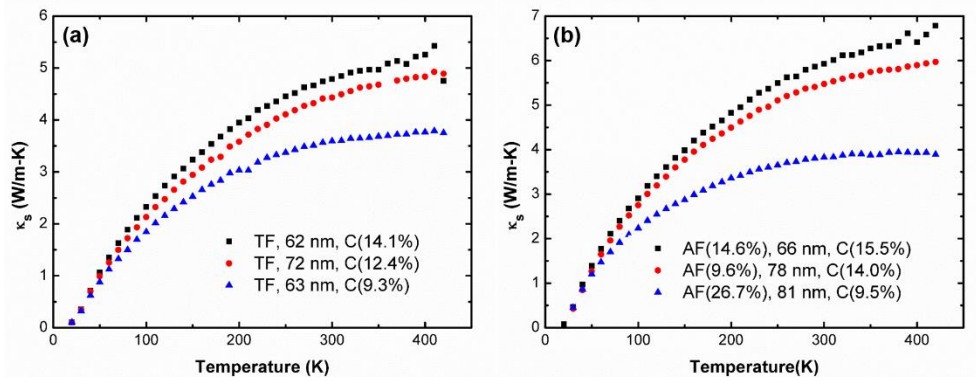


Figure 4.3: Thermal conductivities of TF (a) and AF (b) nanowires with similar diameters while different carbon concentrations

The carbon dependent thermal conductivity in boron carbide has been mainly ascribed to the more ordered molecular structure and reduced structural defects as carbon concentration increases.<sup>236</sup> Boron carbides have a rhombohedral unit structure with eight 12-atom icosahedra locating at the corners and one 3-atom chain occupying the longest diagonal of the unit. Depending on the carbon atoms' substitution sites (icosahedra or 3-atom chain), a C-B-C structure is preferred for higher carbon concentration, while either C-B-B or B-B-C for that of lower carbon concentration. Moreover, C-B-C structure is more ordered and structure defects are reduced as the carbon concentration increases, which would benefit the phonon transport.<sup>33</sup>

#### 4.3.2 Diameter

Besides carbon concentration dependence, the thermal conductivity of boron carbide nanowires also behaves a clear dependence on diameter due to strong phonon boundary scattering at the nanowire surface,<sup>84,86</sup> as confirmed in both TF and AF nanowires. Figure 4.4 (a) plots the thermal conductivity of three TF nanowires with

similar carbon content (13.7%-14.1%). As the diameter decreases, the thermal conductivity goes down as well. In Figure 4.4 (b), the fault densities of three AF nanowires are similar (20%), while the carbon contents vary. However, the 43 nm nanowire with the highest carbon content (16.3%) still has the lowest thermal conductivity, which actually emphasizes the diameter dependence since the highest carbon content was supposed to result in a highest thermal conductivity.

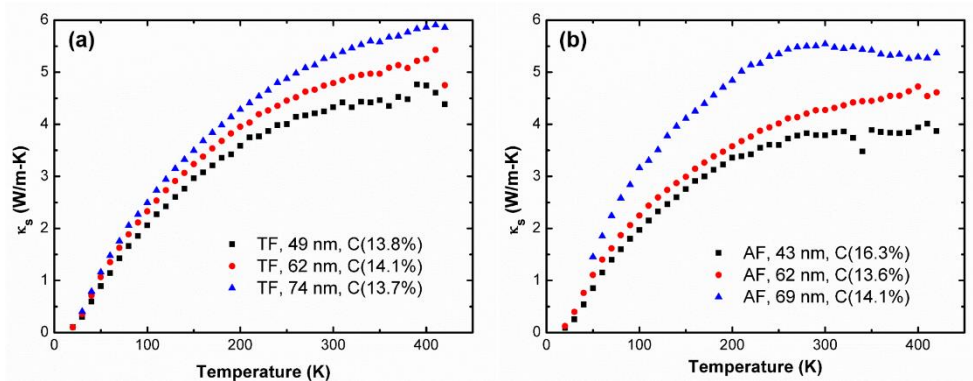


Figure 4.4: Thermal conductivities of two groups of nanowires with different diameters: (a) TF, (b) AF

### 4.3.3 Fault Density

It is commonly believed that any structural defects, such as planar defects (twins or stacking faults), would have significant suppressing effects on phonon transport.<sup>238-</sup>

<sup>241</sup> Therefore, it is expected to see a large reduction of thermal conductivity if the fault density is high. However, looking at the AF nanowires with similar diameters (40 nm) but with varying fault densities, it was found that almost no change happens to the thermal conductivity until the fault density reaches 39% and thermal conductivity rises

beyond this point (Figure 4.5 (a)). Figure 4.5 (b) shows an example of how to calculate the fault density of AF nanowires from a HRTEM image. A possible explanation to this observation is at the stacking faults planes, a large portion of the phonons will transport specularly, which will not pose significant resistance to the thermal transport, while at the nanowire surface, all phonons will be scattered or reflected and this process is nearly diffusive. For high fault density nanowires, the surface scattering is suppressed, which in turn leads to a high thermal conductivity.

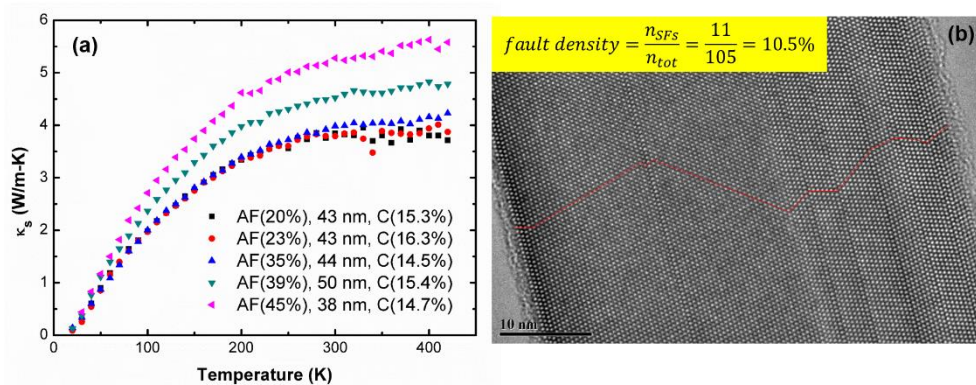


Figure 4.5: (a) Thermal conductivities of five AF nanowires with variable fault densities; (b) an example showing how to calculate the fault density of AF nanowires

#### 4.3.4 AF vs. TF

As mentioned before, our as-synthesized nanowires display two types of stacking faults orientations, TF and AF. It is initially expected that the TF nanowires would have a lower thermal conductivity than AF nanowires since the planar defects of TF nanowires are perpendicular to the phonon transport direction, which would pose more resistance to the specular or diffuse phonon transport. In order to do a systematic

comparison, the nanowires were divided to four groups with similar diameters in each group but different stacking faults orientation, as shown in Figure 4.6. Though the carbon concentration also varies in each group, a general trend that TF nanowires have a lower thermal conductivity than AF ones could still be extracted in Figure 4.6 (b) (group 60 nm) and (d) (group 80 nm). The violation of this trend in Figure 4.6 (d) is from an 81 nm nanowire (purple triangle), whose thermal conductivity is close to the TF nanowires'. Note that this is mainly due to its lower carbon concentration (11.2%) than the rest of nanowires in the group, which essentially reduces its thermal conductivity as a result of the carbon concentration dependency. However, this trend is hard to observe based on the data shown in Figure 4.6 (a) (group 50 nm) and (c) (group 70 nm). Though, in Figure 4.6 (c) the AF nanowire has a higher thermal conductivity than that TF ones, this may be attributed to its higher carbon concentration. However, these data show that phonon transport is generally more difficult in TF nanowires than that of AF nanowires..

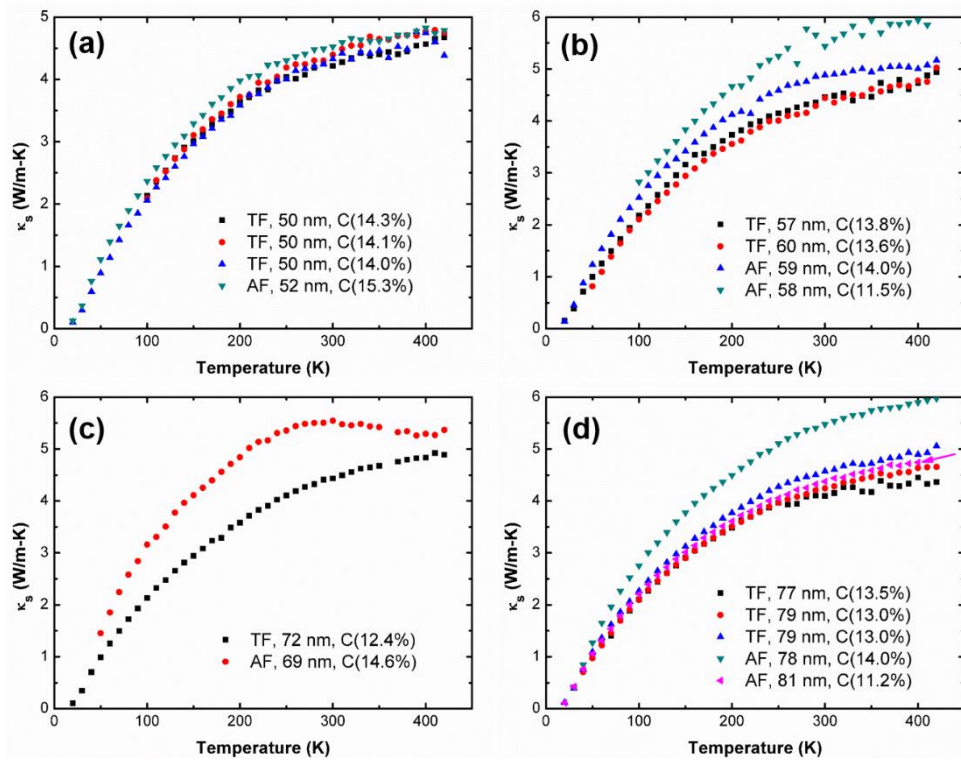


Figure 4.6: Thermal conductivity comparison between TF and AF nanowires: (a) group 50 nm, (b) group 60 nm, (c) group 70 nm and (d) group 80 nm.

#### 4.3.5 Straight vs. Kinked

With a good understanding of the effects of carbon concentration, diameter, and stacking faults densities and orientations for straight boron carbide nanowires, next the effect of kinks on thermal transport is explored. The kinks that we are investigating here are of two simple ones, *i.e.*, TF-TF with a  $106.9^\circ$  kink angle and AF-TF with a  $90^\circ$  kink angle, as shown in Figure 4.7 (e) and (f). The detailed structural investigation of those two kinks could be found in Chapter 3. Based on the difference in diameter, three subset data of TF-TF kinked nanowires are plotted in Figure 4.7 (a), (b) and (c), which all show significant reduction of thermal conductivity for kinked nanowires. Figure 4.7 (d) displays the comparison between a straight AF nanowire, a straight TF nanowire, an

AF-TF kinked nanowire, and a TF-TF kinked nanowire. Again, kinked nanowires exhibit lower thermal conductivity as compared to the straight ones. In addition, the AF-TF kinked nanowire shows less thermal conductivity reduction than that of TF-TF kinked one, which suggests substituting one TF arm with AF will enhance the thermal transport. This observation supports the idea that more resistance is imposed in TF nanowires, as discussed in section 4.3.4.

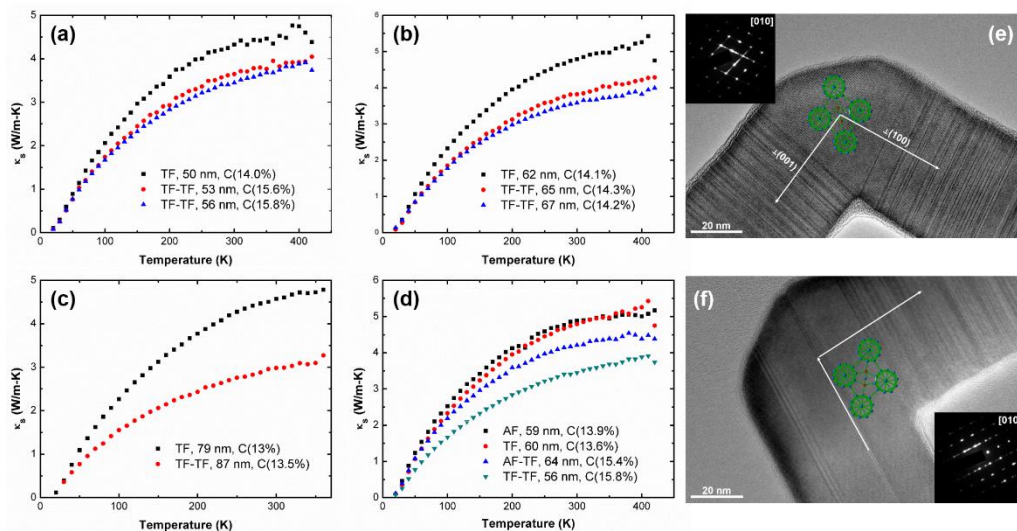


Figure 4.7: Thermal conductivity of straight nanowire vs kinked nanowires based on different diameter group.

It is worth noting that the straight nanowires selected to compare with the kinked ones all have similar or smaller diameters and lower carbon concentrations than the kinked ones. By doing this, it is for sure that the reduced thermal conductivity of the kinked nanowires is indeed arose from the effect of kinks instead of other parameters. In addition, the kinked region of the tested kinked nanowires is of single crystalline

without any defects, as confirmed from the TEM examination, which suggests the reduced thermal conductivity cannot be emerged from low quality crystalline structure at the kinks. Moreover, the thermal conductivity is reduced 15% to 40% at room temperature for different groups of nanowires. The kink actually poses a resistance which is 6 to 16 times greater than a straight nanowire segment if we assume the equivalent length of the kink is 100 nm.

Assuming the phonons mean free path contributing to thermal transport is large in boron carbides, which is reasonable because of the extremely complex structure, the phonon transport in the kinked region is mostly ballistic and the reduced conductance comes from the smaller view factor between the two ends of the kinked region than that between the two ends of a straight wire of equivalent length. However, a ray tracing Monte Carlo simulation performed on a 'L' shape (kinked) wires with square cross section shows the thermal conductivity reduction rate is far smaller than that in boron carbide nanowires because of the low resistance. For example, even with a specular reflection boundary condition that yields a larger conductance reduction, the resistance only increases by about 25%, much smaller than the required 6 to 16 times hike to lead to 15-40% thermal conductivity reduction.

Though there are no direct experimental studies of thermal conductivity reduction by kinks in nanowires, a molecular dynamics (MD) simulation conducted by Jiang *et al.*<sup>94</sup> gives some hints on how kinks can affect thermal transport through silicon nanowires. Their results show a single kink can reduce the thermal conductivity by about 20% at 300K for a kinked silicon nanowire of 1.1 nm diameter, which falls in the

range (15%-40%) of our experimental observed reduction though our boron carbide nanowires are of much larger diameter (>50 nm). They attributed the thermal conductivity induced by kink to phonon pinching effects, in which phonons have much smaller chance to transmit through the kink since the atoms vibrations of the same mode in the two sides of the kink are in orthogonal direction. This pinching effect could be adopted to explain the obvious reduction of thermal conductivity in our kinked boron carbide nanowires. However, this transport phenomenon dominated by the phonon wave nature requires further theoretical and modeling investigations. But one interesting group of data from our measurements seems to support the viewpoint. As can be seen in Figure 4.8, a nanowire with clear stacking faults and dislocations in the kink region has a thermal conductivity smaller than that of a straight nanowire but larger than that of a kinked nanowire without defects in the kink region. They all have similar diameters and carbon concentrations. In the phonon pinching effects, the scattered phonons essentially undergo a mode conversion process to transmit into the other side of the kink. The phonon mode conversion would be enhanced by the structural defects, which helps phonon scattering, and thus more phonons will be directed into the other side of the kink. In other words, phonon scattering actually promotes heat transport instead of posing resistance, similar to the phenomenon observed for the contact thermal resistance between two multi-wall carbon nanotubes.<sup>242</sup>

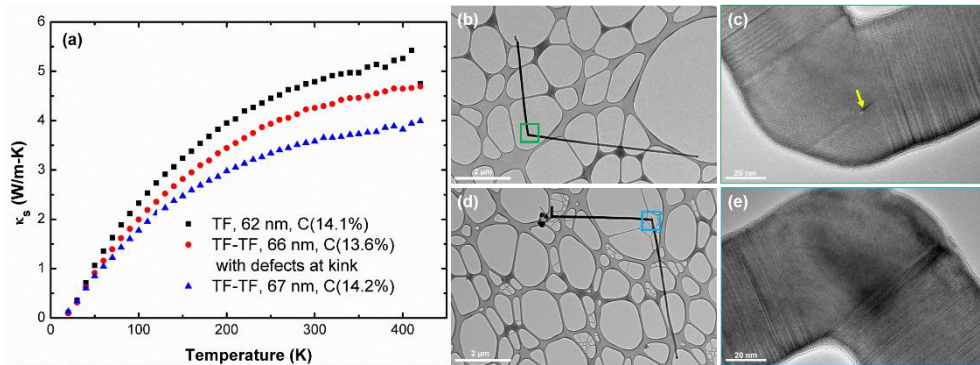


Figure 4.8: Thermal conductivity comparison ((a)) between TF-TF kinked nanowire with defects ((b) and (c)) and without defects ((d) and (e)) in the kink region.

#### 4.3.6 Figure of Merit ( $ZT$ )

As a key parameter to describe the performance of TE materials, the figure of merit ( $ZT$ ) of boron carbide nanowires was evaluated preliminarily. With the same micro-device, we are able to measure the Seebeck coefficient and electrical conductivity as well. However, due to the fact that a 1-2 nm thick oxide sheath always exists as the outer layer of the boron carbide nanowire and its insulating properties, this oxide sheath must be etched away at the position where EBID of Pt locates to ensure a good ohmic contact. Figure 4.9 plots the thermal conductivity (a), Seebeck coefficient (b), electrical conductivity (c), and  $ZT$  (d) of two AF nanowires. The 56 nm nanowire has a smaller thermal conductivity, a larger Seebeck coefficient, but much smaller electrical conductivity, which results in a smaller figure of merit ( $ZT$ ), 0.004 at 420 K than that of the other one, 0.009 at 420 K. Note that, the current measured  $ZT$  value of boron carbide nanowires is much smaller than those (0.15-1) of bulk boron carbides at high temperature ( $>1000$  K), but is larger than those (0.0005) at low temperature ( $< 500$

K). The enhancement of TE performance is apparent in boron carbide nanowires. It is expected to see an even larger enhancement as higher temperature is used in the test since the electrical conductivity increases with the temperature. The next step is to extend the measurements to higher temperature and to proceed with measuring the figure of merit of straight TF nanowires and kinked nanowires, which might have larger  $ZT$  value than the AF ones.

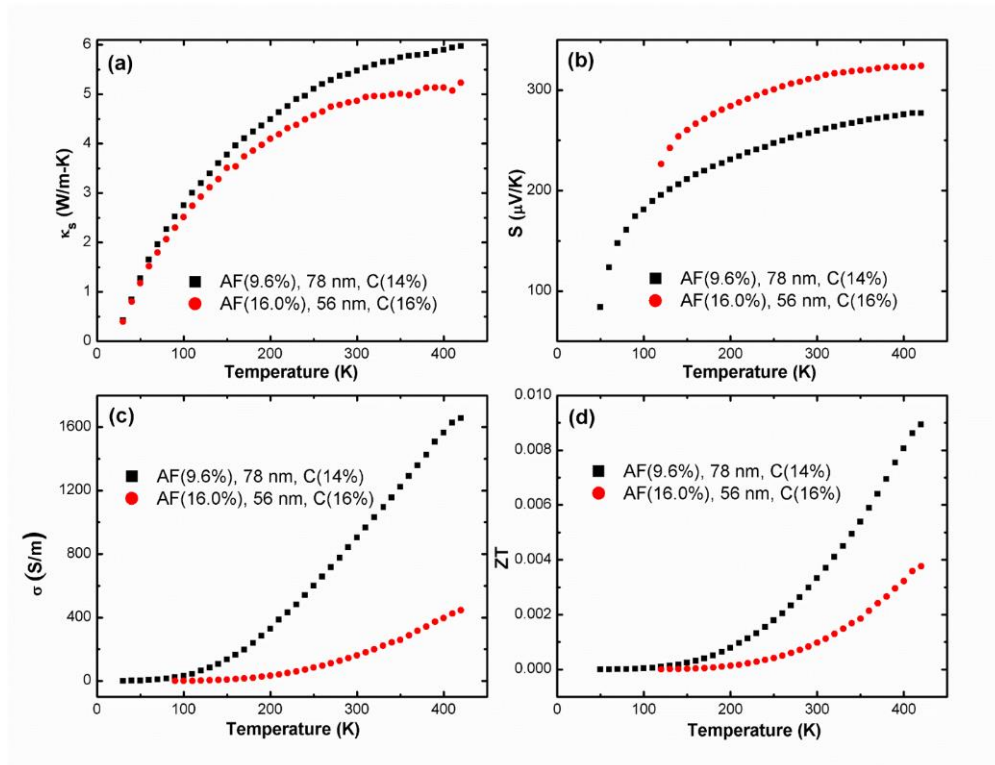


Figure 4.9: Measured thermal conductivity (a), Seebeck coefficient (b), electrical conductivity (c), and calculated  $ZT$  (d) of two AF nanowires.

#### 4.4 Conclusions

In summary, we have experimentally measured the thermal conductivity of boron carbide nanowires of different diameters, carbon concentrations, stacking fault orientations/densities and geometries (straight or kinked). Several general trends of thermal conductivity in boron carbide nanowires are discovered and confirmed: (1) carbon concentration dependence: higher carbon concentration leads to higher thermal conductivity because of more ordered structure and less defects (2) diameter dependence: smaller size leads to lower thermal conductivity due to enhanced phonon boundary scattering; (3) TF nanowires generally have lower thermal conductivity than the AF ones; (4) stacking fault density seems to only have marginal effects; (5) kinked nanowires show significantly reduced thermal conductivity, which might come from the need for phonon mode conversion before they can propagate into the opposite side of the kink. In addition, the figure of merit ( $ZT$ ) of boron carbide nanowires is analyzed preliminarily, in which the lower value is due to the low temperature. This discovery provides new insights into phonon transport in the complex boron carbide nanowires and the reduced thermal conductivity of the kinked nanowires could further boost the thermoelectric properties of these nanowires.

## CHAPTER 5: RAMAN SPECTROSCOPY ON INDIVIDUAL BORON CARBIDE NANOWIRES

### 5.1 Background

As discussed in Chapter 1, the structure of boron carbide is really complex and the debate still exists on the exact carbon positions inside the unit cell even from various theoretical calculations and experiments, such as free-energy calculation,<sup>243</sup> density functional theory,<sup>244,245</sup> electronic transport,<sup>39</sup> thermal transport,<sup>236</sup> X-rays diffraction,<sup>246</sup> neutron diffraction<sup>247</sup> and electron-spin resonance<sup>248</sup> measurements. However, it is agreed that the carbon content and its position actually play important roles in determining the boron carbide's structure, i.e. order or disorder molecular structure. For instance, high carbon content ( $B_{12}C_3$ ) C-B-C chains, which have orientational symmetry, are believed to lead to more ordered structures than low carbon content ( $B_{13}C_2$ ) C-B-B chains with an agreement that one carbon atom resides within each icosahedron ( $B_{11}C$ ).<sup>33</sup> This structural change is well reflected from the thermal transport studies, in which higher carbon content boron carbides always exhibit larger thermal conductivity.<sup>236</sup> In addition, Raman spectroscopy, which has long been utilized to study the structure of boron carbide due to its sensitivity to the molecular bonds' vibrations, also provides evidences to support this view.<sup>33,249</sup>

Besides those molecular level disorders, some other defects, such as stacking faults are often observed in boron carbides, no matter bulks or nanostructures, due to a relative smaller stacking energy.<sup>222</sup> Moreover, it has been reported that Raman spectroscopy could also be used to detect stacking faults in several material systems, i.e. epitaxy grown silicon carbide (SiC)<sup>250-252</sup> and molybdenum diselenide (MoSe<sub>2</sub>)<sup>253</sup> crystals layers or thin films by monitoring some characteristic phonon modes. Disordered stacking faults will introduce either broadened or distorted Raman bands. A denser stacking faults typically will only lead to the widening of the full width at half maximum (FWHM) while not shifting the peak positions.<sup>252</sup> Moreover, Raman spectroscopy has been applied on identifying stacking faults in individual silicon (Si) and germanium (Ge) nanowires.<sup>138,172</sup> However, to the best of our knowledge, no study has been done to correlate the Raman spectroscopy with stacking faults in boron carbides. The main reason may be due to the complex structure and the large homogeneous range of boron carbide. Even though the synthesis of boron carbide thin films is relatively easy, the problem is the low quality of as-synthesized products, which usually have a polycrystalline nature. Here in this chapter, we investigate the effect of stacking faults including the orientations and densities on Raman scattering in high quality single crystalline boron carbide nanowires with minimal variation in carbon contents by means of micro-Raman spectroscopy. The purpose is to evaluate the possibility of utilizing micro-Raman spectroscopy as a quick tool to identify the defects in the as-synthesized boron carbide nanowires.

## 5.2 Experimental

Boron carbide nanowires were synthesized via LPCVD as usual. After growth, individual nanowires were either transferred to a lacey carbon TEM grid or to the edge of a thin glass slide, as shown in Figure 5.1 (a) and (b) respectively. In the former case, the nanowires were first examined by TEM first to identify the stacking faults types and to obtain information on the wire diameters and compositions, and then followed by micro-Raman spectroscopy examination. While in the latter case, the nanowires were initially subjected to micro-Raman spectroscopy examination and later transferred to the lacey carbon grid for subsequent TEM examination. In the latter method, the nanowires are able to lie down flatly, which results in an enhanced Raman scattering, but the risk is the nanowires might be lost during the transfer from glass slide to the TEM grid.

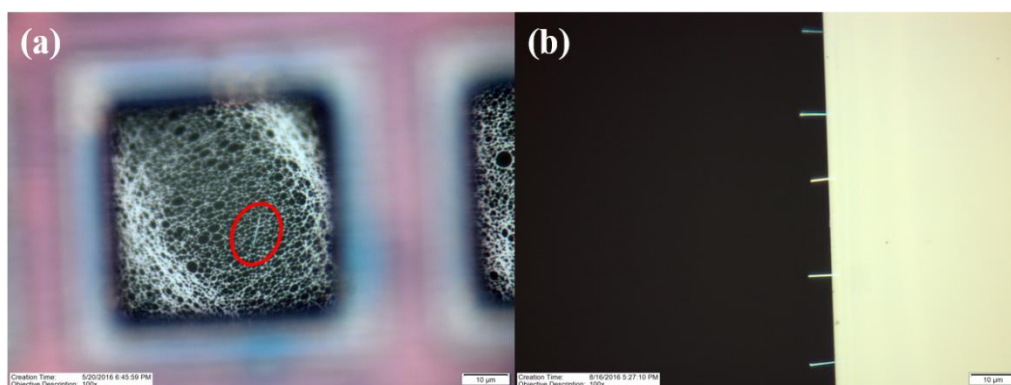


Figure 5.1: (a) An individual nanowire lies on the lacey carbon film of a TEM grid; (b) Several nanowires suspend on the edge a thin glass slide.

A Horiba Jobin-Yvon LabRam HR800 micro-Raman spectroscopy system with a spectral resolution  $0.5 \text{ cm}^{-1}$  is utilized to record the Raman spectra ranging from 100

to  $1200\text{ cm}^{-1}$  for all individual nanowires excited by a torus 532 nm laser made by Laser Quantum at room temperature (300K). Laser power could be tuned from 20 pW to 20 mW with the help of internal filters and an external neutral density filter. An Olympus BX 41 microscope with a motorized XY moveable stage is attached to focus the laser to a small spot ( $\sim 0.75\text{ }\mu\text{m}$  at 100x objective lens (N.A. = 0.9)) and locate the nanowires. In addition, in order to control the geometry configuration between the nanowires and incident laser, a high precision rotation mount ( $360^\circ$ ) from Thorlabs is placed on the moveable stage to support the glass slide, on which the TEM grid or thin glass slide is positioned. Moreover, TEM grids with nanowires were put on a gold coated PDMS strip to reduce the vibration and avoid the interference from the PDMS. The measurements are conducted in a backscattering configuration. The instrument was calibrated using a clean silicon chip as reference, which has a typical Raman peak at  $520.7\text{ cm}^{-1}$ .

### 5.3 Results and Discussions

#### 5.3.1 Test Optimization

It is known the Raman scattering intensity is greatly influenced by the specimens' Raman scattering cross-sections,<sup>189</sup> which is quite small for boron carbides. One way to get stronger Raman scattering in boron carbides is to use higher laser power since the signal is linearly proportional to laser intensity. While for nanowires including boron carbide nanowires, laser power should be kept very small ( $< 300\text{ }\mu\text{W}$ ) in order to avoid damaging or burning the samples as well as heating effect.<sup>172</sup> Besides the laser power, other parameters, such as substrates, nanowires' position, confocal hole size and

integration time, also affect the quality of the final Raman spectral during the measurements. Therefore, the test parameters are firstly optimized to obtain decent Raman scattering signal from individual boron carbide nanowires.

Depending on the substrates, the threshold of laser power may vary. As shown in Figure 5.2 (a), one nanowire on TEM grid got burnt within 3 minutes (acquisition time: 45 s, integration cycle: 1) when the laser power reaches 230  $\mu\text{W}$  (measured by a power meter from Thorlabs), as reflected from the Raman spectrum, in which there was a drop around  $900\text{ cm}^{-1}$  and the peak around  $\sim 1060\text{ cm}^{-1}$  shown in the other three Raman spectral at lower laser power almost vanished. However, one nanowire suspended on the glass slide's edge survived under the same conditions, even with longer exposure time. One hypothesis to explain this threshold difference is that the laser power intensity per area is larger for nanowires on TEM grid since the nanowires are often tangled (inclined or not flat). One more evidence to support this view is that even different nanowires on the same TEM grid show different laser power threshold due to their unique positions. Therefore, for later measurements the laser power is set as 120  $\mu\text{W}$  and 230  $\mu\text{W}$  for nanowires on TEM grid and on glass slide respectively. It should be noted that we mainly use nanowires suspended on the edge of a glass slide for subsequent parameters optimization because of the relative stronger Raman scattering.

Next parameter being optimized is the confocal hole size. As described in section 2.6, the Raman setup used has a confocal hole locating in front of the grating and detector, which is mainly being set for the confocal analysis. Typically, as the confocal hole size decreases, the confocal performance of the system improves since

out-of-focus Raman scattering light is eliminated by the confocal hole, for example, higher spatial resolution.<sup>254</sup> In addition, because of the small analysis volume of the samples in confocal mode, the signal level will decrease accordingly. In our case where the individual boron carbide nanowires' diameters are mostly less than 100 nm, the confocal hole should be set to a small diameter. Three small confocal hole sizes (100, 200 and 300  $\mu\text{m}$ ) were chosen for the comparison and optimization. As plotted in Figure 5.2 (b), the Raman spectrum collected at the smallest confocal size (100  $\mu\text{m}$ ) while with other parameters maintained same (230  $\mu\text{W}$ , 25 s acquisition time and 5 integration cycles) does exhibit stronger peaks. Hence, we used 100  $\mu\text{m}$  confocal hole for the subsequent measurements.

By knowing the appropriate laser power and confocal hole size, now the acquisition time and integration cycles are being studied. Obviously, one can imagine a longer acquisition time will accumulate more signals and more integration cycles are able to increase the signal/noise ratio and smoothen the spectrum. However, when dealing with such small nanowires, longer collecting time means there is a higher possibility of single nanowire being drifted away even though the vibration is minimized, especially for the nanowires on TEM grid. Figure 5.2 (c) displays the Raman spectra of a nanowire suspended on glass slide's edge recorded at different integration time. It is clearly seen that the Raman scattering intensity of longer acquisition time is stronger. However, in the practice, the longest acquisition time for one cycle is usually set no more than 60 s to avoid heating effect and sample shifting. Therefore, we did not go beyond 60 s. But it is surprised to observe negligible sample

shifting during the measurement even though the acquisition time was set to 60 s, which indicates our efforts on reducing the vibrations is in effect. Figure 5.2 (d) shows an example of how the number of integration cycles affects the Raman spectra. As can be seen, though both spectra are noisy because of the weak Raman scattering in boron carbide nanowires, more integration cycles lead to a relative smoother profile. Here, in order to be time-efficient, 10 cycles are used in our experiments.

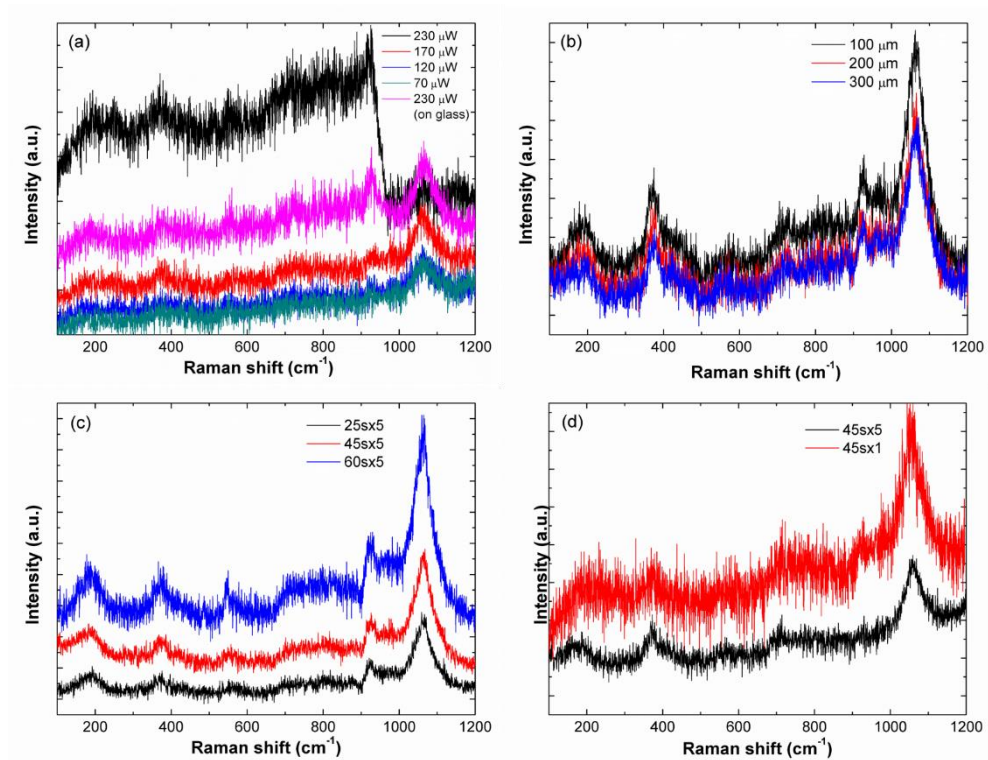


Figure 5.2: Optimization of laser power (a), confocal hole size (b), acquisition time (c) and integration cycles (d) for collecting micro-Raman spectrum of individual boron carbide nanowires.

Another parameter significantly affecting the Raman scattering in boron carbide nanowires is the nanowires' position or orientation, *i.e.* vertically or horizontally

aligned. As illustrated in the schematic drawing (Figure 5.3 (a)), the preferred growth direction of vertically aligned nanowires coincides with the y-axis, while horizontally aligned ones' overlaps with the x-axis. In addition, the laser propagates along the z-axis. The torus 532 nm laser being used has a TEM<sub>00</sub> spatial mode and vertical polarization direction, which means the electric field only oscillates in the y-axis direction, as indicated by the red sinusoidal line. Moreover, the laser spot (~750 nm) is much larger than the diameters of boron carbide nanowires. It is quite straightforward to imagine that the interaction range (~750 nm) between electric field and vertically aligned nanowires will be greatly larger than that (50~100 nm) of the horizontal aligned ones, which in turn will result in a stronger Raman scattering in the former ones. Moreover, the internal electrical field is different in aforementioned two nanowires' orientations. This is confirmed by our experimental data, in which there is almost no detectable Raman scattering in a horizontally aligned nanowire, while multiple peaks show up after aligning the same nanowire vertically, as shown in Figure 5.3 (b). The TEM examination reveals that the nanowire is a TF one. In order to confirm that the effect of nanowires' orientation is not related to stacking faults orientations. Figure 5.3 (c) shows the Raman spectra of another AF nanowire examined by micro-Raman at two different configurations and similar phenomenon was observed. Therefore, all nanowires were aligned vertically before acquisition of Raman spectrum began.

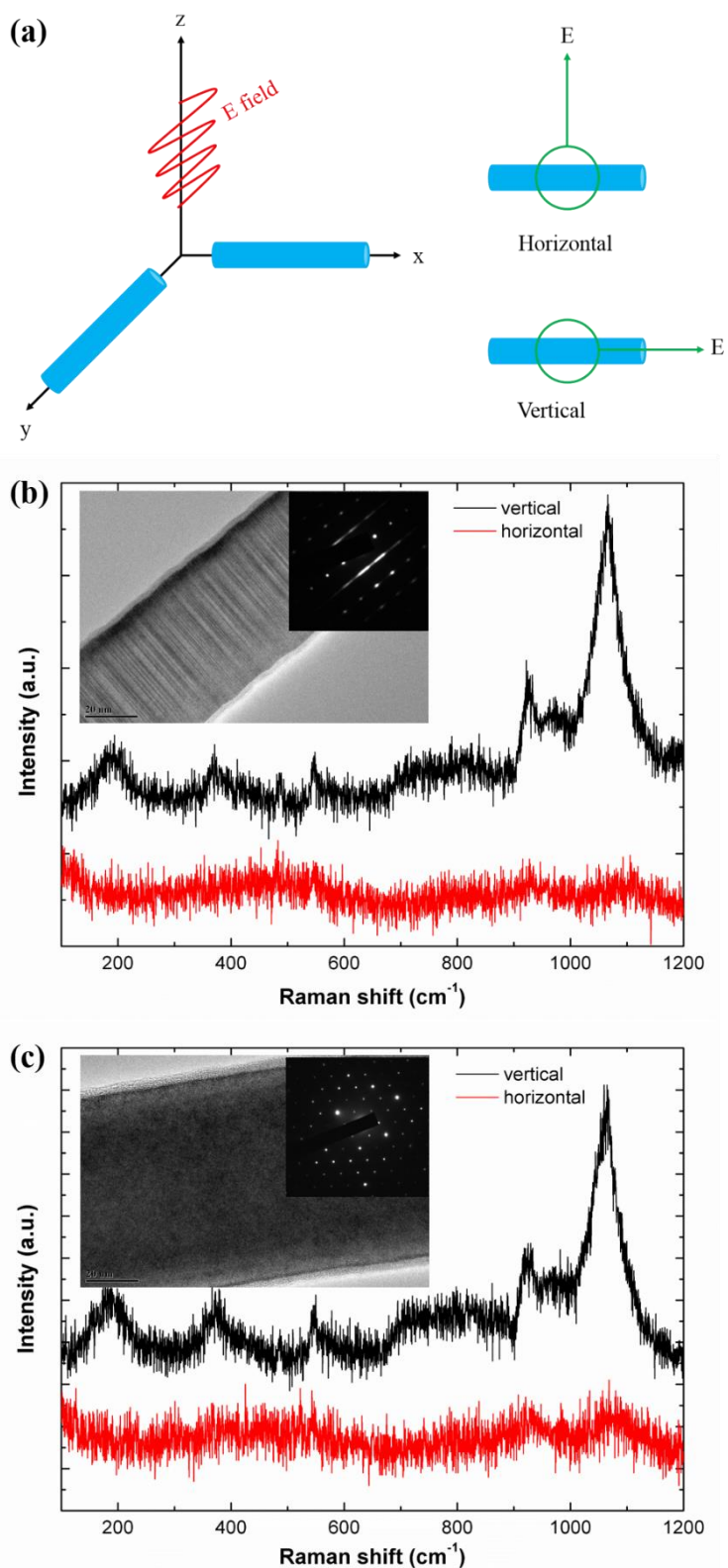


Figure 5.3: The effect of nanowires' positions on Raman scattering: (a) schematic drawing showing the general configuration between laser and nanowire, (b) A TF nanowire and (c) an AF nanowire's Raman spectra when vertically and horizontally placed. Insets are the corresponding HRTEM images and DPs.

### 5.3.2 Comparison Between Bulk and Nanowires

Raman spectra extending from 200 to 1200  $\text{cm}^{-1}$  of bulk single crystalline and polycrystalline boron carbide have been reported in many literatures.<sup>255-258</sup> However, because of the complex structure and uncertainty of the carbon positions, there is still debate on assigning the observed Raman peaks. But, it is agreed that carbon concentration affects the Raman scattering in boron carbide. As an example, Figure 5.4 (a) presents the micro-Raman spectra of boron carbide thin films prepared by LPCVD with different carbon concentrations.<sup>249</sup> In addition, a standard bulk single crystal boron carbide's Raman spectrum as a reference was shown in Figure 5.4 (a) as well. As can be seen in the Raman spectrum from the standard boron carbide (20 at% C), several broad and narrow Raman peaks at 270  $\text{cm}^{-1}$ , 320  $\text{cm}^{-1}$ , 481  $\text{cm}^{-1}$ , 531  $\text{cm}^{-1}$ , 728  $\text{cm}^{-1}$ , 830  $\text{cm}^{-1}$ , 970  $\text{cm}^{-1}$ , 1000  $\text{cm}^{-1}$  and 1080  $\text{cm}^{-1}$  are distinctively observed. In general, the Raman bands appearing in low frequency range ( $<600 \text{ cm}^{-1}$ ) are ascribed to the stretching vibrations of the three atoms chains associated with libration and wagging of the icosahedron containing C,<sup>33</sup> while those in high frequency range ( $>600 \text{ cm}^{-1}$ ) are caused by the vibrations of intra-icosahedra and inter-icosahedra.<sup>259</sup> As the carbon concentration decreases, the Raman profile in the low frequency region starts to change (*i.e.* diminishment of 270  $\text{cm}^{-1}$ , 481  $\text{cm}^{-1}$  and 531  $\text{cm}^{-1}$  bands, arising of a new 380  $\text{cm}^{-1}$  band). In the meantime, Raman bands between 600  $\text{cm}^{-1}$  to 1200  $\text{cm}^{-1}$  are relatively less affected, in which only a blue shift is observed in comparison with the reference Raman spectrum.

Figure 5.4 (b) presents two representative Raman spectra with distinctive profiles of our individual boron carbide nanowires, in which the top one is observed more often. Both nanowires are on TEM grids and the experimental parameters were set same. The major difference between these two Raman spectra arises within the lower frequency range in which carbon content plays important role. The top one has two broad Raman peaks at  $180\text{ cm}^{-1}$  and  $370\text{ cm}^{-1}$ , while the bottom one exhibits a Raman peak at  $270\text{ cm}^{-1}$  besides the  $370\text{ cm}^{-1}$  peak. In addition, the Raman peaks between  $600\text{ cm}^{-1}$  to  $1200\text{ cm}^{-1}$  in top spectrum shift slightly to lower value ( $1054\text{ cm}^{-1}$  to  $1047\text{ cm}^{-1}$ ,  $919\text{ cm}^{-1}$  to  $916\text{ cm}^{-1}$ ). The observation can be rationalized as a result of the slight change in the carbon concentration of the nanowires, although it was initially suspected that stacking fault orientation is responsible for it. Our boron carbide nanowires usually share a similar carbon concentration (13% to 15%) with occasional larger (16%) or smaller (11%) carbon concentration. The EDX measurements show the nanowire with top Raman spectrum has a carbon content of 15.7%, while the other one has a 14.0%. By comparing with Raman spectra shown in Figure 5.4 (a), it is found that boron carbide nanowires' typical Raman spectrum is close to the bulk ones with 13.8~16.2 at% C, which agrees well with our EDX analysis. The  $728\text{ cm}^{-1}$  and  $830\text{ cm}^{-1}$  Raman bands are not well resolved, but the bump within  $600$  to  $850\text{ cm}^{-1}$  shown in Figure 5.4 (b) does indicate certain Raman scattering exists. In addition, some distinct features are also observed between bulk (thin film) and nanowires, for instance, the strong  $480/531\text{ cm}^{-1}$  double peaks usually present in the bulk are barely seen in nanowires, new peaks at  $180\text{ cm}^{-1}$  or  $270\text{ cm}^{-1}$  emerge and large blue shifts of most

Raman bands occur. It has been confirmed that quantum size confinement effects in nanowires are able to broaden and downshift the Raman bands. In the case of our boron carbide nanowires having high density of stacking faults, some additional Raman bands may appear because of the structural disorder.

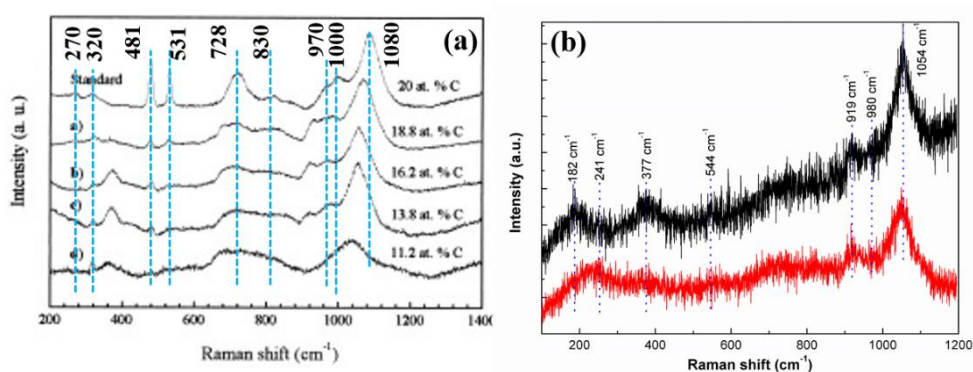


Figure 5.4: Raman spectra comparison between bulk boron carbide crystals (a)<sup>249</sup> and boron carbide nanowire (b)

### 5.3.3 Laser Power Dependence

As mentioned in the optimization part, laser power was the first parameter being investigated. With the help of the internal filters, the Raman spectra of several boron carbide nanowires were recorded at high power ( $\sim 200 \mu\text{W}$ ) and low power ( $\sim 20 \mu\text{W}$ ). An interesting finding is that the  $551 \text{ cm}^{-1}$  Raman peak becomes much more prominent (comparable to the strongest Raman peak) while the rest get suppressed at low power, as can be seen in Figure 5.5. The top two panels present the Raman spectra of two nanowires suspended on a  $\text{Si}_x\text{N}_y$  substrate. The strong and sharp peak locating at  $522 \text{ cm}^{-1}$  is mainly from Si. The bottom two panels plot the Raman spectra of nanowires

suspended on a glass slide. Usually high laser power will lead to the broadening and shifting of Raman peaks because of heating effect. However, it seems this is not the case in our boron carbide nanowires. One possible explanation is that the 3-atoms chain vibrations which gives rise to the  $551\text{ cm}^{-1}$  peak are more sensitive to low power laser due to the anisotropy properties of boron carbide.<sup>260</sup>

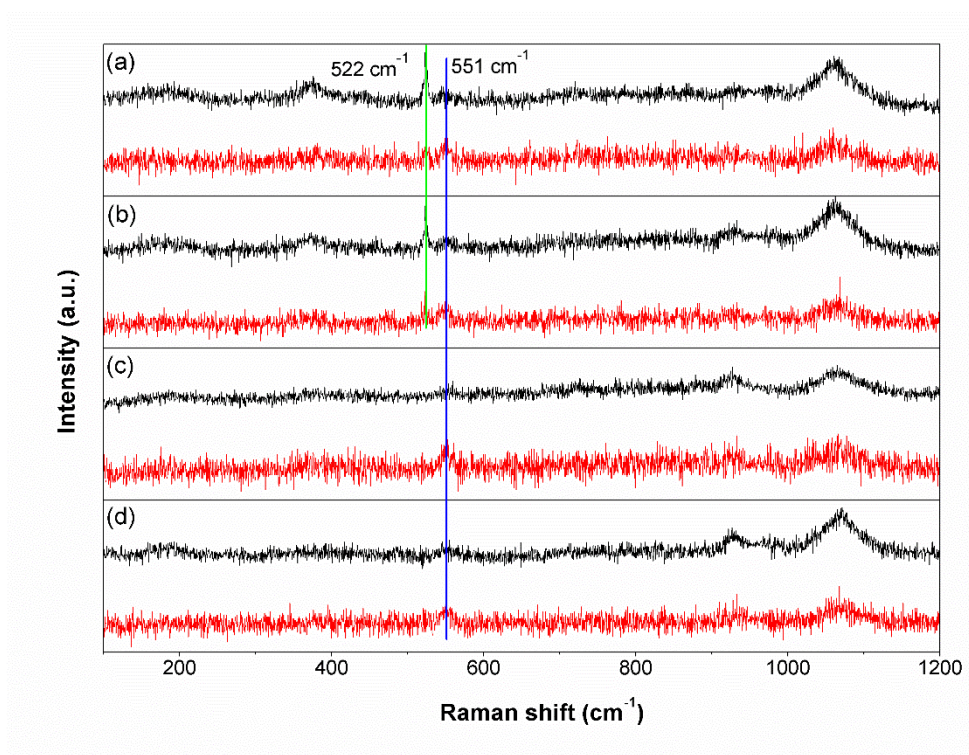


Figure 5.5: Raman spectra of individual nanowires on  $\text{Si}_x\text{N}_y$  substrate (a and b) and glass slide (c and d) taken at two different laser power:  $\sim 200\ \mu\text{W}$  (black) and  $\sim 20\ \mu\text{W}$  (red)

#### 5.3.4 Diameter Dependence

It has been shown that Raman intensity is dependent on diameter in Si nanowires with diameters ranging from 80 to 240 nm, in which the authors showed the

Raman intensity increases with decreasing diameter for a typical back scattering configuration.<sup>261</sup> However, such diameter dependence was absent in AlN nanowires<sup>262</sup> with diameters ranging from 33 to 4000 nm because of the relative small Bohr exciton radius of AlN, which makes quantum confinement not in effect. Here we selected several nanowires with different diameters and took each's Raman spectrum at the same conditions. As shown in Figure 5.6, the comparisons were categorized to two groups, TF and AF nanowires. In the TF nanowires group (Figure 5.6 (a)), it does show that the nanowire with larger diameter tends to exhibit weaker Raman scattering. However, there is no such trend in AF nanowires group (Figure 5.6 (b)). Therefore, the diameter dependence of Raman scattering in boron carbide nanowires is not consistent. In addition, the effect of fault density could also be simply evaluated from the data shown in Figure 5.6 (b), in which one nanowire has a fault density of 24%, while the other has a slightly higher one (28%). By looking at the Raman band at  $1060\text{ cm}^{-1}$ , it is found the one with higher fault density shifts toward lower frequency region and exhibits a broader band. It has been reported that high stacking fault density will broaden the Raman peak in some crystals (i.e. silicon carbides) due to the disorder in bond polarizability, which will then induce phonon modes with wave vectors away from the Brillouin zone center become Raman active.<sup>251</sup> Therefore, with examining the width of the Raman peak, we could roughly estimate the fault densities of boron carbide nanowires. However, by carefully examining the Raman spectra obtained from several nanowires on glass slide, one more interesting phenomenon was discovered. As can be seen Figure 5.7, all five nanowire exhibit similar Raman spectrum profiles. However,

the intensity ratio of the  $371\text{ cm}^{-1}$  to the  $189\text{ cm}^{-1}$  peak varies among the nanowire. Out of these five nanowires, NW 1 gives a ratio slightly larger than 1, while the rest four nanowires all have ratios less than 1, ranging from 0.87 to 0.97. Now the reason leading to this observation is unclear, but carbon concentration and position may play a role, and further structure investigations are needed.

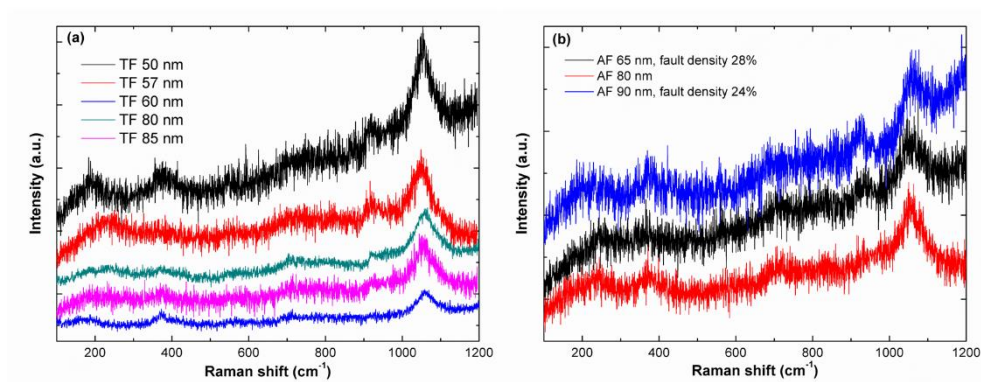


Figure 5.6: Raman spectra of individual nanowire with different diameters: TF group (a) and AF group (b).

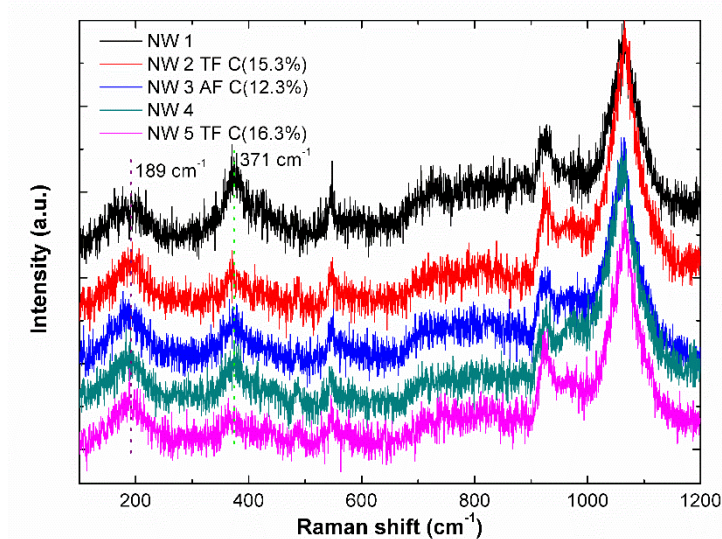


Figure 5.7: Raman spectra of five boron carbide nanowires suspended on the edge of thin glass slide.

### 5.3.5 Stacking Faults Orientations

Initially, it is thought that the stacking fault orientation will have significant effects on Raman scattering. If this is true, Raman spectroscopy will be a great tool to identify the boron carbide nanowires' stacking fault types. However, we discovered that stacking fault orientation actually does not impose significant effects on the Raman scattering. Figure 5.8 displays the Raman spectra of a TF and an AF nanowire, which looks almost identical. Another evidence could be traced back to Figure 5.5, in which two distinctive Raman spectra are observed in TF nanowires. Therefore, it is concluded that the Raman scattering is more related to carbon content other than stacking fault orientations.

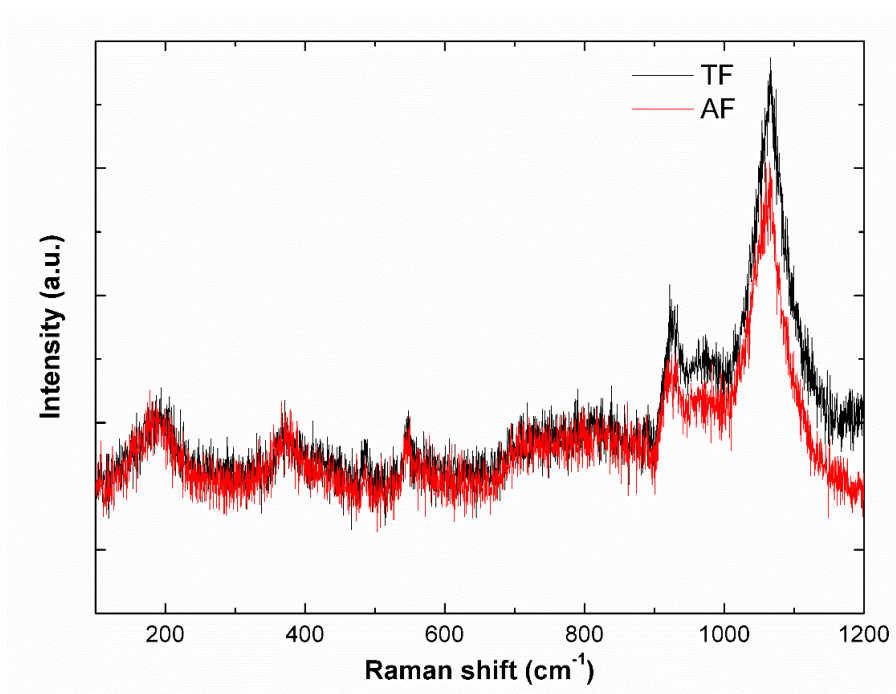


Figure 5.8: Comparison between Raman spectra obtained from a TF and an AF boron carbide nanowire.

#### 5.4 Conclusions

In this chapter, we have performed a preliminary Raman study of individual boron carbide nanowires. Because of the small Raman scattering cross section, the Raman scattering intensity of boron carbide nanowires is extremely weak. In order to acquire decent Raman spectra, the parameters, such as laser power, substrates, nanowires' positions, acquisition time and integration cycles must be optimized prior to the acquisition. The appropriate laser power was determined to be 230  $\mu\text{W}$  and 120  $\mu\text{W}$  for nanowires on glass slide and TEM grid respectively. It should be noted that some nanowires on TEM grid could sustain higher laser power as long as the exposure time is short. The acquisition time is set as 60 s to accumulate as many signals as possible during one cycle. As for the integration cycles, 10 cycles are typically used in our experiments.

In comparison to the Raman spectra from the bulk boron carbides, boron carbide nanowires' Raman spectra exhibit several distinctive features: diminishment of 480 $\text{cm}^{-1}$  and 531  $\text{cm}^{-1}$  double peaks, arising of 180  $\text{cm}^{-1}$  or 270  $\text{cm}^{-1}$  peak, and blue shifts of most Raman band, which are believed due to the quantum size confinement effects and high density of stacking faults. In addition, the effects of laser power, diameter, stacking fault densities and stacking faults orientations on Raman scattering in boron carbide nanowires were explored. It is interesting to find out that (1) the Raman peak at 551  $\text{cm}^{-1}$  becomes more intense at low laser power, (2) higher stacking fault densities actually could broaden the Raman bands, and (3) the intensity ratio of two Raman bands (i.e., the 371  $\text{cm}^{-1}$  to the 189  $\text{cm}^{-1}$  peak ) varies among the nanowires.

However, no solid or consistent diameter and stacking fault orientations dependence were discovered, which makes it impossible to employ Raman spectroscopy as an alternative tool to TEM to identify the stacking faults orientations in boron carbide nanowires. Nevertheless, Raman spectroscopy still could be used to tell the difference between a defective nanowire and defect-free nanowire, which has been confirmed in Si and Ge nanowires. We are not able to verify this finding as there is none defect-free boron carbide nanowires being identified in our as-synthesized nanowires. Though so, it will be worth looking into this issue in the future study.

## CHAPTER 6: CONCLUSIONS AND FUTURE WORKS

### 6.1 Conclusions

In this dissertation, aiming to correlate the structures with thermal properties and Raman scattering, we have systematically investigated the structure evolutions of kinked boron carbide nanowires via extensive TEM examinations and structure reconstruction modeling, performed thermal properties characterizations and analysis of tens of individual boron carbide nanowires including both straight and kinked ones (in collaboration with Dr. Li's group at Vanderbilt University), and also conducted micro-Raman studies on individual boron carbide nanowires. The following conclusions were obtained based on our studies.

For the kinked boron carbide nanowires, five kinking cases (TF-TF, AF-TF, AF-AF, TF-IF and AF-IF kink) are discovered based on the combination of the stacking faults orientations. In addition, the characteristic features and kink angles of kinked boron carbide nanowire viewed from different zone axes were explored and summarized to assist in differentiating the nanowires. The catalysts' instability and migration are believed to be responsible for kinking during the VLS growth of boron carbide nanowires.

The thermal properties and structure relation of boron carbide nanowires has been established. The thermal conductivities of boron carbide nanowires exhibit strong

carbon content and diameter dependence. Larger diameter nanowires of higher carbon concentration typically have higher thermal conductivities. In addition, TF nanowires generally have ~20% lower thermal conductivities than the AF ones. The fault density only seems to affect the phonon transport when it is beyond a threshold (~39%). The most important finding is the significant reduction of thermal conductivities of kinked nanowires, which may be due to the need for phonon mode conversion or scattering before they can propagate into the other side of the kink.

On the hand, micro-Raman spectroscopy could be used to distinguish the stacking faults densities instead of the orientations. Higher stacking fault densities broaden the Raman bands. In addition, carbon content plays an extremely important role in Raman scattering, especially in the low frequency region ( $< 600 \text{ cm}^{-1}$ ), which arises from the vibrations of three-atom chains.

## 6.2 Future Works

For the structural study of boron carbide nanowires, though we have proposed several general growth mechanisms of kinking in boron carbide nanowires based on the catalysts' instability and migration, more works need to be done in order to clarify this hypothesis. For example, the phases, interface and the decomposition, diffusion and migration routes of the catalysts should be carefully investigated, which might shine insights on the rational synthesis of kinked boron carbide nanowires.

For thermal properties study of boron carbide nanowires, we have focused on the thermal conductivities measurement within 20-420 K. Since boron carbide nanowires are potential high temperature TE materials, the measurement should be

extended to a higher temperature (800K). In addition, in order to evaluate the thermoelectric performance of the boron carbide nanowires, electrical conductivities and Seebeck coefficients should be measured as well. The preliminary results indicate the figure of merit of boron carbide nanowires is still relatively low due to the small electrical conductivity. Therefore, our next approach is to find the nanowires (*e.g.* kinked nanowires with multiple kinks) with even smaller thermal conductivities or to dope the current nanowires with Al or other metals to enhance the electrical conductivities.

For micro-Raman study of boron carbide nanowires, a more systematic investigation of the carbon concentration's effect on Raman scattering is necessary. This will give hints on the carbon position within the boron carbide unit cell. In addition, the parameters should be further optimized to obtain better quality Raman spectra of boron carbide nanowires since the current ones contain much noises. For example, the nanowires could be placed directly on an Au-coated silicon or glass substrate.

## REFERENCES

1. Administration, U. S. E. I. Annual Energy Outlook 2016. (2016).
2. Kanatzidis, M. G. Nanostructured Thermoelectrics: The New Paradigm? *Chemistry of Materials* **22**, 648-659, doi:10.1021/cm902195j (2010).
3. DiSalvo, F. J. Thermoelectric Cooling and Power Generation. *Science* **285**, 703-706, doi:10.1126/science.285.5428.703 (1999).
4. Haidar, J. G. & Ghojel, J. I. in *Thermoelectrics, 2001. Proceedings ICT 2001. XX International Conference on.* 413-418.
5. Ghoshal, U. *et al.* Enhanced thermoelectric cooling at cold junction interfaces. *Applied Physics Letters* **80**, 3006-3008, doi:doi:http://dx.doi.org/10.1063/1.1473233 (2002).
6. Bell, L. E. Cooling, Heating, Generating Power, and Recovering Waste Heat with Thermoelectric Systems. *Science* **321**, 1457-1461, doi:10.1126/science.1158899 (2008).
7. Fradkin, G. M. & Kodyukov, V. M. Radioisotope thermoelectric generators. *Soviet Atomic Energy* **26**, 193-198, doi:10.1007/bf01119495 (1969).
8. Bennett, G. L. & Skrabek, E. A. in *Thermoelectrics, 1996., Fifteenth International Conference on.* 357-372.
9. Rowe, D. M. Applications of nuclear-powered thermoelectric generators in space. *Applied Energy* **40**, 241-271, doi:http://dx.doi.org/10.1016/0306-2619(91)90020-X (1991).
10. Gelbstein, Y., Dashevsky, Z. & Dariel, M. P. High performance n-type PbTe-based materials for thermoelectric applications. *Physica B: Condensed Matter* **363**, 196-205, doi:http://dx.doi.org/10.1016/j.physb.2005.03.022 (2005).
11. Sootsman, J. R. *et al.* Large Enhancements in the Thermoelectric Power Factor of Bulk PbTe at High Temperature by Synergistic Nanostructuring. *Angewandte Chemie* **120**, 8746-8750, doi:10.1002/ange.200803934 (2008).
12. Pei, Y., Lensch-Falk, J., Toberer, E. S., Medlin, D. L. & Snyder, G. J. High Thermoelectric Performance in PbTe Due to Large Nanoscale Ag<sub>2</sub>Te

- Precipitates and La Doping. *Advanced Functional Materials* **21**, 241-249, doi:10.1002/adfm.201000878 (2011).
13. Wright, D. A. Thermoelectric Properties of Bismuth Telluride and its Alloys. *Nature* **181**, 834-834 (1958).
  14. Goldsmid, H. J. & Douglas, R. W. The use of semiconductors in thermoelectric refrigeration. *British Journal of Applied Physics* **5**, 386 (1954).
  15. Goldsmid, H. J., Giutronich, J. E. & Kaila, M. M. Solar thermoelectric generation using bismuth telluride alloys. *Solar Energy* **24**, 435-440, doi:http://dx.doi.org/10.1016/0038-092X(80)90311-4 (1980).
  16. Yamashita, O., Tomiyoshi, S. & Makita, K. Bismuth telluride compounds with high thermoelectric figures of merit. *Journal of Applied Physics* **93**, 368-374, doi:doi:http://dx.doi.org/10.1063/1.1525400 (2003).
  17. Takahashi, M. *et al.* Electric and thermoelectric properties of electrodeposited bismuth telluride (Bi<sub>2</sub>Te<sub>3</sub>) films. *Journal of Applied Physics* **96**, 5582-5587, doi:doi:http://dx.doi.org/10.1063/1.1785834 (2004).
  18. Harman, T. C., Taylor, P. J., Walsh, M. P. & LaForge, B. E. Quantum Dot Superlattice Thermoelectric Materials and Devices. *Science* **297**, 2229-2232, doi:10.1126/science.1072886 (2002).
  19. Wang, H., Pei, Y., LaLonde, A. D. & Snyder, G. J. Heavily Doped p-Type PbSe with High Thermoelectric Performance: An Alternative for PbTe. *Advanced Materials* **23**, 1366-1370, doi:10.1002/adma.201004200 (2011).
  20. Seebeck, T. J. Ueber die magnetische Polarisierung der Metalle und Erze durch Temperatur-Differenz. *Annalen der Physik* **82**, 133-160, doi:10.1002/andp.18260820202 (1826).
  21. Goldsmid, H. J. *Springer Series in Materials Science* 228 (Springer-Verlag Berlin Heidelberg, 2010).
  22. Snyder, G. J. Small Thermoelectric Generators. *The Electrochemical Society Interface*, 54-56 (2008).
  23. Zebarjadi, M., Esfarjani, K., Dresselhaus, M. S., Ren, Z. F. & Chen, G. Perspectives on thermoelectrics: from fundamentals to device applications.

- Energy & Environmental Science* **5**, 5147-5162, doi:10.1039/C1EE02497C (2012).
24. Thomson, W. On the Dynamical Theory of Heat. *Transactions of the Royal Society of Edinburgh* **3**, 91-98 (1851).
  25. Naslain, R. in *Boron and Refractory Borides* (ed V.I. Matkovich, Samsonov, G.V., Hagenmuller, P., Lundstrom, T. ) 140-141 (Springer-Verlag Berlin Heidelberg, 1977).
  26. Emin, D. Unusual properties of icosahedral boron-rich solids. *J Solid State Chem* **179**, 2791-2798, doi:10.1016/j.jssc.2006.01.014 (2006).
  27. Decker, B. F. & Kasper, J. S. The crystal structure of a simple rhombohedral form of boron. *Acta Crystallographica* **12**, 503-506, doi:doi:10.1107/S0365110X59001529 (1959).
  28. Domnich, V., Reynaud, S., Haber, R. A. & Chhowalla, M. Boron Carbide: Structure, Properties, and Stability under Stress. *Journal of the American Ceramic Society* **94**, 3605-3628, doi:10.1111/j.1551-2916.2011.04865.x (2011).
  29. Bouchacourt, M. & Thevenot, F. The melting of boron carbide and the homogeneity range of the boron carbide phase. *Journal of the Less Common Metals* **67**, 327-331, doi:http://dx.doi.org/10.1016/0022-5088(79)90007-9 (1979).
  30. Bouchacourt, M., Thevenot, F. & Ruste, J. Études sur le carbure de bore iii. domaine d'existence de la phase carbure de bore. *Journal of the Less Common Metals* **59**, 139-152, doi:http://dx.doi.org/10.1016/0022-5088(78)90126-1 (1978).
  31. Beauvy, M. Stoichiometric limits of carbon-rich boron carbide phases. *Journal of the Less Common Metals* **90**, 169-175, doi:http://dx.doi.org/10.1016/0022-5088(83)90067-X (1983).
  32. Anwar, H., Murli, H. M., Helmut, W., Przemyslaw, D. & Quentin, W. High-pressure phase transition makes B<sub>4.3</sub>C boron carbide a wide-gap semiconductor. *Journal of Physics: Condensed Matter* **28**, 045403 (2016).
  33. Tallant, D. R., Aselage, T. L., Campbell, A. N. & Emin, D. Boron carbide structure by Raman spectroscopy. *Physical Review B* **40**, 5649-5656, doi:10.1103/PhysRevB.40.5649 (1989).

34. McIlroy, D. N. *et al.* Electronic and dynamic studies of boron carbide nanowires. *Physical Review B* **60**, 4874-4879 (1999).
35. A. J. Silvestre, M. J. G. S., O. Conde. The Role of Carbon Precursor on Boron Carbide Synthesis by Laser-CVD. *Key Engineering Materials* **230-232**, 4 (2002).
36. Werheit, H., Leithe-Jasper, A., Tanaka, T., Rotter, H. W. & Schwetz, K. A. Some properties of single-crystal boron carbide. *J Solid State Chem* **177**, 575-579, doi:10.1016/j.jssc.2003.04.005 (2004).
37. Balakrishnarajan, M. M., Pancharatna, P. D. & Hoffmann, R. Structure and bonding in boron carbide: The invincibility of imperfections. *New Journal of Chemistry* **31**, 473, doi:10.1039/b618493f (2007).
38. An, Q., Goddard, W. A. & Cheng, T. Atomistic Explanation of Shear-Induced Amorphous Band Formation in Boron Carbide. *Phys Rev Lett* **113**, 095501 (2014).
39. Wood, C. & Emin, D. Conduction mechanism in boron carbide. *Physical Review B* **29**, 4582-4587, doi:10.1103/PhysRevB.29.4582 (1984).
40. Bouchacourt, M. & Thevenot, F. The correlation between the thermoelectric properties and stoichiometry in the boron carbide phase B<sub>4</sub>C-B<sub>10.5</sub>C. *Journal of Materials Science* **20**, 1237-1247, doi:10.1007/BF01026319 (1985).
41. Medwick, P. A., Fischer, H. E. & Pohl, R. O. Thermal conductivity and specific heat of boron carbides. *Journal of Alloys and Compounds* **203**, 67-75, doi:http://dx.doi.org/10.1016/0925-8388(94)90716-1 (1994).
42. Moss, M. Thermal Conductivity of Boron Carbides. *MRS Online Proceedings Library* **97**, null-null, doi:doi:10.1557/PROC-97-77 (1987).
43. Aselage, T. L. High Temperature Thermoelectric Properties of Boron Carbide. *MRS Online Proceedings Library* **234**, null-null, doi:doi:10.1557/PROC-234-145 (1991).
44. Cai, K.-F., Nan, C.-W. & Min, X.-M. The Influence of Silicon Dopant and Processing on Thermoelectric Properties of B<sub>4</sub>C Ceramics. *MRS Online Proceedings Library* **545**, null-null, doi:doi:10.1557/PROC-545-131 (1998).

45. Cai, K.-f., Nan, C.-W. & Min, X.-m. The effect of silicon addition on thermoelectric properties of a B<sub>4</sub>C ceramic. *Materials Science and Engineering: B* **67**, 102-107, doi:[http://dx.doi.org/10.1016/S0921-5107\(99\)00220-2](http://dx.doi.org/10.1016/S0921-5107(99)00220-2) (1999).
46. Ghamaty, S., Elsner, N., Wang, K. & Xiang, Q. in *Thermoelectrics, 1996., Fifteenth International Conference on.* 469-473.
47. Xinmin, M., Cewen, N. & Kefeng, C. Structural Characteristics and Quantum Chemistry Calculation of Si-Doped Boron Carbides. *MRS Online Proceedings Library* **538**, null-null, doi:[doi:10.1557/PROC-538-579](http://dx.doi.org/10.1557/PROC-538-579) (1998).
48. Lee, S., Mazurowski, J., Ramseyer, G. & Dowben, P. A. Characterization of boron carbide thin films fabricated by plasma enhanced chemical vapor deposition from boranes. *Journal of Applied Physics* **72**, 4925, doi:[10.1063/1.352060](http://dx.doi.org/10.1063/1.352060) (1992).
49. Werheit, H. in *Thermoelectrics, 2006. ICT '06. 25th International Conference on.* 159-163.
50. Gunjishima, I., Akashi, T. & Goto, T. Thermoelectric Properties of Single Crystalline B<sub>4</sub>C Prepared by a Floating Zone Method. *Materials Transactions, JIM* **42**, 1445-1450, doi:[10.2320/matertrans.42.1445](http://dx.doi.org/10.2320/matertrans.42.1445) (2001).
51. Aoqui, S.-i., Miyata, H., Ohshima, T., Ikegami, T. & Ebihara, K. Preparation of boron carbide thin film by pulsed KrF excimer laser deposition process. *Thin Solid Films* **407**, 126-131, doi:[http://dx.doi.org/10.1016/S0040-6090\(02\)00025-1](http://dx.doi.org/10.1016/S0040-6090(02)00025-1) (2002).
52. Suematsu, H. *et al.* in *Surface Engineering* 199-206 (John Wiley & Sons, Inc., 2002).
53. Sasaki, S. *et al.* Thermoelectric properties of boron-carbide thin film and thin film based thermoelectric device fabricated by intense-pulsed ion beam evaporation. *Science and Technology of Advanced Materials* **6**, 181-184, doi:[10.1016/j.stam.2004.11.010](http://dx.doi.org/10.1016/j.stam.2004.11.010) (2005).
54. Chen, Z.-G., Han, G., Yang, L., Cheng, L. & Zou, J. Nanostructured thermoelectric materials: Current research and future challenge. *Progress in Natural Science: Materials International* **22**, 535-549, doi:<http://dx.doi.org/10.1016/j.pnsc.2012.11.011> (2012).

55. Snyder, G. J. & Toberer, E. S. Complex thermoelectric materials. *Nat Mater* **7**, 105-114 (2008).
56. Tian, Z., Lee, S. & Chen, G. A Comprehensive Review of Heat Transfer in Thermoelectric Materials and Devices. *ArXiv e-prints* **1401** (2014). <<http://adsabs.harvard.edu/abs/2014arXiv1401.0749T>>.
57. Madarasz, F. L. & Klemens, P. G. Reduction of lattice thermal conductivity by point defects at intermediate temperatures. *International Journal of Thermophysics* **8**, 257-262, doi:10.1007/bf00515208 (1987).
58. Prytz, O., Flage-Larsen, E., Toberer, E. S., Snyder, G. J. & Taftø, J. Reduction of lattice thermal conductivity from planar faults in the layered Zintl compound SrZnSb<sub>2</sub>. *Journal of Applied Physics* **109**, 043509, doi:10.1063/1.3549821 (2011).
59. Balandin, A. & Wang, K. L. Significant decrease of the lattice thermal conductivity due to phonon confinement in a free-standing semiconductor quantum well. *Physical Review B* **58**, 1544-1549 (1998).
60. Takemoto, H. *et al.* Reduction of thermal conductivity in dually doped ZnO by design of three-dimensional stacking faults. *RSC Advances* **4**, 2661-2672, doi:10.1039/C3RA44223C (2014).
61. Nissimagoudar, A. S. & Sankeshwar, N. S. Significant reduction of lattice thermal conductivity due to phonon confinement in graphene nanoribbons. *Physical Review B* **89**, 235422 (2014).
62. Rowe, D. M. *CRC Handbook of Thermoelectrics*. (CRC Press, 1995).
63. Rowe, D. W. *Thermoelectrics Handbook: Macro to Nano*. (CRC Press, 2006).
64. Slack, G. A. in *CRC Handbook of Thermoelectrics* (ed D.W. Rowe) 407-440 (CRC Press, 1995).
65. Sales, B. C., Mandrus, D. & Williams, R. K. Filled Skutterudite Antimonides: A New Class of Thermoelectric Materials. *Science* **272**, 1325-1328, doi:10.1126/science.272.5266.1325 (1996).
66. Nolas, G. S., Cohn, J. L., Slack, G. A. & Schujman, S. B. Semiconducting Ge clathrates: Promising candidates for thermoelectric applications. *Applied Physics Letters* **73**, 178-180, doi:doi:<http://dx.doi.org/10.1063/1.121747> (1998).

67. Nolas, G. S., Morelli, D. T. & Tritt, T. M. SKUTTERUDITES: A Phonon-Glass-Electron Crystal Approach to Advanced Thermoelectric Energy Conversion Applications. *Annual Review of Materials Science* **29**, 89-116, doi:doi:10.1146/annurev.matsci.29.1.89 (1999).
68. Takabatake, T., Suekuni, K., Nakayama, T. & Kaneshita, E. Phonon-glass electron-crystal thermoelectric clathrates: Experiments and theory. *Reviews of Modern Physics* **86**, 669-716 (2014).
69. Tritt, T. M. Thermoelectric Phenomena, Materials, and Applications. *Annual Review of Materials Research* **41**, 433-448, doi:doi:10.1146/annurev-matsci-062910-100453 (2011).
70. Barabash, S. V., Ozolins, V. & Wolverton, C. First-principles theory of the coherency strain, defect energetics, and solvus boundaries in the PbTe-AgSbTe<sub>2</sub> system. *Physical Review B* **78**, 214109 (2008).
71. Barabash, S. V., Ozolins, V. & Wolverton, C. First-Principles Theory of Competing Order Types, Phase Separation, and Phonon Spectra in Thermoelectric AgPb<sub>m</sub>SbTe<sub>m+2</sub> Alloys. *Phys Rev Lett* **101**, 155704 (2008).
72. Hsu, K. F. *et al.* Cubic AgPb<sub>m</sub>SbTe<sub>2+m</sub>: Bulk Thermoelectric Materials with High Figure of Merit. *Science* **303**, 818-821, doi:10.1126/science.1092963 (2004).
73. Zhou, M., Li, J.-F. & Kita, T. Nanostructured AgPb<sub>m</sub>SbTe<sub>m+2</sub> System Bulk Materials with Enhanced Thermoelectric Performance. *Journal of the American Chemical Society* **130**, 4527-4532, doi:10.1021/ja7110652 (2008).
74. Androulakis, J. *et al.* Nanostructuring and High Thermoelectric Efficiency in p-Type Ag(Pb<sub>1-y</sub>Sn<sub>y</sub>)mSbTe<sub>2+m</sub>. *Advanced Materials* **18**, 1170-1173, doi:10.1002/adma.200502770 (2006).
75. Poudeu, P. F. *et al.* High thermoelectric figure of merit and nanostructuring in bulk p-type Na<sub>1-x</sub>Pb<sub>m</sub>Sb<sub>y</sub>Te<sub>m+2</sub>. *Angew Chem Int Ed Engl* **45**, 3835-3839, doi:10.1002/anie.200600865 (2006).
76. Guéguen, A. *et al.* Thermoelectric Properties and Nanostructuring in the p-Type Materials NaPb<sub>18-x</sub>Sn<sub>x</sub>MTe<sub>20</sub> (M = Sb, Bi). *Chemistry of Materials* **21**, 1683-1694, doi:10.1021/cm803519p (2009).

77. Poudeu, P. F. P., Guéguen, A., Wu, C.-I., Hogan, T. & Kanatzidis, M. G. High Figure of Merit in Nanostructured n-Type  $\text{KPb}_m\text{SbTe}_{m+2}$  Thermoelectric Materials. *Chemistry of Materials* **22**, 1046-1053, doi:10.1021/cm902001c (2010).
78. Li, J.-F., Liu, W.-S., Zhao, L.-D. & Zhou, M. High-performance nanostructured thermoelectric materials. *NPG Asia Mater* **2**, 152-158 (2010).
79. Venkatasubramanian, R., Siivola, E., Colpitts, T. & O'Quinn, B. Thin-film thermoelectric devices with high room-temperature figures of merit. *Nature* **413**, 597-602 (2001).
80. Kittel, C. *Elementary Solid State Physics*. (John Wiley & Sons., Inc., 1962).
81. Yu, J.-k. *Nanostructured silicon thermoelectrics* Ph.D. thesis, California Institute of Technology, (2012).
82. Weber, L. & Gmelin, E. Transport properties of silicon. *Applied Physics A* **53**, 136-140, doi:10.1007/bf00323873 (1991).
83. Bo, Q. *et al.* First-principles simulation of electron mean-free-path spectra and thermoelectric properties in silicon. *EPL (Europhysics Letters)* **109**, 57006 (2015).
84. Li, D. *et al.* Thermal conductivity of individual silicon nanowires. *Applied Physics Letters* **83**, 2934-2936, doi:doi:http://dx.doi.org/10.1063/1.1616981 (2003).
85. Hochbaum, A. I. *et al.* Enhanced thermoelectric performance of rough silicon nanowires. *Nature* **451**, 163-167, doi:http://www.nature.com/nature/journal/v451/n7175/supinfo/nature06381\_S1.html (2008).
86. Boukai, A. I. *et al.* Silicon nanowires as efficient thermoelectric materials. *Nature* **451**, 168-171, doi:http://www.nature.com/nature/journal/v451/n7175/supinfo/nature06458\_S1.html (2008).
87. Davoody, A. H., Ramayya, E. B., Maurer, L. N. & Knezevic, I. Ultrathin GaN nanowires: Electronic, thermal, and thermoelectric properties. *Physical Review B* **89**, 115313 (2014).

88. Wang, K., Liang, H.-W., Yao, W.-T. & Yu, S.-H. Templating synthesis of uniform Bi<sub>2</sub>Te<sub>3</sub> nanowires with high aspect ratio in triethylene glycol (TEG) and their thermoelectric performance. *J Mater Chem* **21**, 15057-15062, doi:10.1039/C1JM12384J (2011).
89. Yazji, S. *et al.* Complete thermoelectric benchmarking of individual InSb nanowires using combined micro-Raman and electric transport analysis. *Nano Research* **8**, 4048-4060, doi:10.1007/s12274-015-0906-8 (2015).
90. Zhou, F. *et al.* One-dimensional electron transport and thermopower in an individual InSb nanowire. *Journal of Physics: Condensed Matter* **18**, 9651 (2006).
91. Wu, P. M. *et al.* Large Thermoelectric Power Factor Enhancement Observed in InAs Nanowires. *Nano letters* **13**, 4080-4086, doi:10.1021/nl401501j (2013).
92. Karg, S. F. *et al.* Full thermoelectric characterization of InAs nanowires using MEMS heater/sensors. *Nanotechnology* **25**, 305702 (2014).
93. Kim, J., Shim, W. & Lee, W. Bismuth nanowire thermoelectrics. *Journal of Materials Chemistry C* **3**, 11999-12013, doi:10.1039/C5TC02886H (2015).
94. Jiang, J.-W., Yang, N., Wang, B.-S. & Rabczuk, T. Modulation of Thermal Conductivity in Kinked Silicon Nanowires: Phonon Interchanging and Pinching Effects. *Nano letters* **13**, 1670-1674, doi:10.1021/nl400127q (2013).
95. Wang, B., Zhou, J., Yang, R. & Li, B. Ballistic thermoelectric transport in structured nanowires. *New Journal of Physics* **16**, 065018, doi:10.1088/1367-2630/16/6/065018 (2014).
96. Hicks, L. D. & Dresselhaus, M. S. Effect of quantum-well structures on the thermoelectric figure of merit. *Physical Review B* **47**, 12727-12731 (1993).
97. Hicks, L. D., Harman, T. C. & Dresselhaus, M. S. Use of quantum - well superlattices to obtain a high figure of merit from nonconventional thermoelectric materials. *Applied Physics Letters* **63**, 3230-3232, doi:doi:http://dx.doi.org/10.1063/1.110207 (1993).
98. Hicks, L. D., Harman, T. C., Sun, X. & Dresselhaus, M. S. Experimental study of the effect of quantum-well structures on the thermoelectric figure of merit. *Physical Review B* **53**, R10493-R10496 (1996).

99. Hicks, L. D. & Dresselhaus, M. S. Thermoelectric figure of merit of a one-dimensional conductor. *Physical Review B* **47**, 16631-16634 (1993).
100. Mingo, N. Thermoelectric figure of merit and maximum power factor in III–V semiconductor nanowires. *Applied Physics Letters* **84**, 2652, doi:10.1063/1.1695629 (2004).
101. Dresselhaus, M. S. Bismuth nanowires for thermoelectric applications. *Microscale Thermophysical Engineering* **7**, 207-219, doi:10.1080/10893950390219056 (2003).
102. Kirihaara, K., Sasaki, T., Koshizaki, N. & Kimura, K. Seebeck Coefficient and Power Factor of Single-Crystalline Boron Nanobelts. *Applied Physics Express* **4**, 041201, doi:10.1143/apex.4.041201 (2011).
103. Guan, Z. *et al.* Boron carbide nanowires: low temperature synthesis and structural and thermal conductivity characterization. *J Mater Chem* **22**, 9853, doi:10.1039/c2jm14857a (2012).
104. Emin, D. Icosahedral Boron-Rich Solids as Refractory Semiconductors. *MRS Online Proceedings Library* **97**, null-null, doi:doi:10.1557/PROC-97-3 (1987).
105. Tian, J. *et al.* Boron nanowires for flexible electronics. *Applied Physics Letters* **93**, 122105, doi:10.1063/1.2976668 (2008).
106. Ding, W., Calabri, L., Chen, X., Kohlhaas, K. M. & Ruoff, R. S. Mechanics of crystalline boron nanowires. *Composites Science and Technology* **66**, 1112-1124, doi:10.1016/j.compscitech.2005.11.030 (2006).
107. Otten, C. J. *et al.* Crystalline Boron Nanowires. *Journal of the American Chemical Society* **124**, 4564-4565, doi:10.1021/ja017817s (2002).
108. Wang, Z. *et al.* Catalyst-free fabrication of single crystalline boron nanobelts by laser ablation. *Chemical Physics Letters* **368**, 663-667, doi:http://dx.doi.org/10.1016/S0009-2614(02)01964-4 (2003).
109. Xu, T. T. *et al.* Crystalline Boron Nanoribbons: Synthesis and Characterization. *Nano letters* **4**, 963-968, doi:10.1021/nl0498785 (2004).
110. Xu, T. T. *et al.* Single-Crystal Calcium Hexaboride Nanowires: Synthesis and Characterization. *Nano letters* **4**, 2051-2055, doi:10.1021/nl0486620 (2004).

111. Amin, S. S., Li, S.-y., Roth, J. R. & Xu, T. T. Single Crystalline Alkaline-Earth Metal Hexaboride One-Dimensional (1D) Nanostructures: Synthesis and Characterization. *Chem Mater* **21**, 763-770, doi:10.1021/cm802018e (2009).
112. Brewer, J. R., Jacobberger, R. M., Diercks, D. R. & Cheung, C. L. Rare Earth Hexaboride Nanowires: General Synthetic Design and Analysis Using Atom Probe Tomography. *Chemistry of Materials* **23**, 2606-2610, doi:10.1021/cm200258h (2011).
113. Frye, C. D. *et al.* Synthesis of Icosahedral Boron Arsenide Nanowires for Betavoltaic Applications. *MRS Online Proceedings Library* **1439**, 69-75, doi:doi:10.1557/opl.2012.1156 (2012).
114. Ma, R. & Bando, Y. High purity single crystalline boron carbide nanowires. *Chemical Physics Letters* **364**, 314-317, doi:http://dx.doi.org/10.1016/S0009-2614(02)01312-X (2002).
115. Ma, R. & Bando, Y. Investigation on the Growth of Boron Carbide Nanowires. *Chemistry of Materials* **14**, 4403-4407, doi:10.1021/cm020630v (2002).
116. Zhang, H. Z. *et al.* Boron carbide nanowires with uniform CN<sub>x</sub> coatings. *New Journal of Physics* **9**, 13-13, doi:10.1088/1367-2630/9/1/013 (2007).
117. Huang, Y. *et al.* Fabrication of patterned boron carbide nanowires and their electrical, field emission, and flexibility properties. *Nano Research* **5**, 896-902, doi:10.1007/s12274-012-0273-7 (2012).
118. Wei, J. *et al.* Straight boron carbide nanorods prepared from carbon nanotubes. *J Mater Chem* **12**, 3121-3124, doi:10.1039/b204792f (2002).
119. Cao, M., Jiang, J., Liu, H. & Yuan, J. A simple method to prepare boron suboxide fibres. *Journal of Electroceramics* **17**, 817-820, doi:10.1007/s10832-006-0457-1 (2006).
120. Yang, J. *et al.* Enhanced and switchable nanoscale thermal conduction due to van der Waals interfaces. *Nat Nano* **7**, 91-95, doi:http://www.nature.com/nnano/journal/v7/n2/abs/nnano.2011.216.html#supplementary-information (2012).
121. Patel, R. B., Chou, T. & Iqbal, Z. Synthesis of Boron Nanowires, Nanotubes, and Nanosheets. *Journal of Nanomaterials* **2015**, 7, doi:10.1155/2015/243925 (2015).

122. Jazirehpour, M., Bahahrvandi, H. R., Alizadeh, A. & Ehsani, N. Facile synthesis of boron carbide elongated nanostructures via a simple in situ thermal evaporation process. *Ceram Int* **37**, 1055-1061, doi:DOI 10.1016/j.ceramint.2010.11.028 (2011).
123. Xu, J., Chang, Y., Gan, L., Ma, Y. & Zhai, T. Ultrathin Single-Crystalline Boron Nanosheets for Enhanced Electro-Optical Performances. *Advanced Science* **2**, n/a-n/a, doi:10.1002/advs.201500023 (2015).
124. Nersisyan, H. H. *et al.* Polymer assisted approach to two-dimensional (2D) nanosheets of B<sub>4</sub>C. *Chemical Engineering Journal* **281**, 218-226, doi:10.1016/j.cej.2015.06.100 (2015).
125. Chen, S., Wang, D. Z., Huang, J. Y. & Ren, Z. F. Synthesis and characterization of boron carbide nanoparticles. *Applied Physics A* **79**, doi:10.1007/s00339-004-2913-6 (2004).
126. Chang, B., Gersten, B. L., Szewczyk, S. T. & Adams, J. W. Characterization of boron carbide nanoparticles prepared by a solid state thermal reaction. *Applied Physics A* **86**, 83-87, doi:10.1007/s00339-006-3729-3 (2006).
127. Shin, W. G., Calder, S., Ugurlu, O. & Girshick, S. L. Production and characterization of boron nanoparticles synthesized with a thermal plasma system. *Journal of Nanoparticle Research* **13**, 7187-7191, doi:10.1007/s11051-011-0633-3 (2011).
128. Guan, Z. *et al.* Observation of 'hidden' planar defects in boron carbide nanowires and identification of their orientations. *Nanoscale Research Letters* **9**, 1-9, doi:10.1186/1556-276X-9-30 (2014).
129. Wagner, R. S. & Ellis, W. C. Vapor - Liquid - Solid Mechanism Of Single Crystal Growth. *Applied Physics Letters* **4**, 89-90, doi:doi:http://dx.doi.org/10.1063/1.1753975 (1964).
130. Doherty, R. S. W. a. C. J. Controlled Vapor - Liquid - Solid Growth of Silicon Crystals.pdf. *Journal of the Electrochemical Society* **113**, 1300-1304 (1966).
131. Schmidt, V., Wittemann, J. V. & Gösele, U. Growth, Thermodynamics, and Electrical Properties of Silicon Nanowires. *Chemical Reviews* **110**, 361-388, doi:10.1021/cr900141g (2010).

132. Seth, A. F. & Xiuling, L. Metal-catalyzed semiconductor nanowires: a review on the control of growth directions. *Semiconductor Science and Technology* **25**, 024005 (2010).
133. Lauhon, L. J., Gudiksen, M. S., Wang, D. & Lieber, C. M. Epitaxial core-shell and core-multishell nanowire heterostructures. *Nature* **420**, 57-61, doi:http://www.nature.com/nature/journal/v420/n6911/suppinfo/nature01141\_S1.html (2002).
134. Kempa, T. J. *et al.* Single and Tandem Axial p-i-n Nanowire Photovoltaic Devices. *Nano letters* **8**, 3456-3460, doi:10.1021/nl8023438 (2008).
135. Wagner, R. S. & Ooherty, C. J. Mechanism of Branching and Kinking during VLS Crystal Growth. *Journal of The Electrochemical Society* **115**, 93-99, doi:10.1149/1.2411032 (1968).
136. J. Westwater, D. P. G., S. Tomiya, S. Usui, and H. Ruda. Growth of silicon nanowires via goldsilane vapor-liquid-solid reaction.pdf. *J Vac Sci Technol B* **15**, 554-557, doi:10.1116/1.589291 (1997).
137. Geaney, H. *et al.* Role of Defects and Growth Directions in the Formation of Periodically Twinned and Kinked Unseeded Germanium Nanowires. *Crystal Growth & Design* **11**, 3266-3272, doi:10.1021/cg200510y (2011).
138. Jeon, N., Dayeh, S. A. & Lauhon, L. J. Origin of Polytype Formation in VLS-Grown Ge Nanowires through Defect Generation and Nanowire Kinking. *Nano letters* **13**, 3947-3952 (2013).
139. Musin, I. R. & Filler, M. A. Chemical Control of Semiconductor Nanowire Kinking and Superstructure. *Nano letters* **12**, 3363-3368, doi:10.1021/nl204065p (2012).
140. W.S. Shi, Y. F. Z., N. Wang, C.S. Lee and S.T. Lee. Synthesis and microstructure of gallium phosphide nanowires.pdf. *J Vac Sci Technol B* **19**, 1115-1118, doi:10.1116/1.1382871 (2001).
141. Wang, J. *et al.* Reversible Switching of InP Nanowire Growth Direction by Catalyst Engineering. *Nano letters* **13**, 3802-3806, doi:10.1021/nl401767b (2013).

142. Minghuan Zhang, F. W., Chao Wang, Yiqian Wang, SenPo Yip and Johnny C Ho. Formation mechanisms for the dominant kinks with different angles in InP nanowires. *Nanoscale Research Letters* **9**, 211 (2014).
143. Yan, X., Zhang, X., Li, J., Wu, Y. & Ren, X. Self-catalyzed growth of pure zinc blende  $\langle 110 \rangle$  InP nanowires. *Applied Physics Letters* **107**, 023101, doi:10.1063/1.4926728 (2015).
144. Lenrick, F., Ek, M., Deppert, K., Samuelson, L. & Reine Wallenberg, L. Straight and kinked InAs nanowire growth observed in situ by transmission electron microscopy. *Nano Research* **7**, 1188-1194, doi:10.1007/s12274-014-0481-4 (2014).
145. Z.H. Wu, X. M., D. Kim, M. Blumin, H.E. Ruda, J.Q. Liu, and K.L. Kavanagh. <2003-Growth, branching, and kinking of molecular-beam epitaxial  $\langle 110 \rangle$  GaAs nanowires.pdf>. *Applied Physics Letters* **83**, 3368-3370, doi:10.1063/1.1618018 (2003).
146. Joyce, H. J. *et al.* High Purity GaAs Nanowires Free of Planar Defects: Growth and Characterization. *Advanced Functional Materials* **18**, 3794-3800, doi:10.1002/adfm.200800625 (2008).
147. Uccelli, E. *et al.* Three-Dimensional Multiple-Order Twinning of Self-Catalyzed GaAs Nanowires on Si Substrates. *Nano letters* **11**, 3827-3832, doi:10.1021/nl201902w (2011).
148. Shen, G., Chen, P.-C., Bando, Y., Golberg, D. & Zhou, C. Single-Crystalline and Twinned Zn<sub>3</sub>P<sub>2</sub> Nanowires: Synthesis, Characterization, and Electronic Properties. *The Journal of Physical Chemistry C* **112**, 16405-16410, doi:10.1021/jp806334k (2008).
149. Klamchuen, A. *et al.* Impurity induced periodic mesostructures in Sb-doped SnO<sub>2</sub> nanowires. *J Cryst Growth* **312**, 3251-3256, doi:http://dx.doi.org/10.1016/j.jcrysgro.2010.08.011 (2010).
150. Gan, L., Liao, M., Li, H., Ma, Y. & Zhai, T. Geometry-induced high performance ultraviolet photodetectors in kinked SnO<sub>2</sub> nanowires. *Journal of Materials Chemistry C* **3**, 8300-8306, doi:10.1039/C5TC01178G (2015).
151. Shen, G., Liang, B., Wang, X., Chen, P.-C. & Zhou, C. Indium Oxide Nanospirals Made of Kinked Nanowires. *ACS Nano* **5**, 2155-2161, doi:10.1021/nn103358y (2011).

152. Liang, B. *et al.* Ladder-like metal oxide nanowires: Synthesis, electrical transport, and enhanced light absorption properties. *Nano Research* **7**, 272-283, doi:10.1007/s12274-013-0394-7 (2014).
153. Wang, G., Park, J., Wexler, D., Park, M. S. & Ahn, J.-H. Synthesis, Characterization, and Optical Properties of In<sub>2</sub>O<sub>3</sub> Semiconductor Nanowires. *Inorganic Chemistry* **46**, 4778-4780, doi:10.1021/ic700386z (2007).
154. Yan, C. Y., Singh, N. & Lee, P. S. Kinking-Induced Structural Evolution of Metal Oxide Nanowires into Single-Crystalline Nanorings. *Acs Nano* **4**, 5350-5356 (2010).
155. Dick, K. A. *et al.* The Morphology of Axial and Branched Nanowire Heterostructures. *Nano letters* **7**, 1817-1822, doi:10.1021/nl0705900 (2007).
156. Svensson, S. F. *et al.* Control and understanding of kink formation in InAs-InP heterostructure nanowires. *Nanotechnology* **24** (2013).
157. Hillerich, K. *et al.* Strategies To Control Morphology in Hybrid Group III-V/Group IV Heterostructure Nanowires. *Nano letters* **13**, 903-908, doi:10.1021/nl303660h (2013).
158. Tian, B. *et al.* Three-Dimensional, Flexible Nanoscale Field-Effect Transistors as Localized Bioprobes. *Science* **329**, 830-834 (2010).
159. Xu, L. *et al.* Design and Synthesis of Diverse Functional Kinked Nanowire Structures for Nanoelectronic Bioprobes. *Nano letters* **13**, 746-751, doi:10.1021/nl304435z (2013).
160. Xu, L., Jiang, Z., Mai, L. & Qing, Q. Multiplexed Free-Standing Nanowire Transistor Bioprobe for Intracellular Recording: A General Fabrication Strategy. *Nano letters* **14**, 3602-3607, doi:10.1021/nl5012855 (2014).
161. Tian, B., Xie, P., Kempa, T. J., Bell, D. C. & Lieber, C. M. Single-crystalline kinked semiconductor nanowire superstructures. *Nat Nano* **4**, 824-829, doi:http://www.nature.com/nnano/journal/v4/n12/suppinfo/nnano.2009.304\_S1.html (2009).
162. Schwarz, K. W. & Tersoff, J. Elementary Processes in Nanowire Growth. *Nano letters* **11**, 316-320 (2011).

163. Livneh, T., Zhang, J., Cheng, G. & Moskovits, M. Polarized Raman scattering from single  $\text{GaN}$  nanowires. *Physical Review B* **74**, 035320 (2006).
164. Kim, M. H. *et al.* Growth direction determination of a single  $\text{RuO}_2$  nanowire by polarized Raman spectroscopy. *Applied Physics Letters* **96**, 213108, doi:doi:http://dx.doi.org/10.1063/1.3435475 (2010).
165. In, J. *et al.* Polymorph-Tuned Synthesis of  $\alpha$ - and  $\beta$ - $\text{Bi}_2\text{O}_3$  Nanowires and Determination of Their Growth Direction from Polarized Raman Single Nanowire Microscopy. *Chemistry – A European Journal* **17**, 1304-1309, doi:10.1002/chem.201001684 (2011).
166. Fan, H. M. *et al.* Orientation-Dependent Raman Spectroscopy of Single Wurtzite CdS Nanowires. *The Journal of Physical Chemistry C* **112**, 1865-1870, doi:10.1021/jp7096839 (2008).
167. Moller, M. *et al.* Polarized and resonant Raman spectroscopy on single InAs nanowires. *Physical Review B* **84**, doi:10.1103/PhysRevB.84.085318 (2011).
168. Tarun, A. *et al.* Stress redistribution in individual ultrathin strained silicon nanowires: a high-resolution polarized Raman study. *New Journal of Physics* **15**, doi:10.1088/1367-2630/15/5/053042 (2013).
169. Laneuville, V. *et al.* Double strain state in a single GaN/AlN nanowire: Probing the core-shell effect by ultraviolet resonant Raman scattering. *Physical Review B* **83**, 115417 (2011).
170. Zardo, I. *et al.* Raman spectroscopy of wurtzite and zinc-blende GaAs nanowires: Polarization dependence, selection rules, and strain effects. *Physical Review B* **80**, doi:10.1103/PhysRevB.80.245324 (2009).
171. Buick, B. *et al.* Single  $\text{Al}_x\text{Ga}_{1-x}\text{As}$  nanowires probed by Raman spectroscopy. *physica status solidi (b)* **247**, 2027-2032, doi:10.1002/pssb.200983948 (2010).
172. Lopez, F. J., Hemesath, E. R. & Lauhon, L. J. Ordered Stacking Fault Arrays in Silicon Nanowires. *Nano letters* **9**, 2774-2779, doi:10.1021/nl901315s (2009).
173. Lopez, F. J., Givan, U., Connell, J. G. & Lauhon, L. J. Silicon Nanowire Polytypes: Identification by Raman Spectroscopy, Generation Mechanism, and Misfit Strain in Homostructures. *Acs Nano* **5**, 8958-8966, doi:10.1021/nn2031337 (2011).

174. Biswas, S. *et al.* Diameter-Controlled Germanium Nanowires with Lamellar Twinning and Polytypes. *Chemistry of Materials* **27**, 3408-3416, doi:10.1021/acs.chemmater.5b00697 (2015).
175. Reina, A. *et al.* Large Area, Few-Layer Graphene Films on Arbitrary Substrates by Chemical Vapor Deposition. *Nano letters* **9**, 30-35, doi:10.1021/nl801827v (2009).
176. Li, Y.-L., Kinloch, I. A. & Windle, A. H. Direct Spinning of Carbon Nanotube Fibers from Chemical Vapor Deposition Synthesis. *Science* **304**, 276-278, doi:10.1126/science.1094982 (2004).
177. Xiang, B. *et al.* Rational Synthesis of p-Type Zinc Oxide Nanowire Arrays Using Simple Chemical Vapor Deposition. *Nano letters* **7**, 323-328, doi:10.1021/nl062410c (2007).
178. Anthony C Jones, M. L. H. *Chemical Vapour Deposition : Precursors, Processes and Applications* (ed Michael L Hitchman and Anthony C Jones) 582 (The Royal Society of Chemistry, 2008).
179. Guan, Z. *Boron carbide nanowires: Synthesis and characterization* 3608286 thesis, The University of North Carolina at Charlotte, (2013).
180. David B. Williams, C. Barry Carter. *Transmission Electron Microscopy A Textbook for Materials Science* (Springer US, 2009).
181. Tursunov, O. *et al.* The Influence of Laser Biotechnology on Energetic Value and Chemical Parameters of *Rose Multiflora* Biomass and Role of Catalysts for bio-energy production from Biomass: Case Study in Krakow-Poland. *World Journal of Environmental Engineering* **3**, 58-66, doi:10.12691/wjee-3-2-5 (2015).
182. Materials Evaluation and Engineering, I. in *Handbook of Analytical Methods for Materials* (2014).
183. Krumeich, F. *Imaging and Diffraction in the TEM (schematic)*, <<http://www.microscopy.ethz.ch/TEMED.htm>> (2015).
184. Hafner, B. *Energy Dispersive Spectroscopy on the SEM: A Primer*.
185. *EDS Principle*, <<http://ywcmatsci.yale.edu/edx-principle>>

186. Egerton, R. F. *Electron Energy-Loss Spectroscopy in the Electron Microscope* (Springer US, 2011).
187. Persson, P. O. Å., Höglund, C., Birch, J. & Hultman, L. Ti<sub>2</sub>Al(O,N) formation by solid-state reaction between substoichiometric TiN thin films and Al<sub>2</sub>O<sub>3</sub> (0001) substrates. *Thin Solid Films* **519**, 2421-2425, doi:http://dx.doi.org/10.1016/j.tsf.2010.12.002 (2011).
188. George Sarau, A. B., Renata Lewandowska and Silke Christiansen in *Advanced Aspects of Spectroscopy* (ed Muhammad Akhyar Farrukh) (InTech, 2012).
189. Vandenabeele, P. *Practical Raman Spectroscopy - An Introduction* (John Wiley & Sons, Ltd, 2013).
190. Wingert, M. C., Chen, Z. C. Y., Kwon, S., Xiang, J. & Chen, R. Ultra-sensitive thermal conductance measurement of one-dimensional nanostructures enhanced by differential bridge. *Review of Scientific Instruments* **83**, 024901, doi:doi:http://dx.doi.org/10.1063/1.3681255 (2012).
191. Pop, E., Mann, D., Wang, Q., Goodson, K. & Dai, H. Thermal Conductance of an Individual Single-Wall Carbon Nanotube above Room Temperature. *Nano letters* **6**, 96-100, doi:10.1021/nl052145f (2006).
192. Majumdar, D., Biswas, S., Ghoshal, T., Holmes, J. D. & Singha, A. Probing Thermal Flux in Twinned Ge Nanowires through Raman Spectroscopy. *ACS Appl Mater Inter* **7**, 24679-24685, doi:10.1021/acsami.5b07025 (2015).
193. Shi, L. *et al.* Measuring Thermal and Thermoelectric Properties of One-Dimensional Nanostructures Using a Microfabricated Device. *Journal of Heat Transfer* **125**, 881-888, doi:10.1115/1.1597619 (2003).
194. Z.L. Wang, Z. R. D., R.P. Gao, Z.G. Bai and J.L. Gole. Side-by-Side Silicon Carbide-Silica Biaxial Nanowires Synthesis, structure and mechanical properties.pdf. *Applied Physics Letters* **77**, 3 (2000).
195. Zhu, Y., Xu, F., Qin, Q., Fung, W. Y. & Lu, W. Mechanical Properties of Vapor-Liquid-Solid Synthesized Silicon Nanowires. *Nano letters* **9**, 3934-3939, doi:10.1021/nl902132w (2009).

196. Xu, F., Qin, Q., Mishra, A., Gu, Y. & Zhu, Y. Mechanical properties of ZnO nanowires under different loading modes. *Nano Research* **3**, 271-280, doi:10.1007/s12274-010-1030-4 (2010).
197. Cheng, G. *et al.* Large anelasticity and associated energy dissipation in single-crystalline nanowires. *Nat Nano* **10**, 687-691, doi:10.1038/nnano.2015.135
198. Naoki, O., Kounosuke, K., Ken, N. & Yasushi, S. Measurement of Young's Modulus of Silicon Single Crystal at High Temperature and Its Dependency on Boron Concentration Using the Flexural Vibration Method. *Japanese Journal of Applied Physics* **39**, 368 (2000).
199. Tsai, C.-Y. *et al.* Growth and properties of single-crystalline Ge nanowires and germanide/Ge nano-heterostructures. *CrystEngComm* **14**, 53-58, doi:10.1039/C1CE06107K (2012).
200. Choi, S.-Y., Fung, W. Y. & Lu, W. Growth and electrical properties of Al-catalyzed Si nanowires. *Applied Physics Letters* **98**, 033108, doi:doi:http://dx.doi.org/10.1063/1.3544933 (2011).
201. Gonchar, K. A. *et al.* Growth, Structure and Optical Properties of Silicon Nanowires Formed by Metal-Assisted Chemical Etching. *Journal of Nanoelectronics and Optoelectronics* **7**, 602-606, doi:10.1166/jno.2012.1401 (2012).
202. Brönstrup, G. *et al.* Optical Properties of Individual Silicon Nanowires for Photonic Devices. *ACS Nano* **4**, 7113-7122, doi:10.1021/nn101076t (2010).
203. Cui, Y., Zhong, Z., Wang, D., Wang, W. U. & Lieber, C. M. High Performance Silicon Nanowire Field Effect Transistors. *Nano letters* **3**, 149-152, doi:10.1021/nl025875l (2003).
204. Ma, Y. & Tong, L. Optically pumped semiconductor nanowire lasers. *Frontiers of Optoelectronics* **5**, 239-247, doi:10.1007/s12200-012-0277-7 (2012).
205. Dai, X. *et al.* GaAs/AlGaAs Nanowire Photodetector. *Nano letters* **14**, 2688-2693, doi:10.1021/nl5006004 (2014).
206. Hwang, I.-S., Kim, Y.-S., Kim, S.-J., Ju, B.-K. & Lee, J.-H. A facile fabrication of semiconductor nanowires gas sensor using PDMS patterning and solution deposition. *Sensors and Actuators B: Chemical* **136**, 224-229, doi:http://dx.doi.org/10.1016/j.snb.2008.10.042 (2009).

207. Holm, J. V. *et al.* Surface-passivated GaAsP single-nanowire solar cells exceeding 10% efficiency grown on silicon. *Nat Commun* **4**, 1498, doi:[http://www.nature.com/ncomms/journal/v4/n2/supinfo/ncomms2510\\_S1.html](http://www.nature.com/ncomms/journal/v4/n2/supinfo/ncomms2510_S1.html) (2013).
208. Hochbaum, A. I., Fan, R., He, R. & Yang, P. Controlled Growth of Si Nanowire Arrays for Device Integration. *Nano letters* **5**, 457-460, doi:10.1021/nl047990x (2005).
209. Romanyuk, K. *et al.* Optimized Ge nanowire arrays on Si by modified surfactant mediated epitaxy. *Physical Review B* **75** (2007).
210. Pevzner, A. *et al.* Confinement-Guided Shaping of Semiconductor Nanowires and Nanoribbons: “Writing with Nanowires”. *Nano letters* **12**, 7-12, doi:10.1021/nl201527h (2012).
211. Jiang, J.-W. & Rabczuk, T. Mechanical oscillation of kinked silicon nanowires: A natural nanoscale spring. *Applied Physics Letters* **102**, 123104, doi:10.1063/1.4799029 (2013).
212. Jiang, Z., Qing, Q., Xie, P., Gao, R. & Lieber, C. M. Kinked p–n Junction Nanowire Probes for High Spatial Resolution Sensing and Intracellular Recording. *Nano letters* **12**, 1711-1716, doi:10.1021/nl300256r (2012).
213. Zimmerman, J. F. *et al.* Free-Standing Kinked Silicon Nanowires for Probing Inter- and Intracellular Force Dynamics. *Nano letters*, doi:10.1021/acs.nanolett.5b01963 (2015).
214. Madras, P., Dailey, E. & Drucker, J. Kinetically Induced Kinking of Vapor–Liquid–Solid Grown Epitaxial Si Nanowires. *Nano letters* **9**, 3826-3830, doi:10.1021/nl902013g (2009).
215. He, Z., Nguyen, H. T., Duc Toan, L. & Pribat, D. A detailed study of kinking in indium-catalyzed silicon nanowires. *CrystEngComm* **17**, 6286-6296, doi:10.1039/c5ce00773a (2015).
216. LaPierre, R. R. *et al.* III–V nanowire photovoltaics: Review of design for high efficiency. *physica status solidi (RRL) – Rapid Research Letters* **7**, 815-830, doi:10.1002/pssr.201307109 (2013).
217. I. Regolin, D. S., S. Luttjohann, V. Khorenko, W. Prost, J. Kastner, G. Dumpich, C. Meier, A. Lorke, F.-J. Tegude. Growth and characterisation of

- GaAsInGaAsGaAs nanowhiskers on(1 1 1) GaAs.pdf. *J Cryst Growth* **298**, 607-611, doi:10.1016/j.jcrysgr.2006.10.122 (2007).
218. Youn-Joo, H., Alois, L., Mathias, S., Emmerich, B. & Peter, P. Orientation specific synthesis of kinked silicon nanowires grown by the vapour–liquid–solid mechanism. *Nanotechnology* **20**, 125606 (2009).
219. Shin, N., Chi, M. & Filler, M. A. Interplay between Defect Propagation and Surface Hydrogen in Silicon Nanowire Kinking Superstructures. *ACS Nano* **8**, 3829-3835, doi:10.1021/nn500598d (2014).
220. E.J. Schwalbach, S. H. D., P.W. Voorhees, D. Wheeler and J.A. Warren. Liquid droplet dynamics and complex morphologies in vapor–liquid–solid nanowire growth. *J. Mater. Res.* **26**, 2186-2198, doi:10.1557/jmr.2011.96 (2011).
221. Hocevar, M. *et al.* Growth and optical properties of axial hybrid III–V/silicon nanowires. *Nat Commun* **3**, 1266, doi:http://www.nature.com/ncomms/journal/v3/n12/supinfo/ncomms2277\_S1.html (2012).
222. Ashbee, K. H. G. Defects in boron carbide before and after neutron irradiation. *Acta Metallurgica* **19**, 1079-1085, doi:http://dx.doi.org/10.1016/0001-6160(71)90040-X (1971).
223. Mackinnon, I. D. R., Aselage, T. & Van Deusen, S. B. High resolution imaging of boron carbide microstructures. *AIP Conference Proceedings* **140**, 114-120, doi:doi:http://dx.doi.org/10.1063/1.35612 (1986).
224. Miller, M. L. & Mackinnon, I. D. R. A Comparison of Calculated and Experimental Hrtm Images for Twinned Boron Carbide. *MRS Online Proceedings Library Archive* **97**, 133 (136 pages), doi:doi:10.1557/PROC-97-133 (1987).
225. Anselmi-Tamburini, U., Munir, Z. A., Kodera, Y., Imai, T. & Ohyanagi, M. Influence of Synthesis Temperature on the Defect Structure of Boron Carbide: Experimental and Modeling Studies. *Journal of the American Ceramic Society* **88**, 1382-1387, doi:10.1111/j.1551-2916.2005.00245.x (2005).
226. Schwarz, K. W., Tersoff, J., Kodambaka, S. & Ross, F. M. Jumping-Catalyst Dynamics in Nanowire Growth. *Phys Rev Lett* **113**, doi:10.1103/PhysRevLett.113.055501 (2014).

227. Schwalbach, E. J., Davis, S. H., Voorhees, P. W., Warren, J. A. & Wheeler, D. Stability and topological transformations of liquid droplets on vapor-liquid-solid nanowires. *Journal of Applied Physics* **111**, 024302, doi:doi:http://dx.doi.org/10.1063/1.3676451 (2012).
228. F.M. Ross, J. T., and M.C. Reuter. Sawtooth Faceting in Silicon Nanowires.pdf. *Phys Rev Lett* **2005**, 146104-146101, doi:10.1103/PhysRevLett.95.146104 (2005).
229. Wood, C. Boron carbides as high temperature thermoelectric materials. *AIP Conference Proceedings* **140**, 362-372, doi:doi:http://dx.doi.org/10.1063/1.35584 (1986).
230. Liu, C. H. Structure and properties of boron carbide with aluminum incorporation. *Materials Science and Engineering: B* **72**, 23-26, doi:http://dx.doi.org/10.1016/S0921-5107(99)00597-8 (2000).
231. Cai, K.-f. & Nan, C.-W. The influence of  $W_2B_5$  addition on microstructure and thermoelectric properties of  $B_4C$  ceramic. *Ceramics International* **26**, 523-527, doi:http://dx.doi.org/10.1016/S0272-8842(99)00089-9 (2000).
232. Aselage, T. L., Emin, D., McCready, S. S. & Duncan, R. V. Large Enhancement of Boron Carbides' Seebeck Coefficients through Vibrational Softening. *Phys Rev Lett* **81**, 2316-2319 (1998).
233. Dresselhaus, M. S. *et al.* Low-dimensional thermoelectric materials. *Phys. Solid State* **41**, 679-682, doi:10.1134/1.1130849 (1999).
234. Dresselhaus, M. S. *et al.* New Directions for Low-Dimensional Thermoelectric Materials. *Advanced Materials* **19**, 1043-1053, doi:10.1002/adma.200600527 (2007).
235. Mavrokefalos, A., Pettes, M. T., Zhou, F. & Shi, L. Four-probe measurements of the in-plane thermoelectric properties of nanofilms. *Review of Scientific Instruments* **78**, 034901, doi:doi:http://dx.doi.org/10.1063/1.2712894 (2007).
236. Wood, C., Emin, D. & Gray, P. E. Thermal conductivity behavior of boron carbides. *Physical Review B* **31**, 6811-6814 (1985).
237. Aselage, T. L., Emin, D. & McCready, S. S. Conductivities and Seebeck coefficients of boron carbides: Softening bipolaron hopping. *Physical Review B* **64**, 054302 (2001).

238. Costescu, R. M., Wall, M. A. & Cahill, D. G. Thermal conductance of epitaxial interfaces. *Physical Review B* **67**, 054302 (2003).
239. Zhou, F. *et al.* Thermal conductivity of indium arsenide nanowires with wurtzite and zinc blende phases. *Physical Review B* **83**, 205416 (2011).
240. Wan, C., Wang, Y., Norimatsu, W., Kusunoki, M. & Koumoto, K. Nanoscale stacking faults induced low thermal conductivity in thermoelectric layered metal sulfides. *Applied Physics Letters* **100**, 101913, doi:doi:http://dx.doi.org/10.1063/1.3691887 (2012).
241. Lee, S.-Y. *et al.* Control of surface morphology and crystal structure of silicon nanowires and their coherent phonon transport characteristics. *Acta Materialia* **64**, 62-71, doi:http://dx.doi.org/10.1016/j.actamat.2013.11.042 (2014).
242. Yang, J. *et al.* Phonon Transport through Point Contacts between Graphitic Nanomaterials. *Phys Rev Lett* **112**, 205901 (2014).
243. Emin, D. Structure and single-phase regime of boron carbides. *Physical Review B* **38**, 6041-6055 (1988).
244. Mauri, F., Vast, N. & Pickard, C. J. Atomic Structure of Icosahedral  $\text{B}_4\text{C}$  Boron Carbide from a First Principles Analysis of NMR Spectra. *Phys Rev Lett* **87**, 085506 (2001).
245. Nathalie, V., Jelena, S. & Emmanuel, B. Boron carbides from first principles. *Journal of Physics: Conference Series* **176**, 012002 (2009).
246. Aselage, T. L. & Tissot, R. G. Lattice Constants of Boron Carbides. *Journal of the American Ceramic Society* **75**, 2207-2212, doi:10.1111/j.1151-2916.1992.tb04485.x (1992).
247. Morosin, B., Kwei, G. H., Lawson, A. C., Aselage, T. L. & Emin, D. Neutron powder diffraction refinement of boron carbides nature of intericosahedral chains. *Journal of Alloys and Compounds* **226**, 121-125, doi:http://dx.doi.org/10.1016/0925-8388(95)01585-X (1995).
248. Azevedo, L. J., Venturini, E. L., Emin, D. & Wood, C. Magnetic susceptibility study of boron carbides. *Physical Review B* **32**, 7970-7972 (1985).
249. Conde, O., Silvestre, A. J. & Oliveira, J. C. Influence of carbon content on the crystallographic structure of boron carbide films. *Surface and Coatings*

- Technology* **125**, 141-146, doi:[http://dx.doi.org/10.1016/S0257-8972\(99\)00594-0](http://dx.doi.org/10.1016/S0257-8972(99)00594-0) (2000).
250. Nakashima, S., Ohta, H., Hangyo, M. & Palosz, B. Phonon Raman scattering in disordered silicon carbides. *Philosophical Magazine Part B* **70**, 971-985, doi:[10.1080/01418639408240266](https://doi.org/10.1080/01418639408240266) (1994).
251. Rohmfeld, S., Hundhausen, M. & Ley, L. Raman scattering in polycrystalline 3C-SiC: Influence of stacking faults. *Physical Review B* **58**, 9858-9862 (1998).
252. Nakashima, S., Nakatake, Y., Harima, H., Katsuno, M. & Ohtani, N. Detection of stacking faults in 6H-SiC by Raman scattering. *Applied Physics Letters* **77**, 3612-3614, doi:[doi:doi:http://dx.doi.org/10.1063/1.1329629](http://dx.doi.org/10.1063/1.1329629) (2000).
253. Lu, X. *et al.* Rapid and Nondestructive Identification of Polytypism and Stacking Sequences in Few-Layer Molybdenum Diselenide by Raman Spectroscopy. *Advanced Materials* **27**, 4502-4508, doi:[10.1002/adma.201501086](https://doi.org/10.1002/adma.201501086) (2015).
254. Scientific, H. *LabSpec 5 user manual*. (2008).
255. Kuhlmann, U. & Werheit, H. Raman effect of boron carbide (B<sub>4.3</sub>C to B<sub>10.37</sub>C). *Journal of Alloys and Compounds* **205**, 87-91, doi:[http://dx.doi.org/10.1016/0925-8388\(94\)90771-4](http://dx.doi.org/10.1016/0925-8388(94)90771-4) (1994).
256. Domnich, V., Gogotsi, Y., Trenary, M. & Tanaka, T. Nanoindentation and Raman spectroscopy studies of boron carbide single crystals. *Applied Physics Letters* **81**, 3783-3785, doi:[doi:doi:http://dx.doi.org/10.1063/1.1521580](http://dx.doi.org/10.1063/1.1521580) (2002).
257. Werheit, H. *et al.* On surface Raman scattering and luminescence radiation in boron carbide. *Journal of Physics: Condensed Matter* **22**, 045401 (2010).
258. Reddy, K. M., Liu, P., Hirata, A., Fujita, T. & Chen, M. W. Atomic structure of amorphous shear bands in boron carbide. *Nature Communications* **4**, 2483, doi:[10.1038/ncomms3483](https://doi.org/10.1038/ncomms3483) (2013).
259. Emura, K. S. a. S. Lattice vibrations and the bonding nature of boron carbide. *J. Phys.: Condens. Matter* **8**, 10919 (1996).
260. McClellan, K. J., Chu, F., Roper, J. M. & Shindo, I. Room temperature single crystal elastic constants of boron carbide. *Journal of Materials Science* **36**, 3403-3407, doi:[10.1023/a:1017947625784](https://doi.org/10.1023/a:1017947625784) (2001).

261. Lopez, F. J. *et al.* Diameter and Polarization-Dependent Raman Scattering Intensities of Semiconductor Nanowires. *Nano letters* **12**, 2266-2271, doi:10.1021/nl204537d (2012).
262. Hsu, H.-C. *et al.* Polarized and diameter-dependent Raman scattering from individual aluminum nitride nanowires: The antenna and cavity effects. *Applied Physics Letters* **101**, doi:10.1063/1.4753798 (2012).

## APPENDIX A: COMPARISON BETWEEN EELS AND EDX

It is well known that EELS is more sensitive and accurate to detect light elements (i.e. B and C). However due to the limitation of accessing the EELS instrument, in this dissertation, the EDX is used to determine the composition of boron carbide nanowires. In order to confirm the carbon concentration information obtained from the EDX is acceptable to investigate the carbon dependent thermal transport and Raman scattering in boron carbide, we have collected and compared both EELS (9.36-15.35% C) and EDX (8.5-16.23%) spectra of 81 boron carbide nanowires. As can be seen in Figure A1, the distribution of carbon content difference between EELS and EDX from all measured nanowires are plotted, in which more than half (47) of the total number of nanowires exhibit a difference less than 2%, while only 5 nanowires have differences of 3.5-4% and the rest are in between 2-3.5%. By taking uncertainty in examining location into consideration, it is safe to conclude that the carbon concentration obtained from our EDX is comparable to the EELS with a relatively small difference.

